On Scalable, Reconfigurable, and Intelligent Metasurfaces

Doctoral thesis by:
Hamidreza Taghvaee

Thesis Advisors:
Dr. Sergi Abadal
Prof. Alberto Cabellos-Aparicio

Department of Computer Architecture
Barcelona, Spain
April 2021

Acknowledgments

Throughout the history humans migrated across the globe to begin a new life. In March 2018, I left my country with my wife and started a fascinating journey as a PhD student. Spain gave me the opportunity and welcomed me with open arms. Like any other adventure mine was full of up and downs. My friends and colleagues helped me to get along with this new life. Back in the day many things were difficult for me but after 3 years I feel comfortable to call Barcelona HOME. Undertaking this PhD has been a truly life-changing experience for me and it would not have been possible to do without the support and guidance that I received from many people. I would like to thank my esteemed supervisor Dr. Sergi Abadal for his invaluable supervision, support and tutelage during the course of my PhD degree. My gratitude extends to Prof. Eduard Alarcón, Prof. Albert Cabellos-Aparicio, and Prof. Josep Solé Pareta for their invaluable advice, continuous support, and patience during my PhD study. Additionally, I would like to express gratitude to Prof. Sergei Tretyakov who provided me an opportunity to join his team as a doctoral visiting student at Aalto University, his treasured support was really influential in shaping my wisdom over Electromagnetic. I also thank Prof. Fu Liu and Dr. Ana Díaz-Rubio for their mentorship and valuable guidance throughout my studies. My sincere appreciation goes to UPC panel committee Prof. Jose Antonio Lazaro and Prof. Davide Careglio as well as external examiners Prof. Tie Jun Cui and Prof. Josep Miquel Jornet. Their suggestions brought in threads of thought that made my research richer. I would like to thank UPC, the doctoral school, the DAC department, secretary and administrative staff members Mr. Albert Lopez and Ms. Joana Munuera. I would like to thank my friends, lab mates, colleagues and research team Dr. Akshay Jain, Mr. Xavier Timoneda i Comas, Mr. Robert Guirado, Mr. Jorge López Alonso, Dr. Filip Lemic, Dr. Odysseas Tsilipakos, Dr. Alexandros Pitilakis, Dr. Taqwa Saeed, Dr. Xuchen Wang, Dr. Svetlana Tcvetkova, Dr. Prasad Jayathurathnage, Mr. Francisco Cuesta, Mr. Grigorii Ptitcyn, Prof. Simovski Constantin, Mr. Masoud Sharifian, Mr. Reza Heydarian for a cherished time spent together in the lab, and in social settings. My appreciation also goes out to my family for their encouragement and support all through my studies. Special thanks goes to my wife Faezeh Zarrinkhat, whom without this would have not been possible.

Preface

Sixth Generation (6G) wireless networks will be even more heterogeneous and dense as compared to Fifth Generation (5G) and other legacy networks. Thus, the 6G architecture will need to be adapted to serve the ever-evolving capacity and quality of service requirements. To satisfy these ever-increasing demands, multiple enablers such as visible light communication, light fidelity, Reconfigurable Intelligent Surface (RIS)s, TeraHertz (THz) communications, etc., have been proposed. Specifically, RISs, through their programmable characteristics, can perform the fine-grained manipulation of the radio signals being generated by the myriad transmitter devices/access points for their corresponding receivers. Such manipulations include absorption of certain components of the impinging radio signals, as well as fine-grained control of these signals in terms of direction, polarization, phase, and power in a frequency-selective manner.

An RIS consists of a device that controls the behavior of the EM waves, alongside circuits that provide the tuning mechanism and the intelligence to control it. This device that controls the EM wave behavior can be realized using Metasurface (MS)s, which are electromagnetically thin-film and planar artificial structures that enable the control of EM fields in engineered and even atypical ways. Hence, the MS is a component of the RIS. On a more granular level, an MS is composed of subwavelength building blocks known as unit cells or meta-atoms. The design of these unit cells depends on the required EM functionality, reconfigurability, or accuracy.

The promises of the RIS paradigm, therefore, come at the expense of a non-trivial complexity in the MS. On the one hand, the performance of an RIS depends on the size of the unit cells, the number of unit cell states, or the size of the whole MS. On the other hand, there are costs and energy overheads associated with the fabrication and operation of RISs that also scale with the aforementioned factors. This thesis aims to bridge this gap by providing a method to dimension the RIS through a design-oriented scalability analysis of programmable MSs.

Besides the challenge of design complexity, MSs will become prone to failure as they continue integrating sophisticated tuning, control and sensing circuits. However, the impact

of faults on the performance of individual MSs is not well understood yet. This thesis proposes a framework to evaluate the impact of failures in programmable MSs, distinguishing between the type of faults and their spatial distribution.

While RIS generally hinge on the design of rather complex tunable MSs, such a complexity can be amortized if the functionality provided by the RIS can be shared among multiple users. This thesis introduces a coding (i.e. digital programming of unit cells) technique based on the momentum conservation law and superposition of waves for MS reconfiguration to engineer multiple beams independently. Then, the wireless channel of such framework among multiple users is evaluated. The capacity is increased at least one order of magnitude compared to a scenario without RIS.

Machine Learning (ML) techniques, and particularly Neural Networks (NNs), owing to their ability to learn complex relationships between input and output data, are capable of solving differential equations, thereby circumventing the need for numerical calculations. This thesis provisions a data-driven NN-based approach for determining an accurate estimation of the radiation pattern or several measures of interest that enable the full characterization of the radiation pattern.

In summary, contributions of this thesis fall under the umbrella of paving the way to realizing 5G and beyond wireless communications empowered with RIS technology.

List of Publications

Publications in the framework of the thesis

[**J1**] **H Taghvaee**, A Cabellos-Aparicio, J Georgiou, S Abadal, "Error analysis of programmable metasurfaces for beam steering", IEEE Journal on Emerging and Selected Topics in Circuits and Systems, 2020 Pages 62-74.

[**J2**] **H Taghvaee**, S Abadal, A Pitilakis, O Tsilipakos, A C Tasolamprou, C Liaskos, M Kafesaki, N V Kantartzis, A Cabellos-Aparicio, E Alarcón, "Scalability Analysis of Programmable Metasurfaces for Beam Steering", IEEE Access, 2020 Pages 105320-105334.

[**J3**] **H Taghvaee**, A Jain, X Timoneda, C Liaskos, S Abadal, E Alarcón, A Cabellos-Aparicio. "Radiation Pattern Prediction for Metasurfaces: A Neural Network-Based Approach", Sensors. 2021; 21(8):2765.

[**C1**] **H Taghvaee**, S Abadal, A Cabellos, E Alarcon, "On the use of Genetic Algorithm to Design and Optimize Graphene-based Absorbers", Nanophotonics and Micro/Nano Optics International Conference 2018, 1st - 3rd October.

[**C2**] **H Taghvaee**, S Abadal, J Georgiou, A Cabellos-Aparicio and E Alarcón, "Fault Tolerance in Programmable Metasurfaces: the Beam Steering Case" in Proceedings of the ISCAS '19, Sapporo, Japan, May 2019.

[**B1**] **H Taghvaee**, S Abadal, E Alarcón, A Cabellos-Aparicio, T Saeed, A Pitsillides, O Tsilipakos, C Liaskos, A Tasolamprou, M Kafesaki, A Pitilakis, N V Kantartzis, V Soteriou, M Lestas, "The scaling laws of HyperSurfaces", CRC Press, 2020, 8: 1-8: 41.

Other publications

[**J4**] A C Tasolamprou, A Pitilakis, S Abadal, O Tsilipakos, X Timoneda, **H Taghvaee**, M S Mirmoosa, F Liu, C Liaskos, A Tsioliaridou, S Ioannidis, N V Kantartzis, D Manessis, J Georgiou, A Cabellos-Aparicio, E Alarcón, A Pitsillides, I F Akyildiz, S A Tretyakov, E N Economou, M Kafesaki, C M Soukoulis, "Exploration of intercell wireless millimeter-wave communication in the landscape of intelligent metasurfaces", IEEE Access, 2020 Pages 122931-122948.

[**J5**] O Tsilipakos, A C Tasolamprou, A Pitilakis, F Liu, X Wang, M S Mirmoosa, D C Tzarouchis, S Abadal, **H Taghvaee**, , C Liaskos, A Tsioliaridou, J Georgiou, A Cabellos-Aparicio, E Alarcón, S Ioannidis, A Pitsillides, I F Akyildiz, N V Kantartzis, E N Economou, C M Soukoulis, M Kafesaki, S Tretyakov, "Toward Intelligent Metasurfaces: The Progress from Globally Tunable Metasurfaces to Software-Defined Metasurfaces with an Embedded Network of Controllers", Advanced Optical Materials, 2020 Pages 2000783.

[**C3**] S Abadal, A Marruedo, A Franques, **H Taghvaee**, A Cabellos-Aparicio, J Zhou, J Torrellas and E Alarcón, "Opportunistic Beamforming in Wireless Network-on-Chip," in Proceedings of the ISCAS '19, Sapporo, Japan, May 2019.

[**C4**] T. Saeed, S. Abadal, C. Liaskos, A. Pitsillides, **H. Taghvaee**, A. Cabellos-Aparicio, M. Lestas, and E. Alarcón, "Workload Characterization of Programmable Metasurfaces," Proceedings of the Sixth Annual ACM International Conference on Nanoscale Computing and Communication, 2019.

[**C5**] N Ashraf, M Lestas, T Saeed, **H Taghvaee**, S Abadal, A Pitsillides, C Liaskos, "Extremum Seeking Control for Beam Steering using Hypersurfaces", 2020 IEEE International Conference on Communications Workshops.

[**C6**] J Klein, A Levisse, G Ansaloni, D Atienza, M Zapater, M Dazzi, G Karunaratne, I Boybat, A Sebastian, D Rossi, F Conti, E P de Santana, P H Bolívar, M Saeed, R Negra, Z Wang, K Wang, M C Lemme, A Jain, R Guirado, **H Taghvaee**, S Abadal, "Architecting more than Moore: wireless plasticity for massive heterogeneous computer architectures (WiPLASH)", Proceedings of the 18th ACM International Conference on Computing Frontiers, 191-193, 2021.

Index

List of Figures

List of Tables

List of Abbreviations

2G	Second generation
3G	Third generation
3GPP	Third Generation Partnership Project
4G	Fourth generation
5G	Fifth generation
5G NR	5G New Radio
5GPPP	The Fifth Generation infrastructure Public Private Partnership
6G	Sixth Generation
ACK	Acknowledgment
AP	Access Point
BS	Base Station
CNN	Convolutional Neural Network
D	Directivity
dB	decibel
dBi	decibel isotropic
DNN	Deep Neural Network
E2E	End-to-end
EM	Electromagnetic
ETSI	European Telecommunications Standards Institute
FDD	Frequency Division Duplex
FPGA	Field-Programmable Gate Arrays
GA	Genetic Algorithm
GAN	Generative Adversarial Network
GHz	GigaHertz
HetNet	Heterogeneous Networks
HPBW	Half Power Beam Width
HSF	HyperSurface
IC	Integrated Circuit

IEEE	Institute of Electrical and Electronics Engineers
IE	Information Element
ITU	International Telecommunication Union
KPI	Key Performance Indicator
LIS	Large Intelligent Surface
LoS	Line of Sight
LTE	Long Term Evolution
MAC	Medium Access Control
MBS	Macro-Base Station
MC	Macro-cell
MCBS	Macro Cell Base Station
SCBS	Small Cell Base Station
MSE	Mean Squared Error
MIMO	multiple-input multiple-output
ML	Machine Learning
MLPNN	Multi-layer Perceptron Neural Network
mmWave	Millimetre Wave
MS	Metasurface
MU-MIMO	Multi-User MIMO
NLoS	Non-Line of Sight
NN	Neural Network
NR	New Radio
NTN	Neural Tensor Network
OFDM	Orthogonal Frequency Division Multiplexing
OFDMA	Orthogonal Frequency Division Multiple Access
PCB	Printed Circuit Board
PHY	Physical
PoC	Proof of Concept
PSO	Particle Swarm Optimization
QoE	Quality of Experience
QoS	Quality of Service
RAN	Radio Access Network
RA	Reflection Angle
RCS	Radar Cross Section
RBFNN	Radial Basis Function Neural Network
RF	Radio Frequency

RIS	Reconfigurable Intelligent Surface
SBS	Small-cell Base Station
SC	Small-cell
SDM	Software Defined Metasurface
SDN	Software Defined Networking
SLA	Side-Lobes Accumulated
SLL	Side-Lobe Level
SNR	Signal to Noise Ratio
TDD	Time Division Duplex
TD	Target Deviation
TDM	Time-Division Multiplexing
TE	Transverse Electric
TM	Transverse Magnetic
THz	TeraHertz
UE	User Equipment
UL	Uplink
UMi	Urban Micro
UMTS	Universal Mobile Telecommunications Systems
VR	Virtual Reality
VLC	Visible Light Communication
Wi-Fi	Wireless Fidelity

Chapter 1

Introduction

The 5G of mobile communications is sustained by a set of key technologies that allow to satisfy the increasing speed, efficiency, and connectivity demands of wireless networks [3]. Relevant examples are massive Multiple-Input Multiple-Output (MIMO) [4], Millimeter-Wave (mmW) spectrum use [5], or software-defined networking [6]. However, a large body of research is already focusing on the major challenges and opportunities to shape the 6G of wireless networks [7–12]. In this context, the concept of Software-Defined Metasurface (SDM) has garnered considerable attention as they allow to modify at will the characteristics of the waves that impinge on it [13–15]. Using SDMs or other variants of the concept such as Reconfigurable Intelligent Surfaces (RIS), wireless environments become programmable and can be incorporated within the design loop of the network [Fig. 1.1(a)]. This represents a true paradigm shift in wireless networks, where the channel has traditionally been an inevitable limiting factor, and opens the door a plethora of novel co-design techniques with enormous potential as the recent explosion of works can attest [16–23]. Programmable MSs are the key enablers of the SDM/RIS paradigm. MSs are compact and planar arrays of subwavelength controllable resonators, i.e., the unit cells. The subwavelength granularity of these *unit cells* confers MSs with exceptional control of Electromagnetic (EM) waves as demonstrated in a variety of works [24–38]. The actual response of the MS is derived from the aggregated response of all unit cells, which need to be modified individually. For instance, beam steering requires exerting specific amplitude and phase profiles to the impinging wave [32,38–41]. The metasurface states are being built by *encoding* a discrete set of unit cell options that can be seen as *bits*. This provides a powerful and intuitive design perspective, while drawing a clear parallelism with information theory, and opens new ways to model, compose, and design advanced metasurfaces.

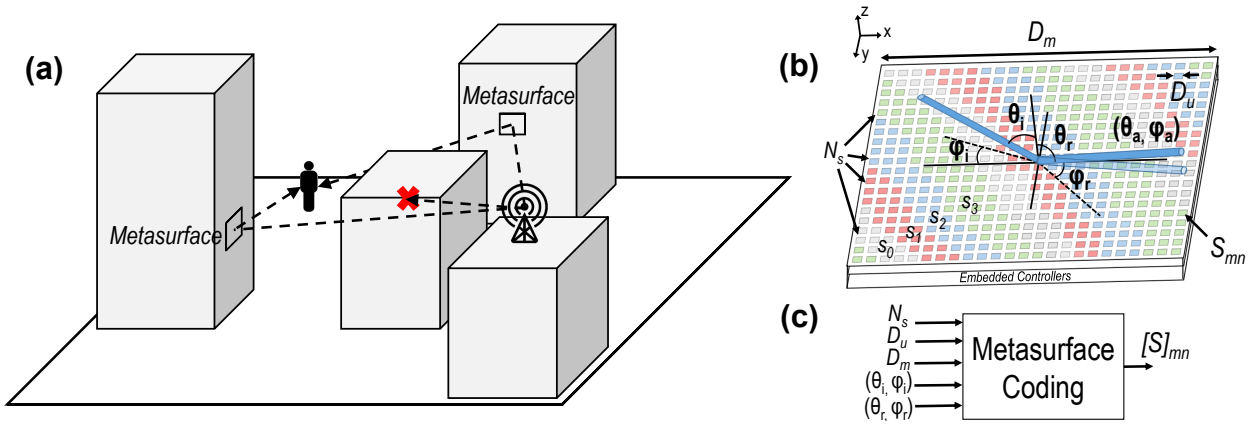

Figure 1.1: Schematic representation of (a) a wireless environment augmented with programmable MSs for coherent combination of reflected rays, (b) a MS of size D_m for beam steering with unit cells of size D_u and N_s possible states (S_0, S_1, S_2, S_3), and (c) the process of MS coding.

1.1 State of the Art

The coding approach provides a natural match for constructing the programmable metasurface paradigm and implementing reconfigurability. Programmability in MSs is achieved via the inclusion of tunable elements within the MS structure and the addition of means of control over such tunable elements [41–46]. This concept has been exemplified with several works in a variety of functionalities in the GHz and THz ranges. Table 1.1 shows a comprehensive summary of the state of the art in coding and programmable metasurfaces. As an example, consider a beam steering gradient metasurface in reflection implemented via a reconfigurable gradient index. In this case, the coding set (i.e., the set of possible unit cell states) is built by picking points where the unit cell provides high reflection amplitude and reflection phases equal to multiples of $2\pi/2^{N_{\text{bit}}}$ (N_{bit} is the number of control bits). This coding set is used by the Field-Programmable Gate Arrays (FPGA) to implement the phase profile required in each instance, a linear phase gradient in this particular case. Using programmable metasurface for holography is yet another application of significant importance. To seek the precise layout for each hologram the conventional Gerchberg–Saxton algorithm is used [30]. Besides providing a natural platform to describe a programmable metasurface, the coding approach is very well suited to modeling and optimization techniques used in areas such as signal processing or complex systems. For instance, genetic algorithms represent candidate solutions as arrays of bits and need a bounded set of solutions to be tractable, which is precisely what coding metasurface offer. This has been leveraged not only with Genetic Algorithm (GA) [47, 48], but also particle-swarm [49, 50], simulated annealing [51, 52]

or even hybrid solutions [53]. More recently, machine learning methods coupled to optimization algorithms have been proposed to reduce the time devoted to designing a given metasurface [54].

Beyond spatial coding, which enables functionalities like wavefront manipulation [64] and polarization control [60,61], space-time-coding digital metasurfaces have been introduced [65] for harnessing the advantages of temporal modulation. Applying space-time modulation on coding metasurface enables control over the *spectral* parameters of the EM wave response, thus offering an important alternative to nonlinear metasurfaces for generating new frequencies, something not possible with conventional linear variants.

In Visorsurf project [1], HSF concept integrates a network of controllers within the structure of the MS [15]. Controllers drive the reconfigurable unit cells and exchange information with neighbouring controllers so that the HSF can (i) implement a given EM functionality requested by an authorized user, and (ii) adapt to changes in the environment. The internal network of controllers is the enabler of the HSF approach and the main difference with respect to conventional programmable HSF. At the hardware level, this has been implemented either by using external FPGA [65] or by directly embedding the controllers within the MS structure [13, 16, 76–78]. At the software level, the encoding process can be tackled by modeling the EM functionalities via a set of well-defined software primitives [79].

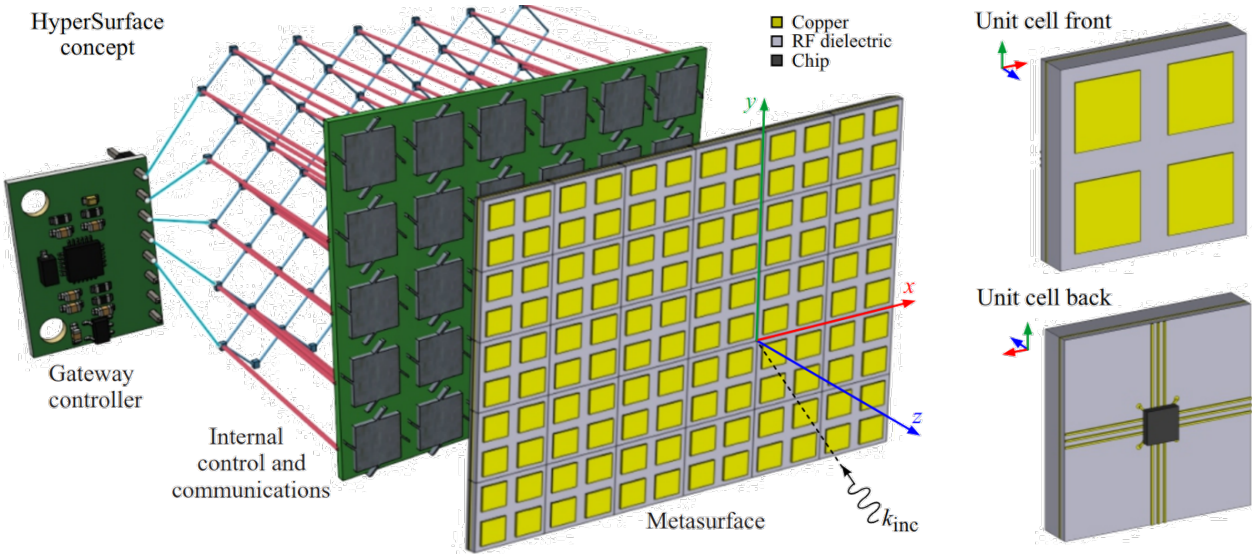

Figure 1.2: The HSF: a hardware and software platform that consist of metasurface layer (top), controllers element (middle) and network layer (bottom) [1].

Table 1.1: Summary of coding and programmable metasurfaces in the literature for different applications.

Function	**Approach**	**Frequency**	**Year**	**Ref**
RCS reduction	Optimization	7-10 GHz	2014	[55]
Low scattering	Hybrid	6-14 GHz (broadband)	2014	[53]
Low reflection	Particle swarm	1-2 THz (broadband)	2015	[49]
Wave diffusion	Particle swarm	0.8-1.7 THz (broadband)	2015	[50]
Beam reconfiguring	Analytic	8-10 GHz	2016	[56]
Diffusion	Simulated annealing	4-8 GHz (broadband)	2016	[51]
Multi-function	GA	9-12 GHz	2016	[28]
Sensor and imaging	Analytic	9-10 GHz	2016	[57]
Hologram	Gerchberg–Saxton	7.8 GHz	2017	[30]
RCS reduction	Analytic	10 GHz	2017	[58]
Focusing	Analytic	0.225-0.300 THz	2017	[59]
Vortex beam generation	Optimization	15 GHz	2017	[60]
Beam-Editing	Orbital angular momentum	15 GHz	2017	[61]
Multi-function	Optimization	0.3-3 THz	2017	[62]
RCS reduction	Simulated annealing	6-20 GHz (Wideband)	2018	[52]
RCS reduction	GA	2-20 GHz	2018	[48]
Transmission control	Optimization	1.5-7.5 GHz	2018	[63]
Wave modulating	GA	8-12 GHz (broadband)	2018	[64]
Real time wave control	binary particle swarm	8-11 GHz	2018	[65]
Vorticity conversion	Analytic	16 GHz	2019	[66]
RCS reduction	Analytic	12-30 GHz	2019	[67]
Vorticity control	Analytic	9-15 GHz	2019	[68]
Surface-space wave control	Analytic	10 GHz	2019	[69]
Multi-function	N/A	3.5-5.5 GHz	2020	[70]
Beam splitting	N/A	3.5-5.5 GHz	2020	[71]
Beam splitting	Analytic	9-11 GHz	2020	[72]
Multi-function	Analytic	1-2 THz	2020	[73]
Flexible scattering field	N/A	8 GHz	2021	[74]
Beam splitting	Analytic	5.17 GHz	2021	[75]

1.2 Challenges and Motivations

One of the many challenges posed by this novel approach concerns the design and development of the controllers and the interconnection network within the HSF [80–82]. Such a task is largely hindered by the unique combination of resource constraints and communication requirements of this new networking scenario, which prevents the use of conventional techniques and requires radically new solutions instead. Moreover, the network design may need to adapt to the different HSF use cases and evolve as soon as technology advances enable the creation of HSF with higher performance and capable of operating up to the THz or optical regime [46, 83].

The performance of a MS depends on the size of the unit cells, the number of unit cell states, or the size of the whole MS. On the other hand, there are costs and energy overheads associated with the fabrication and operation of MSs that also scale with the aforementioned factors [46]. Hence, in order to build HSFs capable of satisfying a set of application-specific requirements with the minimum cost, it becomes necessary to quantify the main scaling trends and tradeoffs of the underlying MS.

The transition from static to intelligent programmable MS has come at the cost of added design, fabrication, and embedding complexity. Programmable MS need to integrate tuning and control elements on a per-cell basis, electronic circuits to implement intelligence within the device, as well as mechanisms to interface the surface with the world. This poses important challenges at fabrication, calibration, deployment, and run time that, among others, affect reliability. In other words, MS will become prone to failure as they continue integrating sophisticated tuning, control and sensing circuits. However, the impact of faults on the performance of individual metasurfaces is not well understood yet. We claim that error analysis is a necessary step to understand the impact of transient or permanent failures on the performance of both a single MS and, crucially, a complete system. Faults might lead to inaccuracies in the steering of the reflection and cause a drop in quality of service. Further, an error analysis would also allow to derive guidelines for the implementation of robust programmable MSs, estimate the lifetime of the deployed ones, or even develop methods to save energy by power-gating a portion of the internal circuitry of the MS.

While an understanding of the radiation pattern characteristics can be obtained through either analytical models or full-wave simulations, they suffer from inaccuracy and extremely high computational complexity, respectively. This fact provides the intuition towards another direction: since the MS EM response (e.g., reflection) is essentially the solution to Maxwell's differential equations, it could be possible to design an ML construct that directly predicts the EM response, without resorting to full-wave simulations. A novel Neural Network (NN)

based approach can enable a fast and accurate characterization of the MS response.

The complexity and the cost of the MS paradigm would be justified properly when it can actually perform multiple functions concurrently. Preferentially, in the use case of wireless communications, multi-user scenarios are appreciated. In order to realize an engineered radiation pattern, MS space or time allocation should be shared between the users. Space or time multiplexing is a linear segmentation of the MS in space or time-domain for multiple users service management. However, the distribution of resources between the users diminishes the link quality compared to single user communication. Multi-user scenarios rely on the proper execution of multiplexing by which the space-time allocation is optimized. The challenge is to find the multiplexing scheme that allows to share the MS resources among multiple users without disrupting the required functionality.

1.3 Aims and Contributions

This thesis aims to address some of the challenges mentioned above. We essentially focus on the relationship between application requirements and MS design. From this information, we can derive guidelines to drive the whole design process of future HSFs/RISs. This thesis develops a semi-analytical methodology that dimensions the HSF/RIS through a design-oriented scalability analysis of programmable MSs. In particular, we study the impact of relevant design parameters on the potential performance of programmable MS. Coupled to power consumption, cost, or application-specific models and even error analysis, our methodology will provide HSF/RIS designers and network architects with a clear picture of the practicable design space, illustrating the main tradeoffs and pointing to potentially optimal regions. In this direction, the thesis makes a number of contributions as described next. In Chapter 2, we declare a general design-oriented and model-based methodology to analyze EM performance of programmable MS. Although the methodology is amenable to any functionality or application, we use it to study beam steering as a particular yet very representative functionality for HSF/RIS-enabled wireless communications [see Fig. 1.1(a)]. Finally, the accuracy of the proposed methodology is compared with full-wave simulation.

In Chapter 3, we introduce scaling model and unit cell performance model then we perform the scalability analysis with the proposed methodology (Chapter 2). Then, we investigate the impact of the incident and deflection angles on the performance. Finally, with the help of appropriate figures of merit and subsequent sensitivity analyses, we derive a set of practical design guidelines for the design of efficient programmable MS for beam steering. With this particular case study, we seek to solve questions such as which is the minimum number of unit cells that guarantee a given steering precision over a certain range

of angles, or whether it is preferable to put more unit cell states or to make unit cells smaller to improve performance.

In Chapter 4, we introduce a unit cell to design a programmable MS at 26 GHz, very relevant use case in RIS-enabled 5G communications. Then, we propose an error model to study the error scenarios in terms of distribution and types of errors. Next, we use the same methodology proposed in 2 to perform error analysis. Finally, through reporting the impact of each error scenario on the performance metrics, destructive errors and vulnerable metrics are identified and discussed qualitatively.

In Chapter 5, we propose a reconfiguration technique providing the radiation pattern for multi-user communication beyond 5G networks. Then, we analyze the performance of our proposed RIS technology for indoor and outdoor scenarios, given broadcast mode of operation. The aforesaid scenarios encompass a majority of the challenging scenarios that wireless networks encounter. Next, we show that our proposed methodology provisions sufficient gains in the observed channel capacity when the users are close to the MS in the indoor office environment scenario. Finally, we report a 1-2 orders of magnitude increase in the system throughput given the outdoor environment. The results prove that RIS with the ability to communicate with multiple users can empower wireless networks with great capacity.

In Chapter 6, we propose an NN-based approach that enables a fast and accurate characterization of the MS response. Then, We analyze multiple scenarios and demonstrate the capabilities and utility of the proposed methodology. Concretely, we show that this method can learn and predict the parameters governing the reflected wave radiation pattern with an accuracy of a full-wave simulation (98.8%–99.8%) and the time and computational complexity of an analytical model. The aforementioned result and methodology will be of specific importance for the design, fault tolerance, and maintenance of the thousands of RISs that will be deployed in the 6G network environment.

Chapter 2

Methodology for Electromagnetic Analysis of Metasurfaces

The contributions of this thesis like scalability and error analysis require a methodology to model the MS response fast and relatively accurately because we need to "simulate" many different designs, and this chapter describes such a methodology. Proposed methodology then is used in the next Chapters.

2.1 Electromagnetic model

To rigorously calculate the actual reflection phase and amplitude of each discrete state, we consider a single unit cell with periodic Floquet boundary conditions, meaning that an infinite uniform MS comprised of such unit cells is assumed in the simulation. This allows us to perform accurate full-wave simulations. When moving to the actual steering MS which is comprised of different unit cells in a supercell configuration, we use the calculated global reflection phase/amplitude states as *local* quantities. This so-called "periodic" approximation is justified by the slowly varying modulation of the MS properties and is frequently used in gradient MS design with excellent results [32, 41]. To obtain the far field (radiation) pattern of the actual finite-size steering MS, we do not use a full-wave simulation setup, as it can become extremely intensive computationally for large MSs and is thus ill-suited for the scalability analysis where the geometric parameters are scaled by orders of magnitude with a huge number of possible parameter combinations. To bridge this gap, the proposed methodology employs a semi-analytical approach where, as described in detail in what follows, the unit cell response is extracted from physical full-wave simulations while the MS response is calculated analytically using the Huygens' principle.

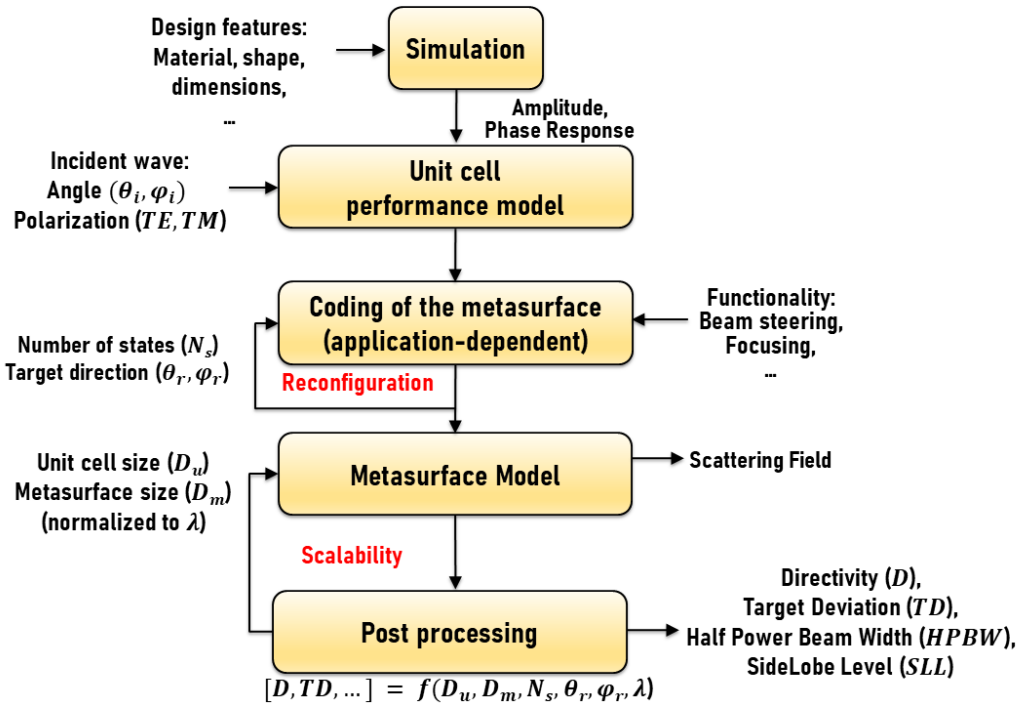

Figure 2.1: Flowchart of the proposed semi-analytic methodology for scalability analysis.

Figure 2.1 summarizes the stages of the proposed methodology. First, a unit cell is designed and evaluated with full-wave simulations. Then, reflection factors are incorporated into the analytic formulation to model the MS. Finally, by processing the scattered field, performance metrics are extracted. Without any compromise on generalization, the methodology is instantiated to study the case of anomalous reflection for beam steering applications. It can be employed to study practically any wavefront transformation by adopting the corresponding phase gradient and adjusting the selected performance metrics. Section 2.2 derives the MS optimal coding for beam steering. Section 2.3 describes MS model and Section 2.4 outlines the performance metrics. Finally, Section 2.5 validates the proposed analytical approach and MS coding method.

2.2 Metasurface coding

The direction of reflection can be engineered by an appropriate linear phase gradient [32, 39, 41]. Assuming that the MS imposes the phase profile $\Phi(x, y)$, we assign the virtual wave vector $\mathbf{k}_\Phi = \nabla\Phi = \partial_x\Phi\,\hat{x} + \partial_y\Phi\,\hat{y}$ (∂_x and ∂_y denote partial derivatives). The momentum

conservation law can be expressed as

$$\begin{aligned} k\sin\theta_i\cos\varphi_i + \partial_x\Phi &= k\sin\theta_r\cos\varphi_r, \\ k\sin\theta_i\sin\varphi_i + \partial_y\Phi &= k\sin\theta_r\sin\varphi_r, \end{aligned} \tag{2.1}$$

where $\partial_x\Phi$ and $\partial_y\Phi$ describe the imposed phase gradients in the x and y directions, respectively, and the subscripts i and r denote incident and reflected (scattered) waves, respectively.

To simulate the MS and perform the scalability analysis, the applied coding should yield the best possible performance across different physical scales. Our approach, instead of relying on fixed super-cell or meta-atom structures [64], calculates the phase gradient at the unit cell granularity and adapts the unit cells states accordingly. Therefore, we fix the unit cell size ($d_x = d_y = D_u$) and then obtain the phase required at the mn-th unit cell. Assuming air as the host medium the required phase reads

$$\Phi_{mn} = \frac{2\pi D_u(m\cos\varphi_r\sin\theta_r + n\sin\varphi_r\sin\theta_r)}{\lambda_0} \tag{2.2}$$

Subsequently, based on the number of unit cell states N_s and the phase gradient profile, the nearest available state will be mapped to the unit cell. Note that to adapt to the digital logic of the control devices, the number of states is associated to the number of bits N_b used to encode the states through $N_s = 2^{N_b}$. Depending on N_b, the phase states are separated by $\pi/2^{N_b-1}$ in the 2π range. For example, a 2-bit coding MS possesses 4 phase states ("00", "01", "10" and "11") which are 0, $\pi/2$, π, $3\pi/2$. Note that a constant phase offset for all states would not change the performance; it is the phase difference between states that is important. To illustrate the output of the coding process and the impact of the deflection angles (θ, φ) on the required phase gradients in the x and y directions, Fig. 2.2 depicts the MS phase profile for different pairs of target angles assuming normal incidence.

2.3 Metasurface model

Following the Huygens principle in the far-field limit, the MS cells can be accurately modeled as a collection of sources of secondary radiation. For linearly polarized incidence, the scattered field can be expressed as [28]

$$\begin{aligned} E(\theta,\varphi) = \sum_{m=1}^{M}\sum_{n=1}^{N} & A_{mn}e^{j\alpha_{mn}} f_{mn}(\theta_{mn},\varphi_{mn}) \\ & \Gamma_{mn}e^{j\Phi_{mn}} f_{mn}(\theta,\varphi)e^{jk_0\zeta_{mn}(\theta,\varphi)} \end{aligned} \tag{2.3}$$

where φ and θ are the azimuth and elevation angles, A_{mn} and α_{mn} are the amplitude and phase of the wave incident on the mn-th unit cell, Γ_{mn} and Φ_{mn} are amplitude and phase

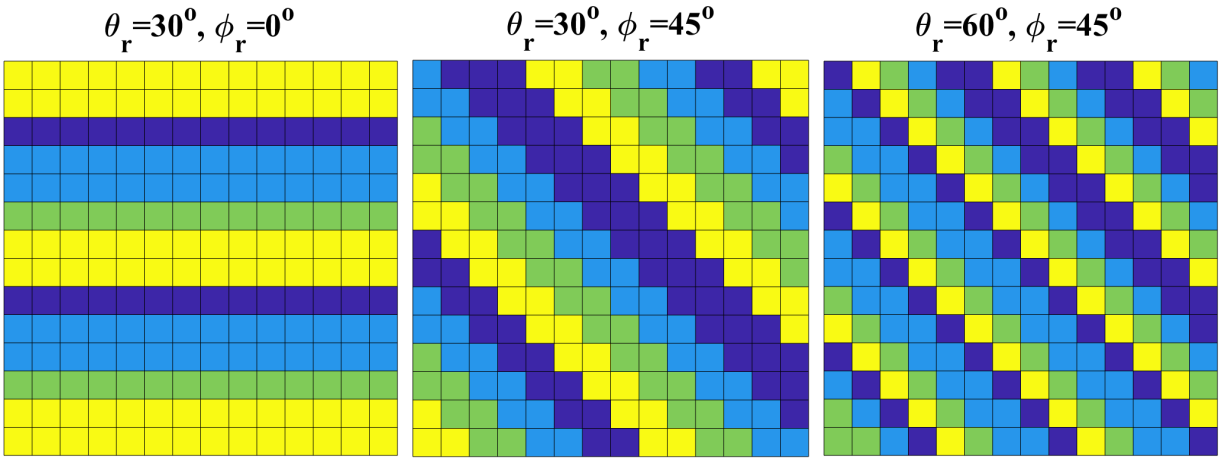

Figure 2.2: Coding of a 15×15 MS with $N_s = 4$ for different target reflection angles assuming normal incidence. Each color represents a different state (blue: 00, yellow: 01, cyan: 10, green: 11) with equispaced reflection coefficient phases.

reflection coefficient for the mn-th unit cell, and f_{mn} denotes the scattering pattern of the mn-th unit cell, which, according to reciprocity, is identical for scattering toward the (θ, φ) direction and the interception of incoming waves from the $(\theta_{mn}, \varphi_{mn})$ direction; here we assume $f_{mn}(\theta, \varphi) = \cos(\theta)$ which describes real-world dipolar scatterers. Finally, $\zeta_{mn}(\theta, \varphi)$ is the relative phase shift of the unit cells with respect to the radiation pattern coordinates, given by

$$\zeta_{mn}(\theta, \varphi) = D_u \sin\theta[(m - \tfrac{1}{2})\cos\varphi + (n - \tfrac{1}{2})\sin\varphi] \tag{2.4}$$

In summary, after evaluating the phase required at each unit cell using Eq. (2.2) and performing the nearest neighbour mapping to the available unit cell states, the amplitude and phases from the unit cell performance models are introduced in Eq. (2.3) through Γ_{mn} and Φ_{mn} to obtain the far-field pattern of the MS.

2.4 Performance metrics

The far field pattern obtained in the previous step is post-processed to obtain a set of performance metrics relevant to beam steering. We detail them next.

A Directivity ($D(\theta, \varphi)$):

A fundamental antenna parameter quantifying concentration of energy at a given direction with respect to isotropic scattering, calculated as

$$D(\theta, \varphi) = \frac{4\pi U(\theta, \varphi)}{\int_0^{2\pi} \int_0^{\pi} U(\theta, \varphi) \sin\theta d\theta d\varphi} \tag{2.5}$$

where $U(\theta, \varphi) \propto |E(\theta, \varphi)|^2$ is the radiation intensity scattered towards a given direction, and the denominator corresponds to the total scattered power. For a fully reflective MS, the elevation angle θ is limited to $[0, \pi/2]$ while the maximum Directivity is limited to $4\pi A/\lambda^2$, where A is the MS aperture area.

B Reflection Angle ($\mathbf{RA}(\theta_a, \varphi_a)$):

In beam steering case, target reflection angle (θ_r, φ_r) is the desired reflection direction where the target is located while the actual Reflection Angle (RA) (θ_a, φ_a) is the direction of the main lobe which is deviated form the target in most cases due to the inaccuracies (see Fig. 2.3).

C Target Deviation (TD):

It is measured in degrees and quantifies the difference between the target (θ_r, φ_r) and the actual (θ_a, φ_a) reflected angle due to inaccuracies in the phase profile. It is calculated as

$$TD = \sqrt{(\theta_r - \theta_a)^2 + (\varphi_r - \varphi_a)^2} \tag{2.6}$$

D Side-Lobe Level (SLL):

In addition to the main beam, a set of minor reflected beams may arise due to the phase profile of the MS and, especially, its finite aperture. The SLL is defined as the ratio (in dB) of the directivity of the side-lobe nearest to the main lobe. A low SLL is preferable to minimize scattering of energy in unwanted directions.

E Side-Lobes Accumulated energy (SLA):

In addition to the secondary beam, a set of minor reflected beams may appear due to the fundamental operation of MS structure. We measure the accumulation of power within these lobes and report it normalized to the power of the main beam.

F Half Power Beam Width ($HPBW$):

The waist of the main reflected beam defines the resolution of steering. The $HPBW$, measured in degrees, is calculated as the square root of the solid angle at the -3 dB of a lobe maximum. Low values suggest very accurate localization and tracking, whereas high values suggest diffuse scattering or higher angular coverage.

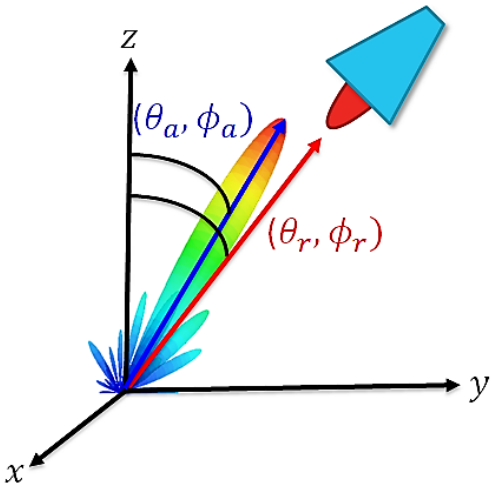

Figure 2.3: Discrimination between the target angle (θ_r, ϕ_r) and the actual reflected angle (θ_a, ϕ_a).

2.5 Validation

The accuracy of the proposed semi-analytical method is verified through a comparison with full-wave simulations in CST Microwave Studio [84] by assuming an MS with dimensional parameters $D_u = \lambda/3$ and $D_m = 5\lambda$ and a target reflection angle $\theta_r = \varphi_r = \pi/4$ under normal plane-wave incidence. Unit cells are simply modeled as lossless dielectric with different Permittivity to provide maximum reflection amplitude and required phase profile. Even though the unit cell design is simple, one single simulation takes 40–70 minutes in a high-end workstation while proposed method estimates the radiation pattern within 1–2 minutes. As shown in Fig. 2.4 the semi-analytical method is in excellent agreement with the full wave simulation (97% accuracy).

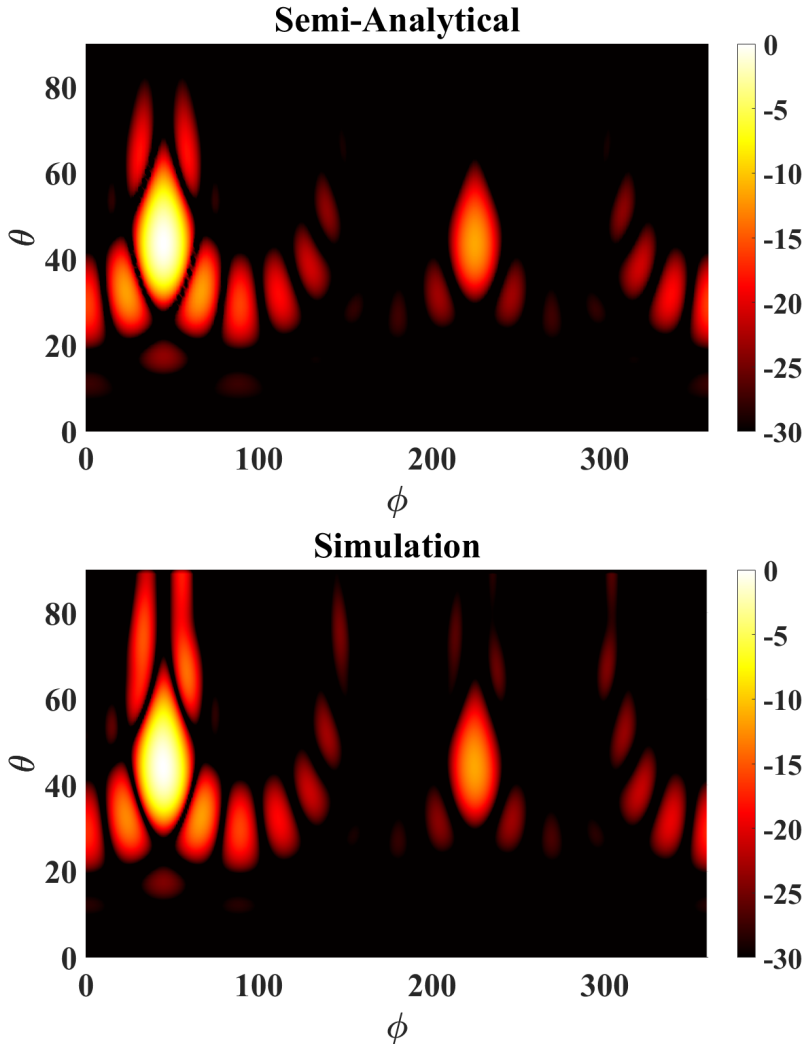

Figure 2.4: Normalized power radiation (E-Field, dB) of the programmable MS while targeting $\theta_r = \varphi_r = \pi/4$, calculated with our method (top) and full-wave simulation (bottom). Excellent agreement is observed.

Chapter 3

The Metasurface Scalability versus Design Space

The design of programmable MS faces significant challenges in terms of complexity due to the many aspects involved, including but not limited to the unit cell design, the placement of the tuning elements and its impact on the unit cell response, the tuning range requirements, the integration of driving methods within the MS structure, or the associated extra fabrication steps [44]. Furthermore, mapping all these design aspects to the requirements of the functionalities to be implemented by the programmable MS is an arduous task.

In the pathway to dimension a programmable MS for a given functionality, a key question is then: **how do the MSs scale?**. In more detail, we should try to know how do MSs scale in terms of performance for the target functionality. Thus, a scalability analysis would inspect the impact of each design parameter to the MS performance.

This chapter revolves around the concept of scalability analysis of RISs, in an attempt to provide tools to derive general considerations and guidelines of design for future MSs. For instance, a clear outcome of this analysis would be the answer to the question:

- **which is the minimum number of unit cells, number of states per unit cell, and maximum unit cell size that guarantee a given performance for a given EM functionality?**

In the pathway to answering this question, we will face several tradeoffs that we can navigate easily thanks to the analytical modeling of the MS. For instance, we shall be able to answer the (also pertinent) question, among many others:

- **is it preferable to improve in terms of discretization of the space (with smaller unit cells) or in terms of quantization of the phases (with more**

states) to comply with the requirements of a given application?

Coupled to complexity or cost models, or tied to other tools such as information theory methods [85, 86], the scalability analysis could clarify the practicable space of RIS design, illustrating the main design tradeoffs and delimiting optimal design regions. In particular, the chapter applies the methodology developed in Chapter 2 for scalability analysis for a representative functionality like anomalous reflection i.e., beam steering.

This chapter aims to lighten the burden of programmable MS designers by studying the main scaling trends of reconfigurable MS. Through a design-oriented scalability analysis, our goal is to obtain a good understanding of the potential performance of programmable MS as a function of critical design parameters. The rest of the chapter is structured as follows. The scaling model is described in Section 3.1. The assumed unit cell model is described in Section 3.2 and the results of the scalability analysis are given in Section 3.3. The impact of the incident and deflection angles are investigated in Section 3.4 and a discussion of the contradicting trends between performance and cost is delivered in Section 3.5.

3.1 Scaling model

This section outlines the scaling model proposed for MSs. The model distinguishes between factors that relate to the MS geometry, Section A, as well as the ability to program the MS to match a given application-specific parameter, Section B. The model is general, but instantiated here for the case of beam steering. Figure 3.1 shows a schematic representation of the system under study. We assume that MSs are deployed to direct reflected rays to a particular user. Each MS has a lateral size of D_m and is composed by a set of reconfigurable unit cells of size D_u. The unit cells are driven by a set of controllers, whose function is to choose the states $S_{mn} \in \Sigma$, $\forall m, n$ that will allow to point waves impinging from incidence angles (θ_i, φ_i) towards a given direction described by (θ_r, φ_r). Due to the limited number of states that the unit cells can adopt, i.e. $|\Sigma| = N_s$, the theoretically required reflection phase modulation along the MS may not be exactly satisfied, leading to deviations in the reflection direction, i.e. (θ_a, φ_a) instead of (θ_r, φ_r), the appearance of side lobes, etc. In what follows, the main parameters are described in more detail.

A Dimensional factors

Size of the unit cell (D_u): The unit cell dimensions commonly depend on the desired frequency regime as they need to be subwavelength. Beyond that, and since the MS is spatially discretized on a unit cell granularity, the size of each unit cell will have an impact

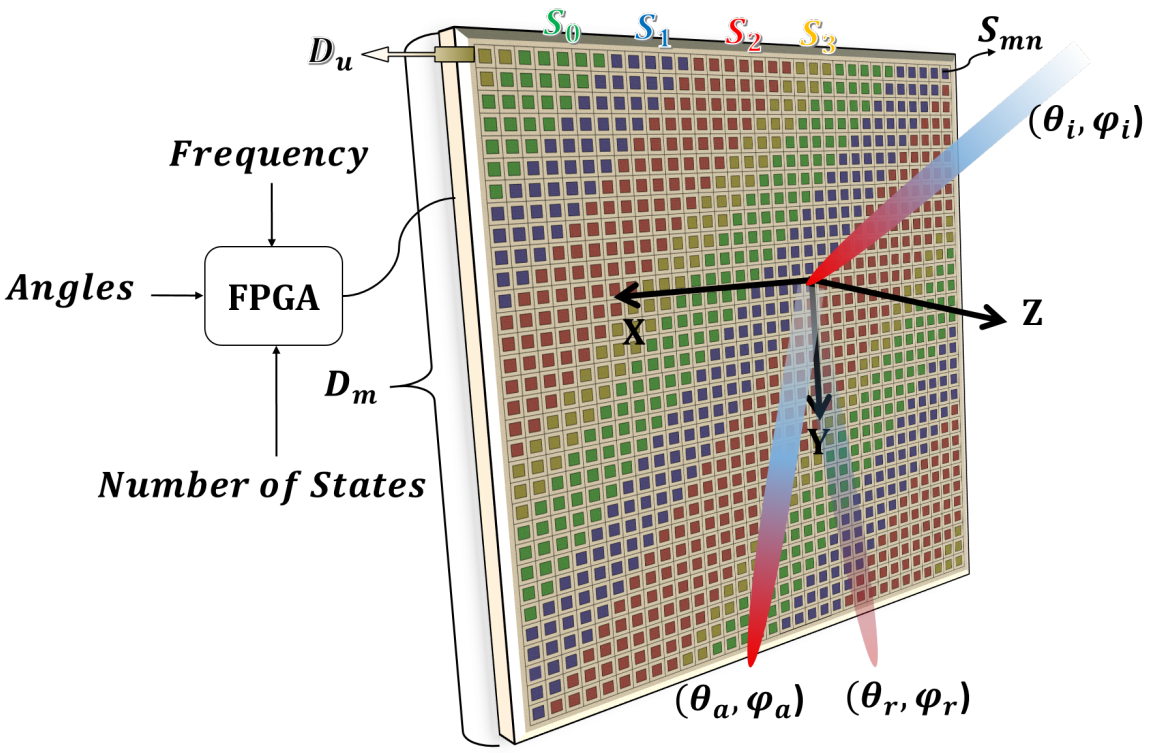

Figure 3.1: Schematic representation of a programmable metasurface implementing a phase gradient for beam steering with unit cells of size D_u and N_s possible states (S_0, S_1, S_2, S_3).

on the MS performance. Here, without loss of generality, we assume square unit cells of side D_u.

Size of the metasurface (D_m): The size of the MS determines its aperture and ability to coat objects or walls, as well as its cost. Here, we assume that the MS covers a square area with lateral size of D_m. With D_m and D_u, one can calculate the number of unit cells.

Wavelength (λ): From the EM perspective, determining the frequency band of interest is critical to tackle the design of the unit cell. In the case of RIS-enabled communications, λ corresponds to the wavelength in the medium enclosing the MS, typically air. In our study, instead of adding frequency as another parameter, we express the dimensions normalized to the wavelength in order to give a clear and general vision over the frequency-to-dimensions relationship.

B Programming parameters

Number of unit cell states (N_s): Ideally, a programmable MS would have continuous control over the local phase and amplitude of the unit cell responses. However, complexity

issues related to the tuning elements and their driving methods often suggest discretizing the amplitude-phase states of the unit cells. The parameter N_s that models the number of possible unit cell states is decided at design stage and cannot be modified at runtime. The discretization imposed by the finite number of states will have an impact on the MS performance. Note that, as will be shown in Sections 3.2 and B, a pool of available states larger than N_s is in generally needed, from which the optimum N_s states are chosen for each specific case. This is useful for example for combating the effect of varying incidence angle on the steering performance.

Target direction (θ_r, φ_r): As any reflectarray, programmable MSs for beam steering naturally have the direction of reflection as the main input. We express the direction using the spherical notation (θ_r, φ_r) as the position of the intended receiver can be easily expressed in spherical coordinates (r, θ, φ) as well, using the MS as point of reference in the coordinate system as shown in Fig. 3.1. Without loss of generality, we assume plane wave incidence and a distant receiver, which allows to define the position of the receiver with $\{\theta_r, \varphi_r\}$ only. The model, however, would admit arbitrary wavefront shapes if necessary.

Incidence angle (θ_i, φ_i): The unit cell states leading to the desired reflection direction also depend on the angle of incidence. With the assumptions made above, the incidence is fully defined by angles (θ_i, φ_i) as shown in Fig. 3.1. Again, if needed, the model would admit arbitrary wavefront shapes. We note that, while the number of states is fixed at design time, the incidence angle and target direction will be generally time-variant in RIS scenarios. For instance, a RIS designed to add beams coherently at the receiving end will need to adapt the incidence and reflected angle to the positions of the transmitters and receivers.

3.2 Unit cell performance model

In this section, we propose a reconfigurable unit cell for operation in reflection, Fig. 3.2. A square unit cell ($a = 4$ mm) with a metallic back plane is designed to resonate at 26 GHz, a band of great interest for 5G applications, and thus provide the necessary 2π phase delay for implementing wavefront control based on the Huygens' principle. We stress that this physical concept is independent of the adopted physical system and frequency range; for example, a dielectric meta-atom can be used for providing a resonance in the near/far-infrared, or a plasmonic meta-atom for a resonance in the optical regime. A square metallic patch ($w = 3.92$ mm) is stacked on top of a substrate made of Rogers RO4003C high-frequency board material with permittivity $\epsilon_r = 3.38$ and thickness $h = 0.203$ mm. The reconfigurability is voltage-controlled and stems from varactor elements properly incorporated in the unit cell, Fig. 3.2(c). More specifically, through vias connect the rectangular patch to four varactors

residing behind the backplane inside an integrated chip, making it possible to tune the surface impedance of the MS and, thus, the local reflection phase and amplitude. The four vias are positioned in a symmetric fashion near the four corners of the patch, with a distance from the unit cell center along both axes of $b = 1.5$ mm, and have a diameter $d = 0.1$ mm. The ground of the chip is connected with the MS backplane via a metallic post in the center of the unit cell, Fig. 3.2(c). The four varactors are collectively set to the same capacitance value C_{var}; they are used instead of a single varactor at the center of the unit cell [41] in order to enhance the impact of varying capacitance over the surface impedance (induced currents are maximized at the edges of the patch) while retaining an isotropic unit cell (same behavior along both Cartesian axes).

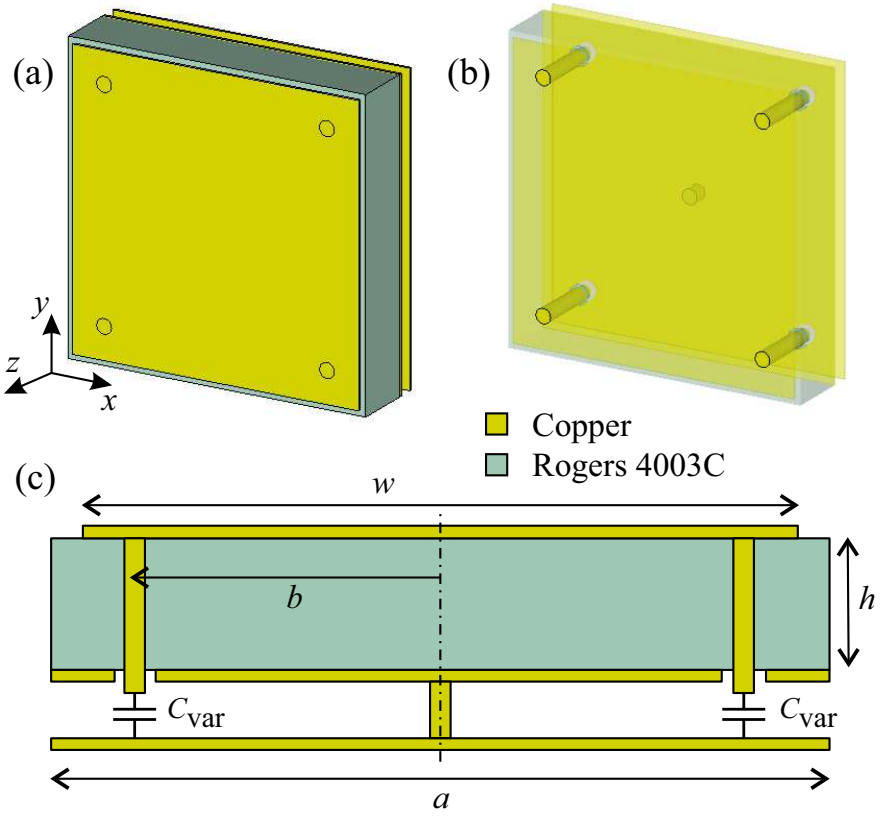

Figure 3.2: Schematic of unit cell for operation at 26 GHz. (a,b) Bird's eye views indicating the positions of the through vias and the shorting post connecting the chip ground with the MS backplane. (c) Cross-section with annotations of geometric parameters and the varactor capacitances.

For providing reconfigurable steering performance, we will combine unit cells of different reflection phase states; e.g. for the case of two-bit coding we use four different states equidistantly spanning the 0–2π range, i.e. with values $\{135, 45, -45, -135\}$ degrees. They can be

achieved with specific values of the varactor capacitances C_{var} by means of an appropriate biasing voltage. In Fig. 3.3 we depict the reflection phase, Fig. 3.3(a), and reflection amplitude, Fig. 3.3(b), of the proposed unit cell, as calculated by full-wave simulations of the unit cell for normal incidence. The required reflection phase states are attained for varactor capacitances $\{0.26, 0.29, 0.31, 0.33\}$ pF. At the same time, the corresponding amplitudes are high and quite uniform; absorption is maximized on resonance and thus it is unavoidable that certain capacitance values that bring the MS resonance closer to 26 GHz will be associated with smaller reflection amplitudes. The designed phase states can be used to steer a reflected beam towards the desired direction; the performance of this operation will be thoroughly assessed in the following sections. Note that although designed for a specific pitch value $a \equiv D_u$, the proposed unit-cell extent can be scaled and still function around the target frequency of 26 GHz by modifying the required varactor capacitances or, equivalently, the bias voltages.

Next, we investigate the effect of oblique incidence for both Transverse Electric (TE) and Transverse Magnetic (TM) polarizations. Specifically, it is expected that the attained reflection phase will depend on the incident angle. This means that the aforementioned capacitance values will provide suboptimal reflection phase as the incidence angle varies. Having at our disposal a different set of four phase states (for the case of two-bit coding) can help in retaining excellent performance for different incidence angles. This is shown in Fig. 3.3, where the reflection phase as a function of capacitance is depicted for incidence angles of 30 and 60 degrees, for TE [Fig. 3.3(b)] and TM [Fig. 3.3(c)] polarization, respectively. By selecting each time the best four out of a total of 16 available states enables us to retain almost perfect performance for all the cases investigated in Fig. 3.3. It is worth noting that our model of varactors simply have only capacitance while in practice varactors have small values of resistance. Nevertheless, electrical resistivity only reduces the reflection amplitude from the unit cell. The reflection phase span remains mostly unchanged and the required values can be obtained with minor changes in the capacitance.

3.3 Performance Scalability

The evaluation of a beam steering system relies on multiple metrics. Here, we obtain the directivity D, side-lobe level SLL, half power beam width $HPBW$ and target deviation TD as functions of the unit cell size D_u, MS size D_m, and number of states N_s. The parameters are swept by at least an order of magnitude by the definition of scalability analysis. Evidently, some parameter combinations and regions will be unfeasible or *de facto* unacceptable, by virtue of reflect-array principles; nevertheless, this helps to better identify

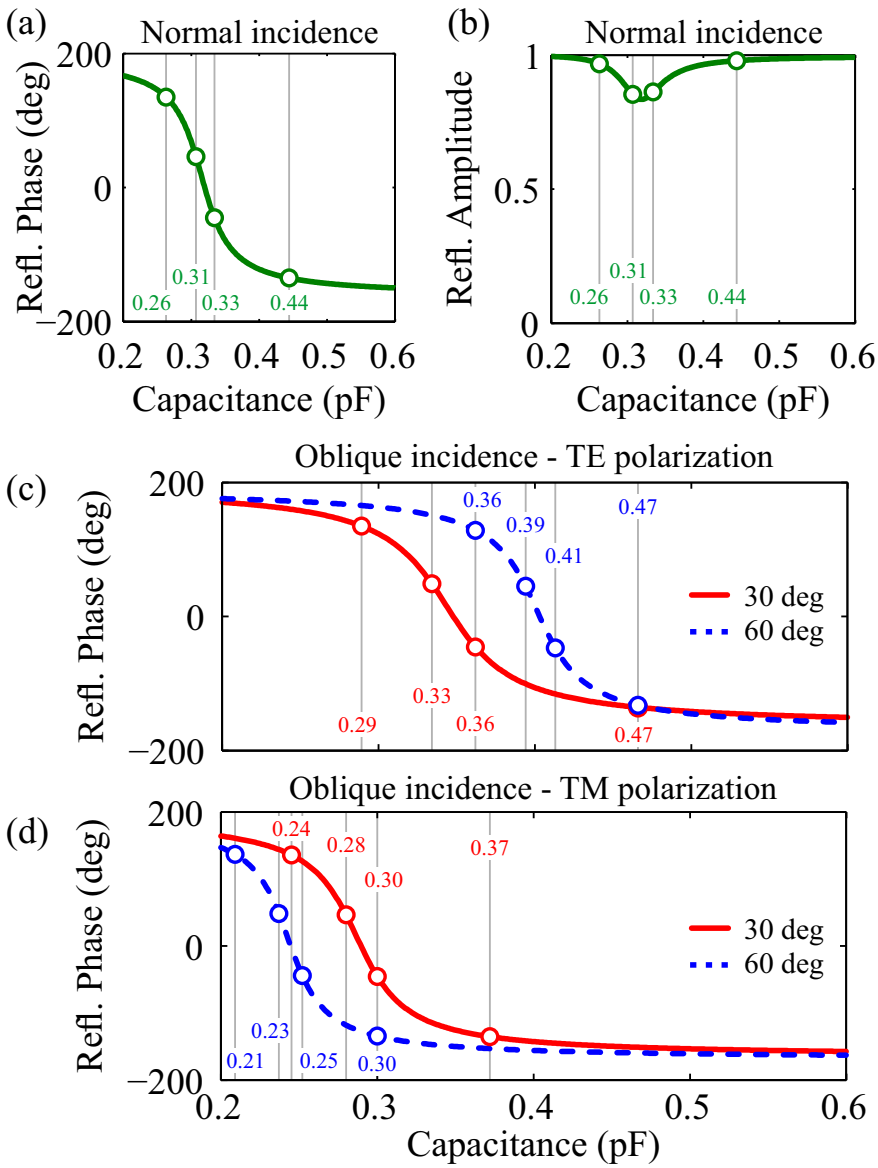

Figure 3.3: (a) Reflection phase and (b) amplitude for the proposed unit cell under normal incidence as a function of capacitance. The four capacitance values leading to reflection phase $\{135, 45, -45, -135\}$ degrees are marked. (c) Reflection phase as a function of capacitance for TE polarization and incidence angles 30 and 60 degrees. The capacitance values for the desired four phase states are marked. (d) Reflection phase as a function of capacitance for TM polarization and incidence angles 30 and 60 degrees. The capacitance values should for the desired four phase states are marked.

the frontier between relevant and irrelevant design spaces, and highlights the shortcomings of the latter to a broader audience. To present comprehensive results, we normalize the dimensions to the incident wave wavelength (λ). This way, the reasoning is applicable to

any frequency as long as the scaled unit cell is redesigned to offer the required amplitude-phase response[1]. Also, the reported results are for particular target angle $\varphi_r = \theta_r = \pi/4$ and normal incidence. The effect of the incidence and target angles on the performance of the MS is discussed later in Section 3.4.

A Directivity

We first assess the directivity in the direction of maximum radiation (θ_a, φ_a) as a function of the three input parameters D_u, D_m, and N_s. Figure 3.4 shows how the directivity scales with respect to D_u/λ and D_m/λ for three representative values of N_s corresponding to 1-bit, 2-bit, and 3-bit coding. It is observed that the directivity increases with the MS size. For instance, for $N_s = 4$, we see a consistent increase of 15 dB when moving from $D_m = \lambda$ to $D_m = 3\lambda$. The improvement diminishes from there, yet an additional 10 dB can be achieved when moving from $D_m = 3\lambda$ to $D_m = 10\lambda$. The impact of the unit cell size is only appreciable above $D_u = \lambda/2$. Reducing the size further does not improve the directivity of the MS, therefore discouraging the use of small unit cells due to the associated raise of the fabrication complexity and cost.

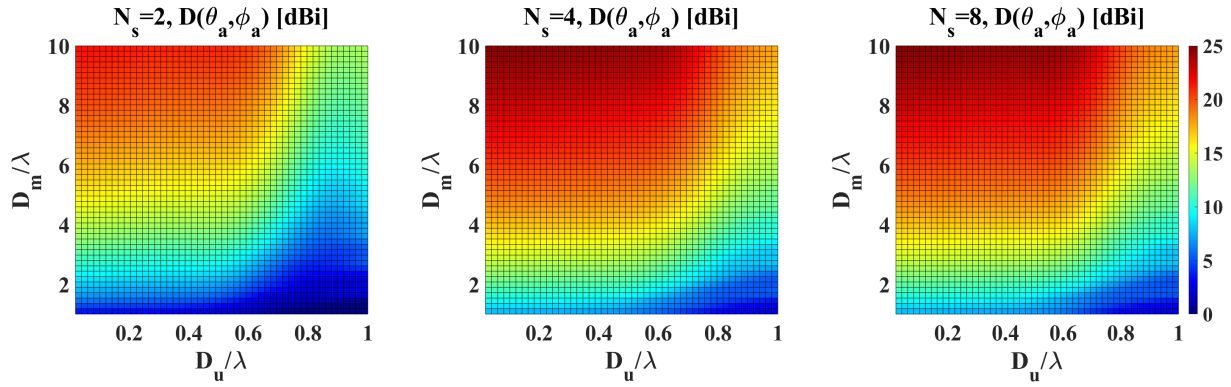

Figure 3.4: Directivity at the direction of maximum radiation $D(\theta_a, \varphi_a)$ for $\varphi_r = \theta_r = \pi/4$ as a function of the dimensional parameters for 1-bit, 2-bit and 3-bit coding. The color bar is common to all figures.

The impact of the number of states is especially noticeable as we move from $N_s = 2$ to $N_s = 4$, with a general improvement of ∼3 dB. The main reason behind this behavior is that, for $N_s = 2$, the reflected wave is split into two identical lobes directed to two symmetrical angles and, therefore, half of the power is lost. This behavior disappears when introducing

[1]Note that the unit-cell phase shifts needed for beam steering have been demonstrated across the spectrum [24–26].

the second bit of coding, which explains the 3 dB difference. Adding a more states beyond $N_s = 4$ bit does not have a significant impact.

B Target Deviation

Figure 3.5 shows the scaling trends of the TD, which we generally aim to minimize in order to achieve high steering precision. Here, we consider 10 degrees to be the maximum admissible deviation, although we will see that such interpretation will depend on the beam width as well. The results in Figure 3.5 demonstrate that TD depends greatly on all the evaluated

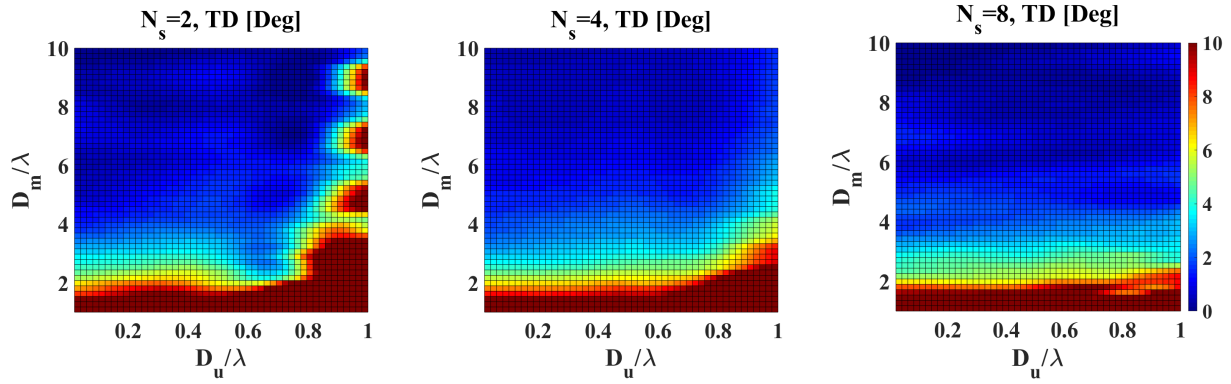

Figure 3.5: TD as a function of dimensional parameters for 1-bit, 2-bit, and 3-bit programmable MSs targeting $\varphi_r = \theta_r = \pi/4$. The color bar is common to all figures.

scaling factors. Downscaling the unit cells diminishes the target deviation of the MS because this implies that the MS is programmed at a finer spatial resolution. However, as in the case of directivity, we observe diminishing results as we reach values around $D_u = \lambda/3$. The impact of the phase quantization error, this is, when increasing the number of states, is also similar than in the directivity case: the improvement is appreciable as we move from $N_s = 2$ to $N_s = 4$, but marginal beyond that. Finally, we note that the impact of the MS size D_m is significant only for MS with relatively large unit cells. This implies that one can achieve reasonable steering precision with small MSs as long as the unit cells are also small.

C Half Power Beam Width

The spatial resolution of a steering MS is generally inversely proportional to the $HPBW$, which we aim to reduce. Figure 3.6 shows how the $HPBW$ is mainly affected by the MS size. This is because the aperture of the device is effectively increased. The improvement is very clear for $D_m < 4\lambda$, to the point that values below 15° are consistently achieved for

$D_m \geq 6\lambda$. For a MS of $10\lambda \times 10\lambda$, the $HPBW$ is reduced down to around 5º. On the other hand, the impact of the unit cell size and number of states is negligible in this case.

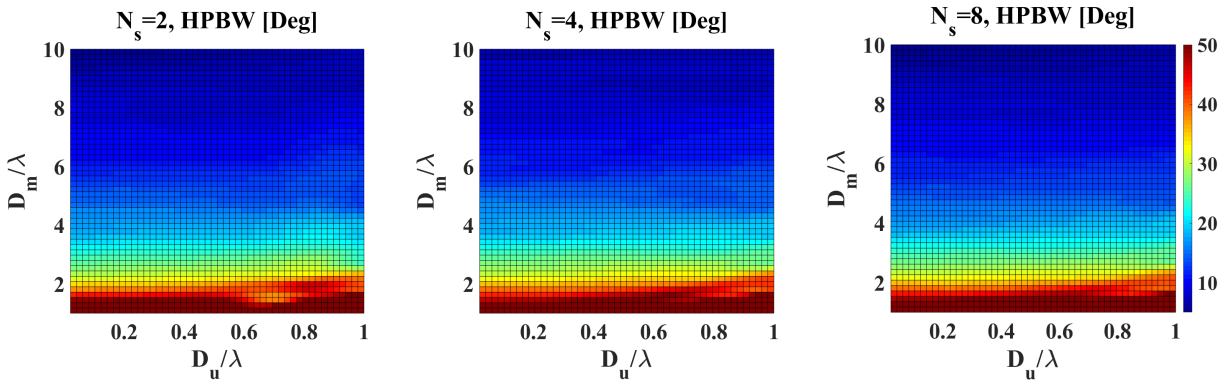

Figure 3.6: HPBW as a function of dimensional parameters for 1-bit, 2-bit, and 3-bit programmable MSs targeting $\varphi_r = \theta_r = \pi/4$. The color bar is common to all figures.

D Side Lobe Level

The evaluation of the SLL is a good first-order estimation of the power that may be off-target and interfere with nearby communications. Figure 3.7 shows the scaling tendencies of SLL. Remind that $N_s = 2$ is a particular case where the scattered field is split into two identical beams, which would lead to $SLL = 0$ dB throughout the design space. Therefore, for this case, we calculate the SLL with respect to the third lobe. For $N_s = 4$ and $N_s = 8$, the SLL is evaluated as usual. Figure 3.7 essentially proves that the unit cell size is the main determinant of SLL. We can clearly observe how $D_u = \lambda/2$ marks a frontier between a region of good performance in terms of SLL with values below -12 dB from a design space with SLL in excess of -9 dB. It is also worth remarking that, unlike the rest of metrics, the SLL keeps improving as we introduce a third bit of coding ($N_s = 8$). This reinforces the intuition that the SLL is mainly affected by errors in the discretization and quantization of the space-phase. We finally note that, although the MS size does not have a significant influence on this metric, we could compensate the existence of large unit cells with enough unit cell states in large MSs.

3.4 Impact of Input/Output Angles on Performance

In this section we will investigate the impact of reflection direction on the steering performance metrics for MS with (i) variable aperture and cell size, but ideal unit cell response

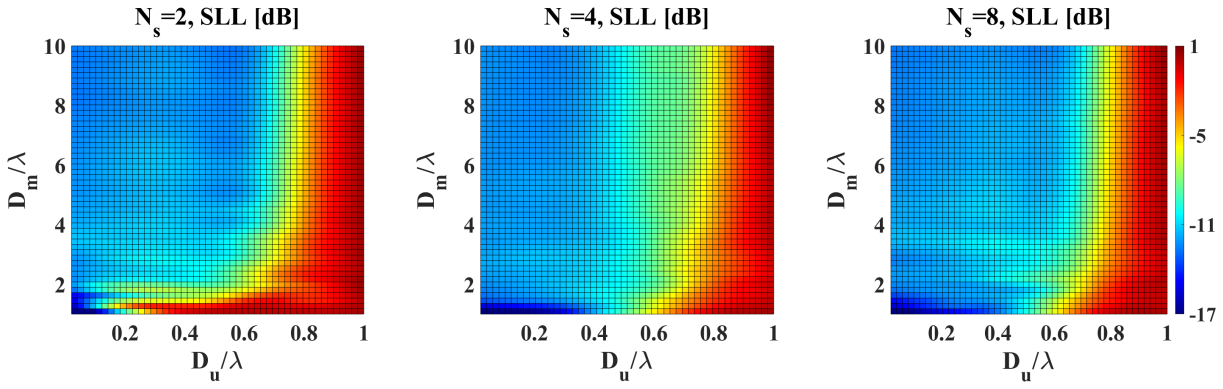

Figure 3.7: SLL as a function of dimensional parameters for 1-bit, 2-bit, and 3-bit programmable MSs targeting $\varphi_r = \theta_r = \pi/4$. Side-Lobe Level is normalized to the maximum across all MSs. The color bar is common to all figures.

across all angles in Section A; and (ii) using a realistic (physical) implementation for the unit cells in Section B. This way, we differentiate between the performance degradation caused by the MS at large or by individual unit cells. Exploiting the rotational symmetry of the structure and the inherent reciprocity of the EM problem, only a subset of all combinations of incidence (input) and reflection (output) directions needs to be analyzed. Moreover, as highlighted in the previous section, four phase states are sufficient for the basic steering functionality so will limit our simulations to this case and briefly comment on the higher-state cases.

A Impact on Metasurfaces with Ideal Unit Cells

We will start by assessing the effect of aperture and cell size on the performance of 4-state MS with ideal unit cell response for a few different scenarios. To this end, normalized 2D (E-plane) scattering patterns are presented in Fig. 3.8; the plots correspond to steering from normal incidence to two reference directions, namely $\theta_r = 30^o$ and 60^o, while $\phi_r = 45^\circ$ in both cases. Moreover, we consider three cell sizes $D_u = \{\lambda/2, \lambda/4, \lambda/10\}$ for a fixed aperture $D_m = 5\lambda$, and then three apertures $D_m = \{3\lambda, 4\lambda, 10\lambda\}$ for a fixed cell size $D_u = \lambda/3$. The resulting patterns clearly illustrate that targeting elevated angles (near zenith) leads to better results, due to their proximity to the specular reflection direction; in contrast, targeting ground-level (grazing) reflection angles, significant side lobes appear while the main lobe becomes wider, due to the 'steeper' phase gradients applied across the MS. The results also re-iterate our previous conclusions on the effect of aperture and cell size, now confirmed for various reflection directions: higher apertures always improve (reduce) the HPBW whereas smaller cells always improve (reduce) the SLL. Note that the maximum

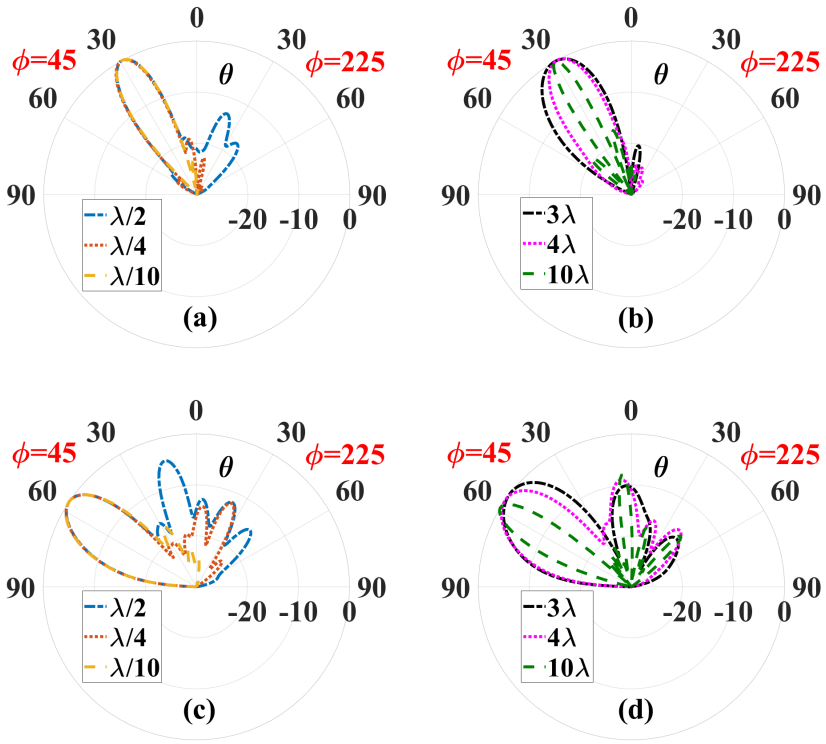

Figure 3.8: Normalized 2D/E-plane scattering patterns of ideal 4-state MS steering normally incident plane wave to $\theta_r = 30°$ (a–b) and $\theta_r = 60°$ (c–d). Panels (a) and (c) are for different unit cell sizes at fixed aperture $D_m = 5\lambda$, whereas panels (b) and (d) are for different apertures with fixed cell size $D_u = \lambda/3$.

directivity also increases with aperture (not shown in these normalized plots). To generalize the example presented above, we repeat the analysis for multiple steering directions to the upper hemisphere and, in each case, evaluate the directivity as a representative performance metric. Hence, we extend previous works [87–89] where only a set of discrete angles were studied, as the analysis of the complete angular space is extremely time-consuming unless analytical methods are used to focus on the scaling of the dimensional parameters instead. Figure 3.9 plots the normalized directivity when steering from normal incidence to: $\theta_r = 0 \rightarrow 90°$, and $\varphi_r = 0 \rightarrow 45°$. The region for which the normalized directivity is above a certain value is considered the coverage zone of the MS. Our analysis also amounts for variable cell and aperture size: $D_u = \lambda/3$, λ /10 and $D_m = 5\lambda$, 7λ, 10λ. We confirm that the performance is consistently better in directions close to the specular reflection (normal, in this case) and get worse as we approach steering directions close to the MS plane. The azimuth angle has a smaller influence on the performance.

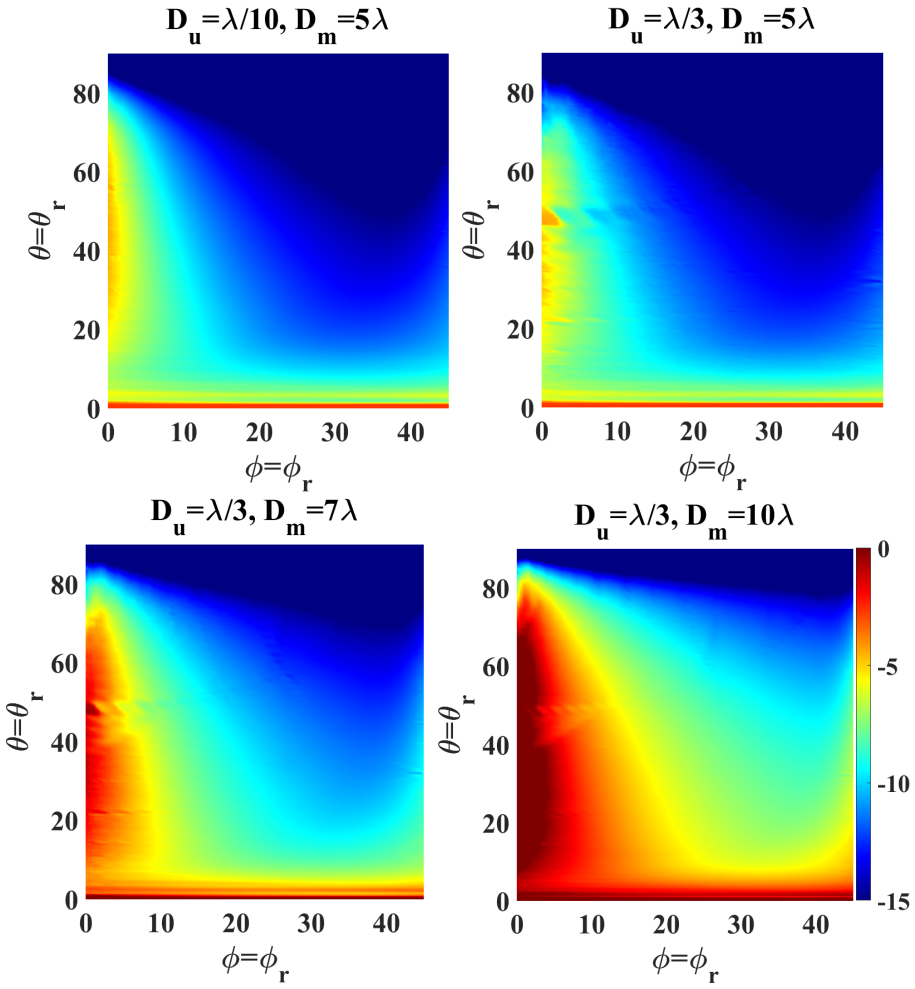

Figure 3.9: Normalized directivity when steering a normally incidence plane wave to any direction in the quarter-hemisphere. Each of the four panels corresponds to a different unit cell (D_u) and aperture size (D_m) combination. In all cases, we assume four ideal phase states, i.e., 2-bit encoding of the MS.

B Impact on Metasurfaces with Realistic Unit Cells

Here, we consider a fixed MS of $D_m = 5\lambda$ aperture composed of the realistic unit cells designed in Section 3.2; these are 4 mm wide, i.e., $D_u \approx \lambda/3$ for $f \approx 25$ GHz. We consider wave incidence from three directions, $\theta_i = \{0, 30°, 60°\}$ and $\varphi_i = 0$ in all cases. For this MS, we calculate the performance metrics as a function of the reflection direction requested, $\theta_r = 0$ to 85° and $\varphi_r = 45°$, after mapping the required phase-profile for each steering scenario onto the four available states. Note that the steering scenario that we selected corresponds to off-plane retro-reflection, which is more demanding compared to scenarios like in-plane steering or steering close to the specular reflection. The resulting curves presented in Fig. 3.10(a)-(d),

including also the absolute limit values corresponding to ideal (continuous) phase profiling, indicate that the realistic unit cell design is capable of almost optimal performance for slightly oblique incidence, with respect to the directivity, HPBW and TD metrics; performance degrades with increasing θ_r (steering further away from specular direction) and θ_i (coming closer to grazing incidence), while the curves are generally monotonic and smooth. The notable exception is SLL which diverges from the ideal trendline even for the reference case of normal incidence; this is attributed firstly to the relatively large unit cell, secondarily to the 'nearest neighbour' staircasing used to optimally map the continuous phase profile to the given fixed states for each steering direction, and, finally, to our post-processing algorithm which takes into account only the highest directivity side lobe, in whichever direction it might appear. For this fixed MS and demanding steering scenario, the performance breaks down for $\theta_i = 60°$ and $\theta_r > 30°$, due to the strong presence of a parasitic lobe in the specular direction; this can be visualized in Fig. 3.10(e) and (f), depicting the scattering patterns acquired for slightly oblique and highly oblique incidence, respectively, when the steering direction is $(\theta_r, \varphi_r) = (45°, 45°)$. Increasing the pool size of the available phase states (capacitance values), from 4 to 8 or 16, would lead to progressively better performance, i.e., all metric curves would get closer to the ideal profile curves, even for highly oblique incidence. As discussed in Section 3.2, this improvement is due to the higher reflection-phase span (coverage) that can be attained with optimal selection of capacitances from a finer-resolution and/or wider pool. Finally, note that owing to the adopted unit cell design approach, the overall performance is better as the incidence angles decreases (closer to zenith), while TE polarization behaves better than TM; however, the unit cell can in principle be designed for any reference case, e.g., for TM polarization and/or for highly oblique incidence.

3.5 The HyperSurface Energy Footprint, Cost and Performance

This section aims to illustrate how the proposed methodology can be leveraged to guide the dimensioning of programmable MSs. Section A discusses the extraction of design guidelines from the exploration, Section B exemplifies the use of combined figures of merit to delimit the practicable design space, and Section C describes how cost could be introduced in the exploration.

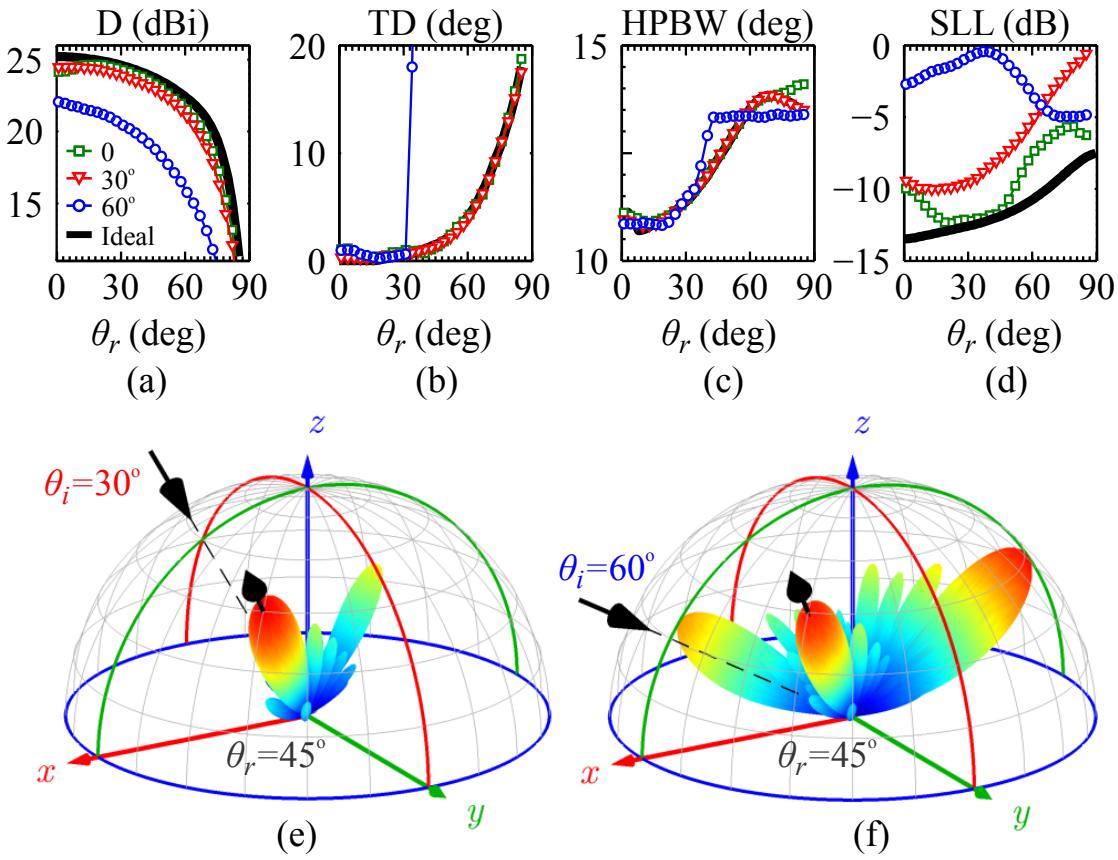

Figure 3.10: Realistic MS performance metrics as a function of steering direction $(\theta_r, 45°)$ and three incidence directions, $(\theta_i,0)$. (a) Directivity at θ_r, (b) Target deviation, (c) HPBW, (d) SLL. The thick black curves correspond to the ideal case of continuous phase profiling of the MS. Logarithmic-scale 3D scattering patterns for two reference cases, (e) $\theta_i = 30°$ and (f) $\theta_i = 60°$, targeting steering to $\theta_r = 45°$ in both cases. The MS has $D_m = 5\lambda$, $D_u = \lambda/3$ and its non-ideal states (amplitude and phase of reflection coefficients) are four, corresponding to four capacitance values.

A Extracting Design Guidelines from Performance

As expected, previous sections have confirmed that large MSs with small discretization error (unit cell size tending to zero) and phase quantization error (large number of unit cell states) consistently yield the best performance for beam steering. However, the trends depend much on the performance metric and some metrics have clear *frontiers* where performance increases abruptly. For instance, we have seen that, as expected, unit cell sizes below $\lambda/2$ are required to achieve reasonable directivities and side-lobe levels. The scaling trends with respect to the number of unit cell states lead to less anticipated results. It has been observed that at least four states ($N_s = 4$) are needed to achieve high-quality steering performance and that,

while additional bits help in suppressing the side-lobe level and increasing the directivity, the improvements soon saturate. We have also seen that having a larger pool of available states is necessary to increase the angular range of the MS. In Fig. 3.3, we have shown that a pool of $4N_s$ states instead of N_s states can perfectly accommodate incidence angles of 30 and 60 degrees for both polarizations.

To illustrate our case, first, we show a graphical representation of the HSF structure in Figure 3.11. Essentially, the HSF receives external programmatic commands from a gateway controller that are disseminated to the internal control logic at the controller chips via chip-to-chip interconnects and routing logic [80, 90]. These commands contain the state (within the discrete set of possible states) that should be applied to each unit cell. The control logic translates the state into an analog value to be applied to the tuning element, e.g. the voltage applied to a varactor to achieve a target capacitance. Additionally, embedded sensors can pick up data from the environment and send it to the control logic or external devices again via the communications plane.

B Application-Specific Figures of Merit

Thus far, the study has been application-agnostic in the sense that specific performance metric combinations are not taken into account. For instance, it is a well-known problem that, although narrow beams provide high efficiency and may be in fact necessary in some SDM/RIS-enabled scenarios [91], slight target deviations can lead to loss of connectivity. Wider beams are less efficient, but also less prone to disruption. The methodology presented in this Chapter can help reason about multiple design decisions, thereby delimiting the practicable design space, when putting different performance metrics together and introducing user requirements. For instance, beam steering for 5G communications will generally demand low beamwidth with low side-lobe level to minimize interference. Let us assume, as a practical case, a scenario where the necessary quality of experience is achieved with a $HPBW$ of 20 degrees with ± 5 degrees of tolerance and a SLL of -13 dB with ± 2 dB of tolerance. In this context, we could define a figure of merit that encompasses both requirements.

Although a formal definition of such a figure of merit is outside the scope of this work, we propose a particular example as follows

$$FoM_1 = 1 - w \cdot \delta(HPBW) - (1 - w) \cdot \delta(SLL) \tag{3.1}$$

where $w \in [0, 1]$ is the weight of the $HPBW$ metric and $\delta(\cdot)$ is the distance of a metric to its nominal required value, normalized to the tolerance range. We set $FoM_1 = 0$ if the design point is outside the tolerance interval. Figure 3.12a shows the FoM_1 for the conditions mentioned above for $N_s = 4$ and normal incidence. A value of 1 indicates maximum

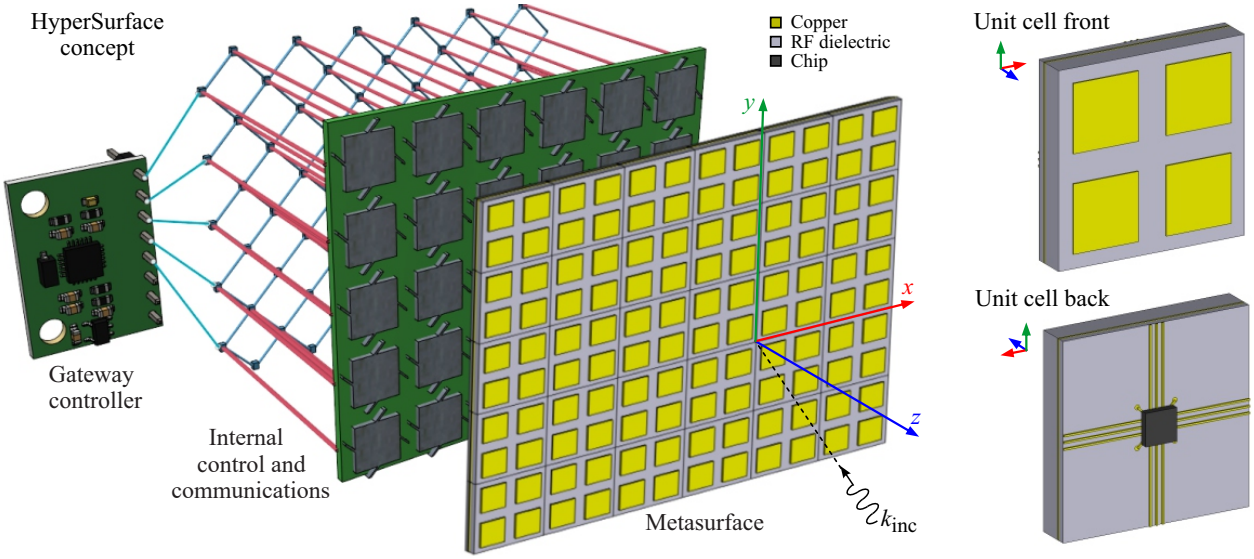

(a) Front, back, and layered representation.

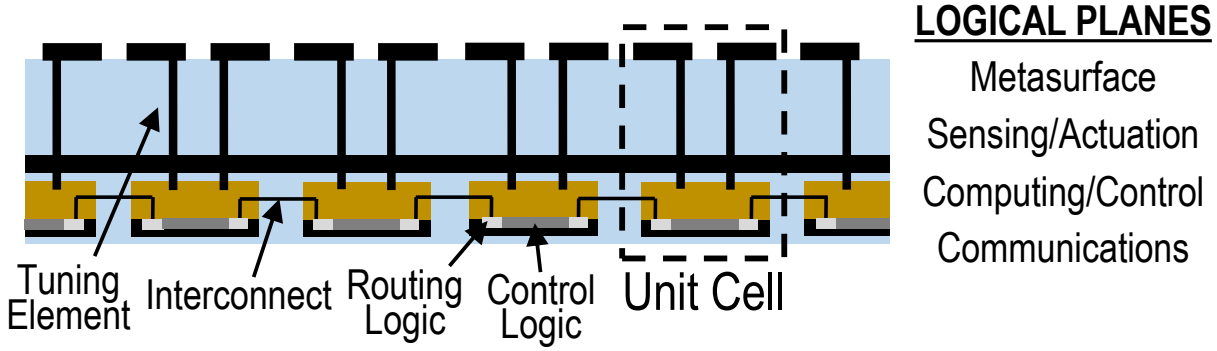

(b) Cross-section and logical.

Figure 3.11: Graphical representation of a possible HSF implementation, which includes the metasurface plane with the metallic patches and the substrate, the sensing/actuation plane with the tuning elements and sensors, the computing/control plane containing the controller chips, and the communications plane containing the routing logic and interconnects. A gateway controller interfaces the HSF with the external world. From [2].

suitability of a design point, whereas a value of 0 delimits invalid design points. In this case, values around $D_m = 4\lambda$ for $D_u < 2\lambda/5$ are a good fit for the proposed application. Making an analogy to networking provisioning, one could argue that MSs with $D_m > 4\lambda$ and unit cells of lateral size $D_u < \lambda/3$ tend to be *overprovisioned* as they perform better than the requirements set. whereas the MS is *underprovisioned* for $D_m < 3\lambda$ or $D_u > 2\lambda/5$. Finally, note that while we considered that both metrics are equally important ($w = 0.5$), architects can define their own weights depending on the application.

C Performance-Cost Analysis

It has been shown throughout this chapter, optimum performance is obtained in asymptotic cases of very large MSs with very small unit cells and a high number of states, which is clearly impractical. Although defining the application's requirement and tolerance interval helps to delimit the design space, practical design guidelines need to consider cost and complexity. To bridge this gap, parameterized models accounting for the cost or power consumption associated to integrated circuitry can be incorporated to our methodology for a joint performance-cost analysis. This would allow system architects to quantify the different tradeoffs with performance-cost figures of merit and, by adding weights to each metric, find the optimal design space for a particular budget. To exemplify the process, let us consider

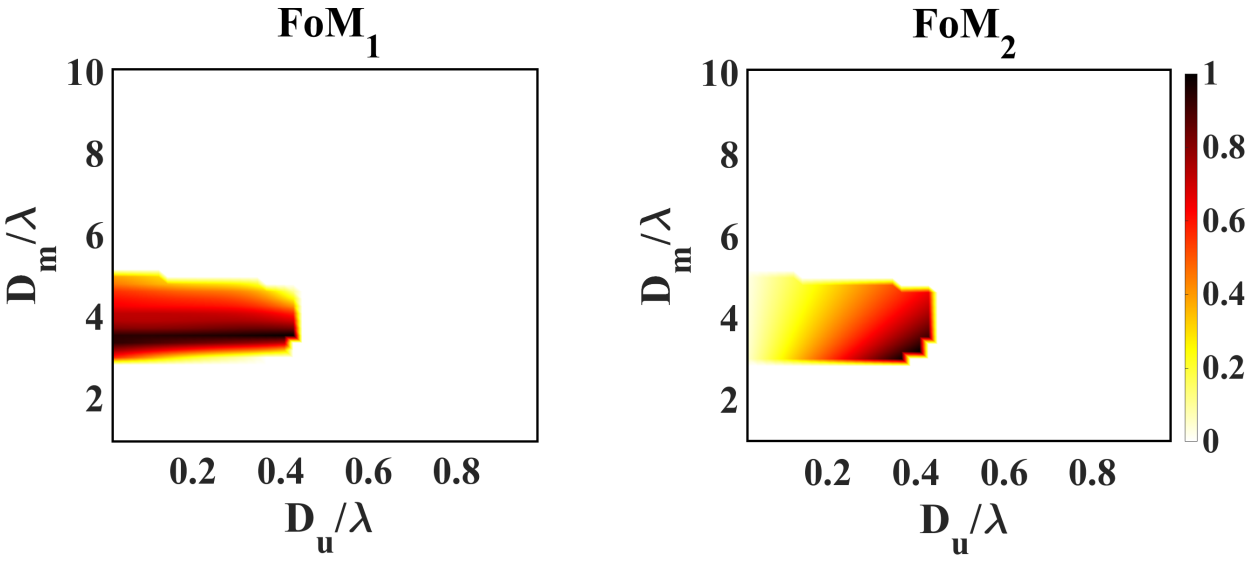

(a) Performance figure of merit.

(b) Performance-cost figure of merit.

Figure 3.12: Evaluation, through figures of merit, of a 4-state MS for beam steering with a beamwidth requirement of $HPBW = 20^o \pm 5^o$ and side-lobe level requirement $SLL = -13 \pm 2$ dB. Values close to 0 (1) refer to invalid (optimal) design points.

the example from previous section and assume that power or cost of the MS scale linearly with the number of unit cells per dimension. This assumption is backed up by recent studies analyzing the impact of adding more controllers to the amount of internal messages required to reprogram the MS [81, 90]. In our particular example, our performance-cost figure of merit is named FoM_2 and is obtained by dividing FoM_1 from Eq. (3.1) by the number of unit cells per dimension and normalizing the result. As shown in Figure 3.12, the tendency is to favor configurations with less unit cells within the range that yields good performance within the tolerance range, as the intuition would suggest.

3.6 Summary

This chapter has presented a methodology for the design-oriented scalability analysis of programmable MSs, which allows to obtain a set of performance metrics across the design space. We have applied the methodology to analyze the beam steering case, evaluating the scaling trends of the directivity, target deviation, half power beam width, and side-lobe level with respect to multiple dimensional and programming parameters. We have observed that four unit cell states (2 bits) are enough to provide acceptable performance and confirmed that, as expected, large MSs with small unit cells provide the best performance. We further confirm that the performance drops significantly as incidence or target reflection angles approach the MS plane due to a degradation of the unit cell response. From the analysis, we conclude that the $\theta_r < 60^{\text{o}}$ range is practicable for most MS designs and that, beyond that angle, increasing the amount of unit cell states may alleviate the performance degradation to some extent. Finally, we proposed the use of figures of merit that, tied to user requirements and cost models, provide an assessment of the practicable design space and optimal regions of such space in an attempt to guide the development of programmable MSs for future RIS-enabled wireless environments.

Chapter 4

Study of Errors in Metasurfaces

Adding reconfigurability to MSs comes with a non-trivial increase of the complexity that will pose new reliability challenges stemming from the need to integrate tuning, control, and communication resources. While MSs will become prone to failures, little is known about their tolerance to errors. Anticipating and modeling errors in complex systems like HSFs is an important facet, this is, as the MS gets large or dense. In the scenario of Figure 4.1, for instance, faults might lead to inaccuracies in the steering of the reflection and cause a drop in quality of service. In this context, an error analysis would also allow to derive guidelines for the implementation of robust programmable MSs, estimate the lifetime of the deployed ones, or even develop methods to save energy by power-gating a portion of the internal circuitry of the MS.

However, error analyses have not been carried out taking the particularities of MSs into consideration. In [92], the authors evaluate the impact of phase errors in RIS panels that shift the phase of impinging waves aiming for a coherent combination at the receiver. In that case, each RIS is spaced apart and treated independently, ignoring the directions of impinging or reflected waves and limiting errors to system inaccuracies, i.e. quantization and estimation error, but no faults. This resembles the classical works that analyze the impact of errors in phased antenna arrays [93–96]. Such an analysis is therefore not directly applicable to MSs, where (1) the causes of failures can be more varied due to the amount of control circuitry, and (2) the focus is on the impact of a number of failures (or the chained effect of a few of them) rather than on individual faulty components.

This chapter uses the same framework proposed in Chapter 2 to evaluate the impact of failures in programmable MSs, distinguishing between the type of faults and their spatial distribution. Despite being applicable to any EM functionality, here we use the methodology to study a beam steering MS at 26 GHz as a particular yet very relevant use case in MS-

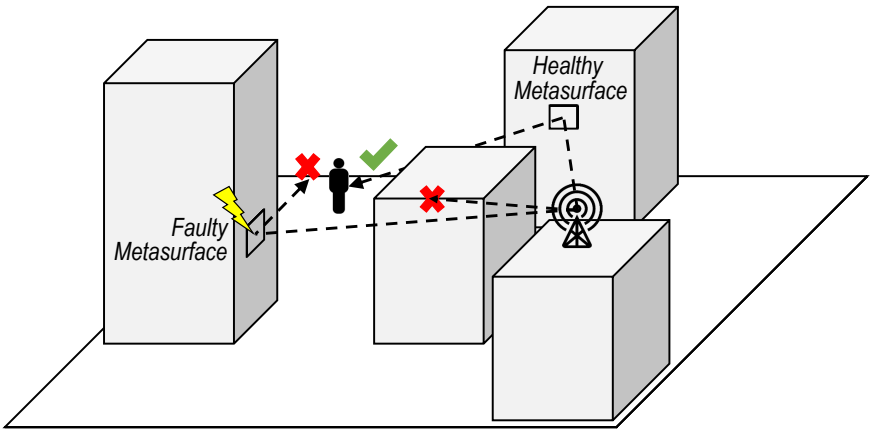

Figure 4.1: Graphical illustration of an environment augmented with potentially faulty programmable MSs. Since LoS propagation is not possible, the MSs attempt to maximize the non-LoS power at the receiver by directing the reflections and altering the phase for coherent detection. A faulty MS may lead to service disruption by not pointing the reflected beam accurately.

enabled 5G communications as shown in Fig. 4.1 [9]. To derive the error model, the causes and potential impact of faults are identified and discussed qualitatively. Here, we deepen the analysis by (i) introducing a realistic unit cell to improve the system model (Section 4.1), (ii) exemplifying the effects of failures in the components of a tunable unit cell (Section 4.2), (iii) introducing the error scenarios in the MS coding (Section 4.3) and (iv) evaluating the impact of faults in multiple performance metrics such as deviation from the target direction (Section 4.4).

4.1 Unit Cell Model

As shown in several works, providing phase reconfigurability can be achieved via several tuning mechanisms [97]. Since one of the aims of this Chapter is to capture the possible loss of performance arising from component faults, here we provide a particular unit cell design.

The case shown here revolves around the promising application of programmable MSs in millimeter-wave communications for 5G (Fig. 4.1). We assume a square unit cell ($c = 2$ mm) with a metallic backplane as shown in Figure 4.2. The unit cell is designed to resonate around 25 GHz, aimed at giving service to one of the available 5G bands according to new recommendations by the International Telecommunication Union (ITU) [98]. A square metallic patch ($b = 1.85$ mm) is stacked on top of a substrate (Rogers RO4003C) with permittivity $\epsilon_r = 3.5$ and thickness $a = 0.81$ mm. It is possible to modify the phase response of the unit cell by adding capacitance to the square metallic patch. For phase tunability,

this capacitance is given by varactors, which are embedded within the controllers and hidden under the backplane, but connected to the top patch with vertical vias [77].

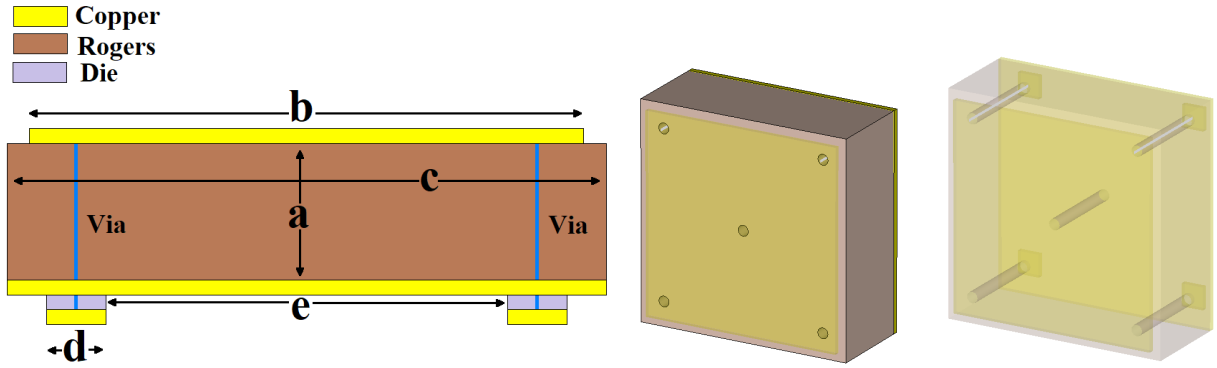

Figure 4.2: Cross-section, top-view, and bottom-view of the assumed unit cell.

We implement the proposed unit cell in a full-wave solver, CST Microwave Studio [84], and evaluate the reflection coefficient when the unit cell is illuminated by a normal incident plane wave and for a set of capacitance values.

Assuming that our design implements four coding states, it is standard practice in anomalous reflection MSs that the 2π phase range is divided into evenly spaced states with $\pi/2$ separation with high reflection amplitude [97]. As shown in Figure 4.3, the unit cell achieves these objectives around the target frequency, 25 GHz, with a reflection amplitude Γ of 0.9 and phases Φ at $\{45, 135, 225, 315\}$ degrees. The figure plots the capacitances that have achieved such separation: 0.01 pF, 0.04 pF, 0.06 pF, and 0.9 pF. We will see that, if the capacitances deviate from such values, the unit cell may inaccurately point to different amplitude and phase.

4.2 Error Model

This section presents the model that we propose for the error analysis of programmable MSs. The model describes both the impact of faults on the behavior of individual unit cells and how the faults can be distributed across the MS in Sections A and B, respectively. We also reason about the possible sources of each type of fault and attempt to exemplify a few relevant causes.

Generally speaking, faults in electronic systems may occur for a wide variety of reasons. This is also true in the mixed-signal HSF platform, where the MS and its associated tuning, control, and communication subsystems are integrated together. In any case, the relevance of different types of failure will eventually depend, among others, on the maturity of the

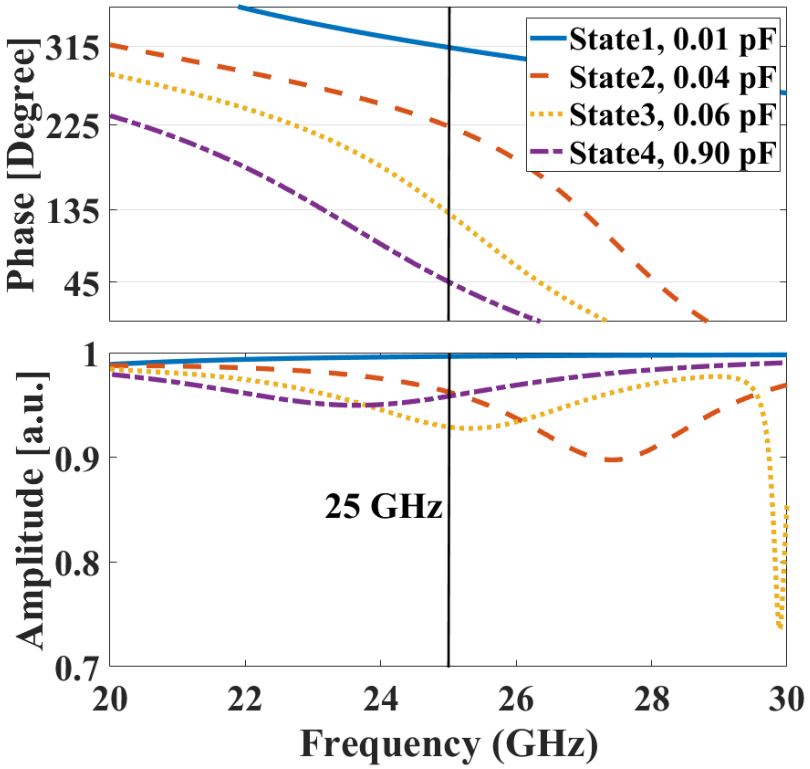

Figure 4.3: Unit cell reflection phase Φ (top) and amplitude Γ (bottom) as a function of frequency for the four chosen capacitance values.

technology, the manufacturing process, or the application environment. Several examples are outlined below. For instance, it is widely known that chip failure rates and fabrication mismatches increase as the technology nodes go down [99], which may become necessary in HSFs operating at mmWave and THz frequencies. Manufacturing defects could lead to stuck unit cells, similar to dead pixels in displays. When interconnecting the chips that drive the different unit cells, connector constraints or bad fitting can also lead to errors of different typologies. Once deployed, chip connections might fail over time due to thermal cycling or flexing. MSs could be exposed to physically challenging conditions that could lead to hard faults, such as physical damage in a conflict zone where bullets could impact the MS or bit flips due to cosmic radiation in space applications. Last but not least, ultra-low-power HSFs could power-gate a set of controllers in order to save energy in environments where a given performance degradation is tolerable. Here, the error analysis would help to determine which controllers should be powered off and at which state they should be kept. In any case, power gating can be regarded as an intentional transient fault.

A Types of Errors

Here, we describe the impact that faults can have on the performance of individual unit cells. We assume that each unit cell is assigned a *valid state* $s \in \Sigma$, where Σ represents the set with cardinality N_s of valid states for a particular unit cell design. As shown in Section 2.3, the state s basically determines the amplitude and phase of the reflection coefficient at an arbitrary unit cell.

In the presence of a fault, we assume that the unit cell will transition to a state s' which may or may not be within the set of valid states of the MS. The value of s' and its probability will depend on the type of fault, that we comprehensively classify as follows (see Figure 4.4):

- **Stuck at state:** the unit cell is stuck at a random, but valid unit cell state $s' \in \Sigma$. This type of error assumes that a failure *disconnects* the unit cell from the rest of the system, leaving it in an old state. Such a disconnection can occur due to failures in the communication or control planes (e.g. in the router or in the controller) that prevent control signals to reach the tuning element. The value of s' is picked randomly with uniform distribution.

- **Out of state:** the unit cell takes a random invalid state $s' \notin \Sigma$, which essentially means random amplitude and/or phase. Possible causes of this error may be failures that affect the tuning elements and, thus, lead to a wrong capacitance. Via disconnections arising from manufacturing defects or aging, or defects in the DAC circuits that drive the tuning element, could lead to such error.

- **Deterministic:** The unit cell stays in a known fixed, generally invalid state, which is the same across all unit cells with the same type of fault. For instance, a deterministic error could be caused by a physically damaged unit cell, i.e. a bullet making a small hole within the HSF could be approximated as zero phase and full transmittance.

- **Biased:** The unit cell is at a state which is at a fixed given distance Δ of the actual required state $s' = s + \Delta \in \Sigma$. This may be caused by flip-bit errors at the computing plane, or by external biases, perhaps due to attacks.

It is worth discriminating the mapping sequence from types of errors. In the end of Section 2.2, a process is described which maps the desired phase in the $[0, 2\pi]$ range to the closest available phase for four states s_0, s_1, s_2, s_3 (state 1 to state 4). Errors occur after the mapping done by design and, thus, may cause the unit cells states to shift to valid states (e.g. s_0, s_1, s_2, s_3; yet not the intended state for that unit cell) or invalid states (outside the phases mapped to s_0, s_1, s_2, s_3).

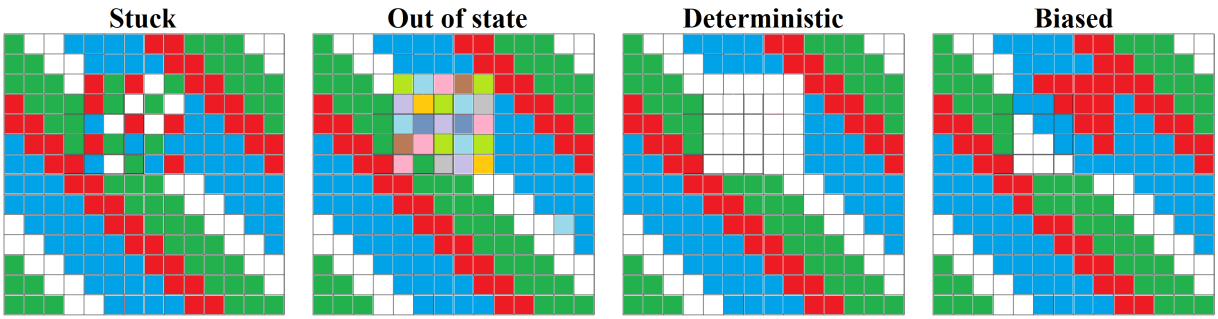

Figure 4.4: Graphical representation of the different types of error in a MS with 15×15 unit cells. White, green, red, and blue squares indicate valid states, whereas other colors indicate invalid states.

Next, we illustrate how single component faults can affect the performance of an individual unit cell. In particular, we evaluate the impact of biasing a single varactor to the wrong voltage or completely disconnecting it. To that end, we simulate the different combinations using our unit cell design from Section 4.1 as a baseline and calculate the phase error as the difference between the correct and erroneous reflection phase.

The results of this example are shown in Figure 4.5. Red bars represent the impact of via disconnection with respect to the initial states. Exponential growth from state 1 (0.01 pF) to state 4 (0.9 pF) is observed, revealing that the disconnection of large capacitances has a more significant impact. Blue, black, green and yellow bars indicate the phase error resulting from the wrong biasing of a single via from the state indicated in the X-axis to state 1, 2, 3, and 4 respectively. For instance, the first black bar indicates the phase error of biasing the via to state 2 instead of state 1. The impact of each change is subtle and does not follow a clear trend. In this particular example, then, we could approximate single via failures as an *out of state* error with a random phase.

B Spatial Distribution

Next, we describe the possible spatial distribution of errors across the MS. We base our reasoning on the fact that faults may impact multiple unit cells or have cascading effects, this is, lead to further faults. We distinguish between the following distributions, represented in Figure 4.6:

- **Independent:** The errors are randomly distributed over the MS and can be modeled with a spatial Poisson process. Individual uncorrelated faults, maybe with different origins, could yield such a distribution.

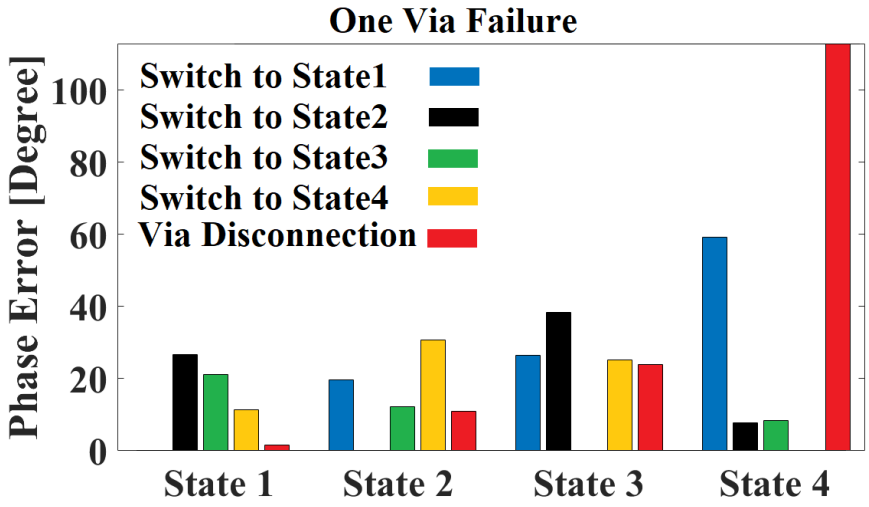

Figure 4.5: Phase error resulting from the biasing of a single via to an incorrect state, or its complete disconnection, for the proposed unit cell design at 26 GHz. The x-axis depicts the state at which the other vias are biased.

- **Clustered:** The errors appear around a given area. Cascading effects of a fault or faults that affect several unit cells can lead to such behavior. For instance, faults rendering a controller chip useless will impact all its associated unit cells. Another example would relate to the loss of connectivity at the network: faults in a few interconnects can leave an entire region of the MS isolated and stuck in an old state [80].

- **Aligned:** The errors are spatially co-located following a line. For instance, let us assume that power or ground signals are distributed through the HSF through a matrix of electrical lines. We speculate that, in such a case, if one line representing a row or column fails, the whole row and column could be affected.

- **State-specific:** Another speculative type of spatial distribution would be that all unit cells that are supposed to be in a specific state, behave incorrectly. This could happen if the actuator uses an external value (e.g. voltage from a centralized regulator) to determine the given state; if that value is incorrect, the state will be erroneous.

4.3 Introducing Errors

A general methodology for the analysis of errors in MSs would simply evaluate the metasurface in the presence of an increasing number of errors, and compare it with the performance

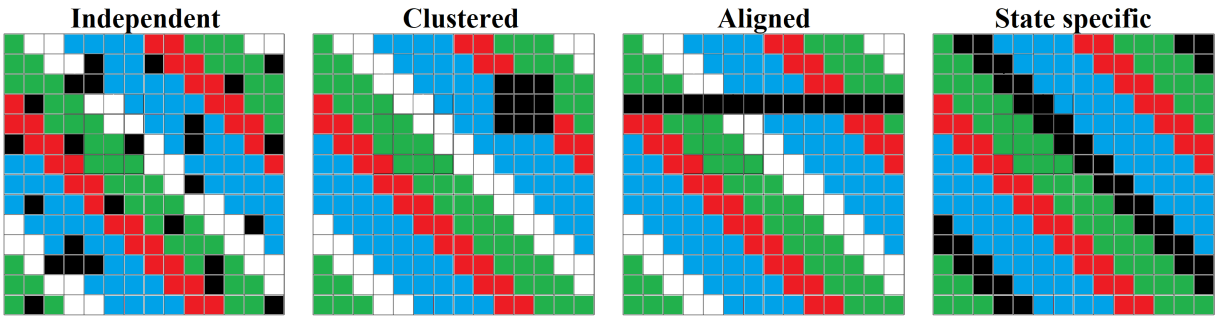

Figure 4.6: Graphical representation of the different error distributions in a MS with 15×15 unit cells. Black squares represent faulty unit cells.

of a golden reference. Basically, the golden reference is coded according to the EM functionality and evaluated using the methods exemplified in Section 2.3 for beam steering. Then, faults are introduced using the guidelines discussed in Section 4.2. To better understand the impact of errors, representative metrics are used to characterize the performance degradation as discussed in Section 2.4.

The analytical formulation allows to trivially introduce errors by modifying the terms Γ_{mn} and Φ_{mn} of the affected unit cells in Equation (2.3). The type of error, its spatial distribution, together with the percentage of faulty unit cells, define the error scenario as represented in Figure 4.7. To apply a particular error scenario, the steps are:

1. To set the number of faulty unit cells according to the input percentage.

2. To set the position of the faulty unit cells according to the spatial distribution, setting the m and n values in Γ_{mn} and Φ_{mn}, using spatial Poisson processes if required.

3. To set the Γ and Φ values of each particular unit cell, either within the discrete set of valid states Σ or within a continuous range (valid or invalid states), depending to the type of error and using random number generators if required.

4.4 Results

This section applies the proposed methodology on a particular case of beam steering MS. We take, as the basic building block, the unit cell described in Section 4.1 with the four states represented in Figure 4.3. We consider a MS of 15×15 unit cells and the far field is obtained with equations from Section 2.3. The MS is coded to point to $\theta_r = \phi_r = \pi/4$ from normal incidence, using the methods described in Section 2.2. Figure 4.8 shows

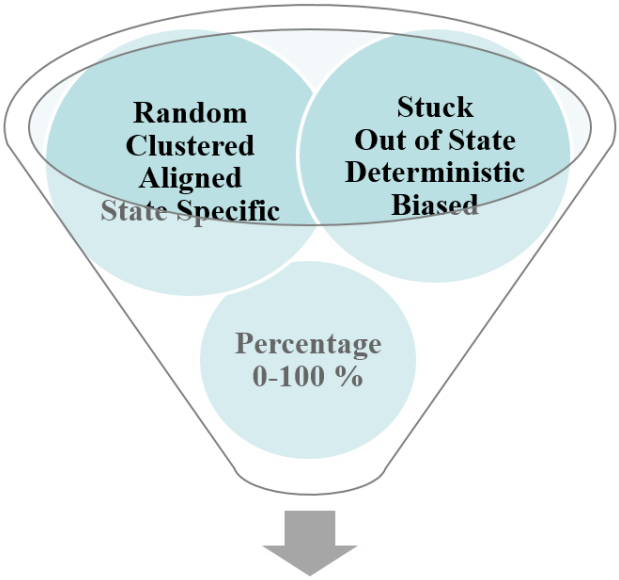

Figure 4.7: Error scenario generation process.

corresponding far-field pattern of a MS with the ideal state distribution and without any errors. Indexing the performance metrics, we get $D(\theta_r, \phi_r) = 0$ dB, $D(\theta_a, \phi_a) = 0$ dB, $TD = 1.5^o$, $HPBW = 14.47^o$, $SLL = -11.43$ dB and $SLA = 11.14$ dB. Note that the directivity values are normalized to the strength at the direction of maximum radiation, which is why we obtain a value of 0 dB.

A Overview

Figure 4.9 demonstrates how different types of error and their spatial distribution can have a significantly different impact. The far field is plotted for increasing fault rates for four representative combinations of error type and spatial distributions. It is observed that the MS points most of the energy towards the intended direction of $\theta_r = \phi_r = \pi/4$ for relatively low error percentages and starts losing its functionality as the percentage increases.

The differences between the distinct types of errors are clearly distinguishable. For instance, Figure 4.9a shows the far field for the MS with stuck-at errors clustered around the center. We can see that increasing the error ratio gives more power to the side lobes and decreases the width of the main lobe. The clustered-biased scenario shown in Figure 4.9b, on the other hand, illustrates that biasing errors are less impactful because, in the end, the phase gradient is largely conserved. Similar studies performed for the (independent, out of state) and (independent, deterministic) scenarios, shown in Figures 4.9c and 4.9d, respec-

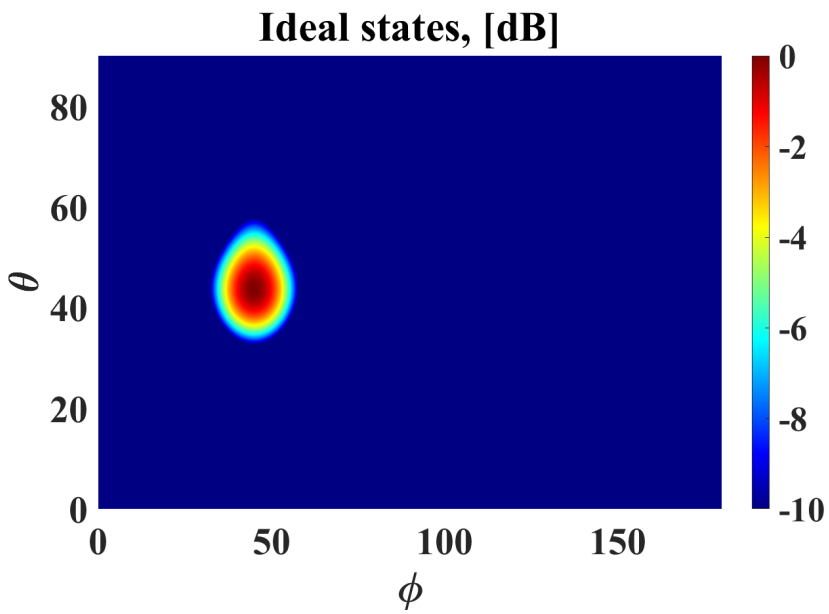

Figure 4.8: Normalized radiation pattern of the ideal distribution of the states in a MS with 15×15 unit cells.

tively, allow to conclude that completely random errors tend to average out and minimize impact, whereas deterministic errors tend to destroy the functionality by increasing the importance of specular reflection, which becomes the main lobe for more than 30% of error ratio.

Here we set the deterministic error to be s_0, which ends up with a strong secondary lobe at $\theta = 0$ and arbitrary ϕ. This reflection angle is independent of the determined value of the error and we would obtain the same results with any other determined value (s_1, s_2, s_3). This reflection, namely specular, is only characterized by the incident angle. In other words, deterministic errors react as a mirror reflecting the incident wave according to Snell's law ($\theta_i = \theta_r$ and $\phi_i = \phi_r$) irrespective to the erroneous value, as long as it is the same in all erroneous unit cells. In our case (normal incident of plane wave), where we put $\theta_i = 0$ and arbitrary ϕ_i, we obtain $\theta_r = 0$ and arbitrary $\theta_r = 0$.

The next sections complement this qualitative analysis with the evaluation of performance metrics for different combinations of type of error and spatial distribution. For the sake of brevity, we consider the combinations outlined in Table 4.1. The rest of the possible combinations have been evaluated, but are not shown due to their behavioral similarity with the combinations from Table 4.1.

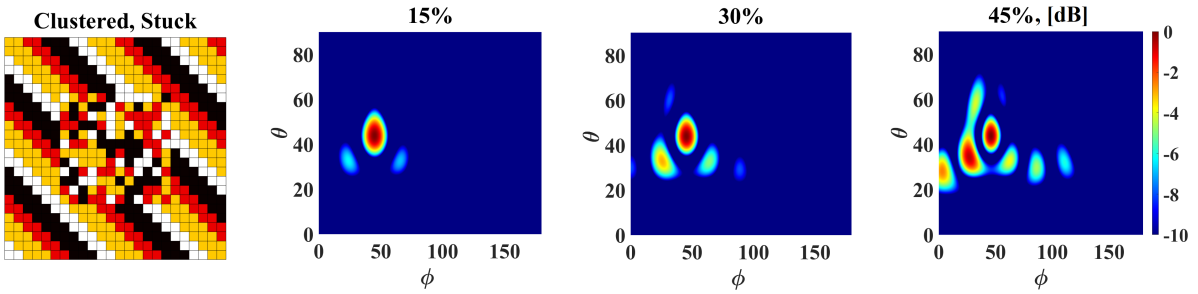

(a) Sketch of the MS coding under Clustered-Stuck errors and radiation pattern for three error percentages.

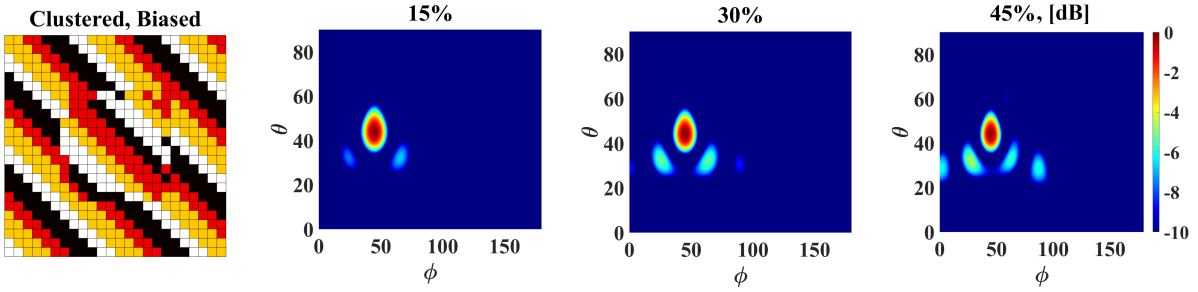

(b) Sketch of the MS coding under Clustered-Biased errors and radiation pattern for three error percentages.

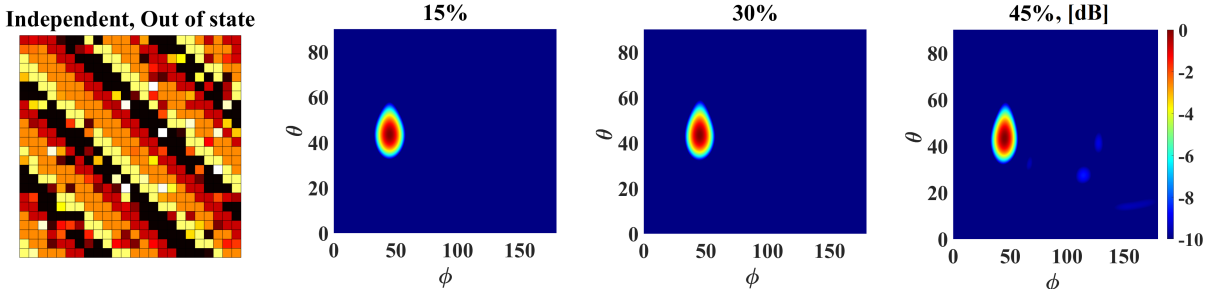

(c) Sketch of the MS coding under Independent-Out of state errors and radiation pattern for three error percentages.

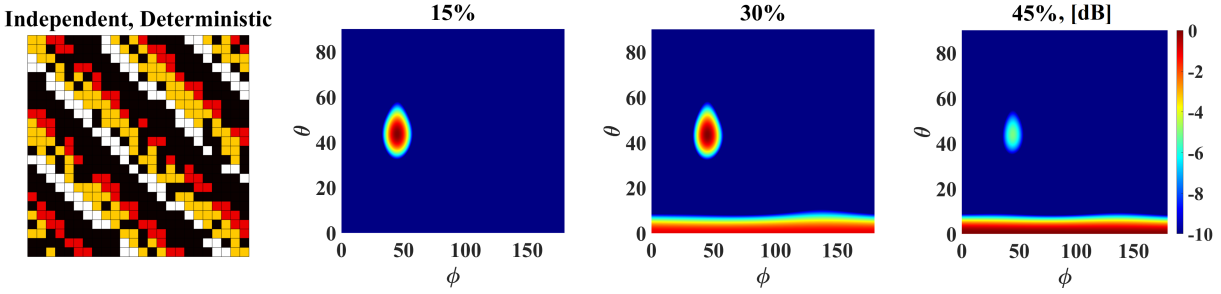

(d) Sketch of the MS coding under Independent-Deterministic errors and radiation pattern for three error percentages.

Figure 4.9: Qualitative analysis of performance degradation for different error scenarios.

Table 4.1: Error scenario acronyms.

Error scenario	Acronym
Clustered-Stuck	CS
Clustered-Out of State	CO
Clustered-Deterministic	CD
Clustered-Biased	CB
Independent-Stuck	IS
Independent-Out of State	IO
Independent-Deterministic	ID
Independent-Biased	IB

B Directivity

Figure 4.10 illustrates the impact of the different types of errors by plotting the Directivity at the desired reflection angle $D(\theta_r, \phi_r)$ over the error percentage. As expected, the most detrimental type of error is deterministic because all wrong values are mapped to the same phase, which has a more detrimental effect in the beam steering case due to its phase-gradient requirements. This reasoning also implies that different types of errors may have a completely different impact on MSs implementing different functionalities: for instance, absorbers may set the same value to all unit cells and, therefore, deterministic errors may not reduce performance vitally. Assuming a 3 dB threshold as the acceptable performance degradation, we observe that CD is the most degrading option as error rates beyond 20% cannot be tolerated, while Out of state and Biased errors (IO, IB, CO and CB) guarantee good performance beyond 40% of erroneous cells.

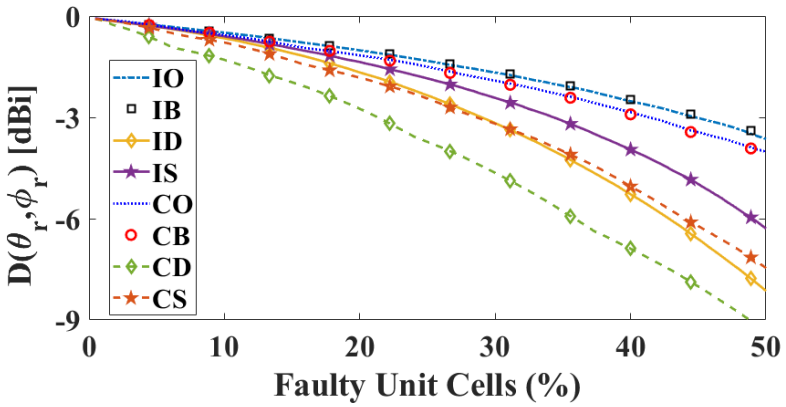

Figure 4.10: Directivity on target direction $D(\theta_r, \phi_r)$ of the beam steering MS as a function of the error percentage for different error types and spatial distribution.

The story is different for the directivity at the direction of maximum radiation, $D(\theta_a, \phi_a)$, as shown in Figure 4.11. In this case, the curves of $D(\theta_a, \phi_a)$ corresponding to deterministic errors with fault rates beyond 33% start to increase regardless of their spatial distribution. The reason for this behavior underlies behind the fact that deterministic errors posses the same reflection phase and, by the accumulation of many of these errors, a secondary beam starts to grow. The 33% error figure represents the inflection point where the secondary lobe becomes the main lobe. This is illustrated in Figure 4.12 for the independent-deterministic combination of errors, revealing how the secondary lobe emerges at $\theta = 0$ and becomes the main beam.

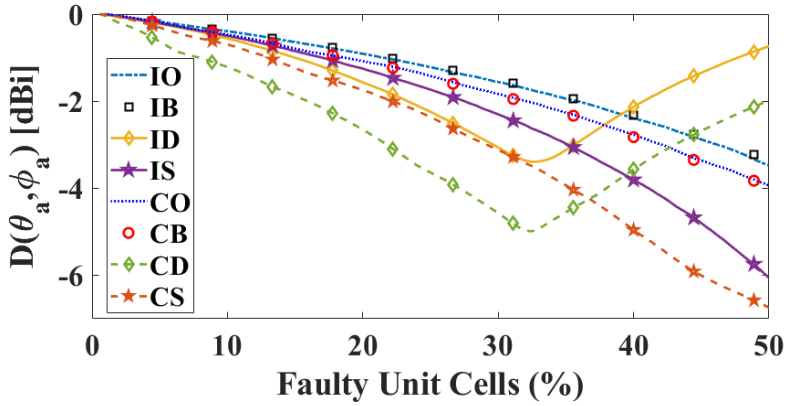

Figure 4.11: Directivity on the direction of maximum reflection $D(\theta_a, \phi_a)$ of the beam steering MS as a function of the error percentage for different error types and spatial distribution.

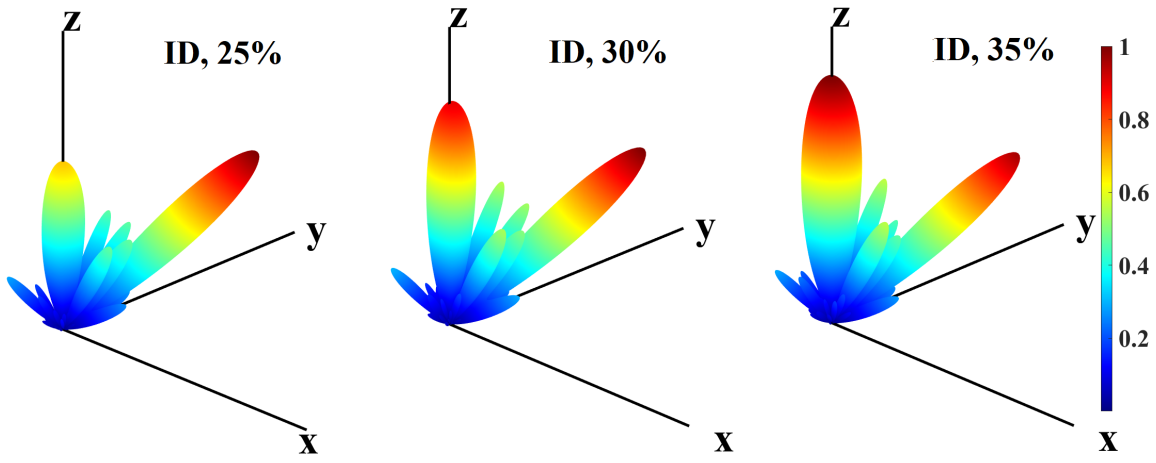

Figure 4.12: The normalized radiation pattern for ID errors as an example of an emerging secondary lobe in the wrong direction. The color bar is common to all figures.

C Target Deviation

In this part, we want to emphasize the importance of the differences between the desired and actual position of the main beam. Figure 4.13 shows the accuracy of the beam steering MS versus different error scenarios. As mentioned above, deterministic errors may make the main beam shift from the target direction to specular reflection. This is the main cause of the jump observed at 33% for TD. Beside CS that forces the main beam to deviate, other kinds of errors are not affecting TD considerably. In fact, TD takes values below 2 degrees, which is acceptable for most applications. This suggests that loss of directivity or increase of side lobe may be more critical in the present scenario.

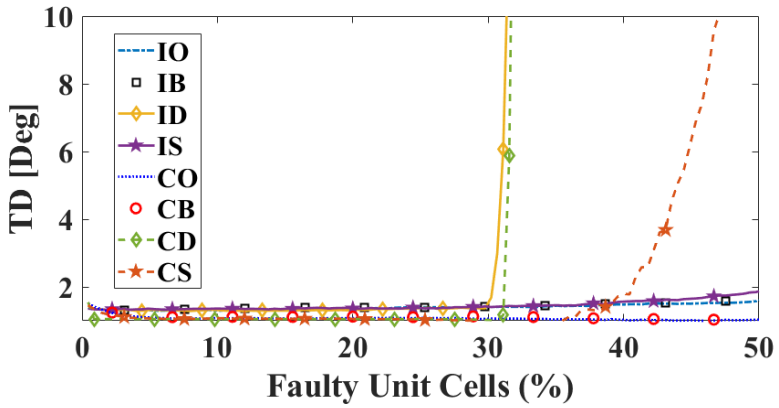

Figure 4.13: Deviation from the target versus the percentage of the faulty unit cells for different error types and spatial distribution.

D Half Power Beam Width

From Figure 4.14 it can be inferred that, on one hand, the $HPBW$ is not affected by the IS, IO and IB combinations of errors. However, their associated types with cluster distributions, CS, CO, and CB smoothly decrease the $HPBW$. We can relate this effect to the consolidated spot of errors leading to a united constructive response. On the other hand, for Deterministic cases (i.e., ID and CD), a jump at 33% is observed due to the deterministic values of errors. At this turning point, anomalous reflection (i.e. the desired behaviour) is very weak, while specular reflection (emerged from deterministic errors) is strong enough to take over as the main beam. This is the reason for the jumps for $HPBW$ in Figure 4.14. In other words, before 33% we have the $HPBW$ of anomalous reflection and after that of specular reflection.

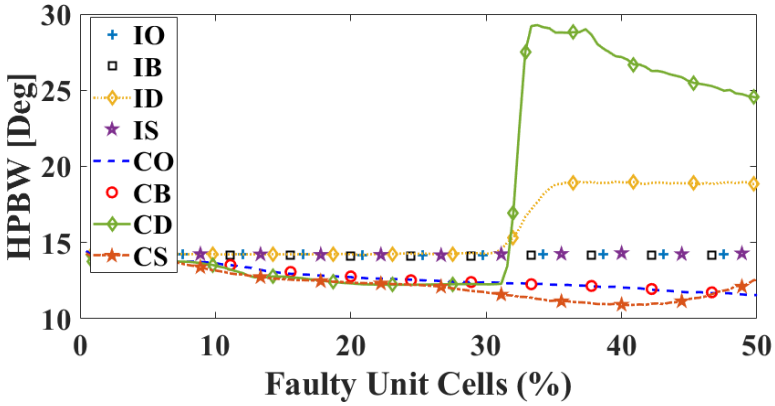

Figure 4.14: Half power beam width versus the percentage of the faulty unit cells for different error types and spatial distribution.

E Side-Lobe Level

Figure 4.15 illustrates the performance degradation in terms of side lobe level. It is quickly observed that SLL is the most sensitive performance metric so far. Fundamentally, SLL grows proportionally to the ratio of errors for all kinds. Among the monotonically increasing cases, clustered distributions seem to have a higher impact in this metric, whereas independent and out of state errors are the least relevant. Since random coding [58] leads to random scattering, we argue that uncorrelated random errors generate scattering that does not accumulate as a large secondary lobe. On the other hand, clustered and deterministic errors, which tend to group unit cells together and to apply a uniform state, lead to large secondary lobes.

Deterministic errors lead to a characteristic behaviour that we elucidated with several simulations at specific points for CD and ID. The dip appearing between 29% and 37% is due to the fact that a secondary lobe starts to disappear while another minor lobe begins to rise. At 32%, this minor lobe takes the place of secondary lobe then at 37% main and secondary beams are exchanging their roles and SLL starts to decline once again.

F Side-Lobe Accumulated Energy

SLL cannot accurately describe the distribution of energy around the main lobe, so we evaluate the SLA metric in Figure 4.16 to consider the impact of all the minor lobes. This figure demonstrates that, as expected, increasing fault rates reduce the power at the main beam and distribute it around a set of side-lobes. The main lobe is debilitated very similarly for all error combinations. Likewise, deterministic errors exhibit abnormal behaviour for SLA showing a dip between $[29\% - 32\%]$ and decline after 37%. The reason being of such

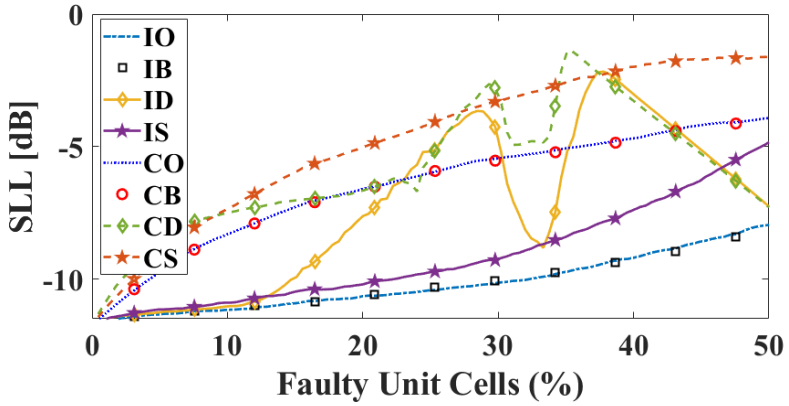

Figure 4.15: Secondary lobe level versus the percentage of the faulty unit cells for different error types and spatial distribution.

trend is similar to that discussed in Section E.

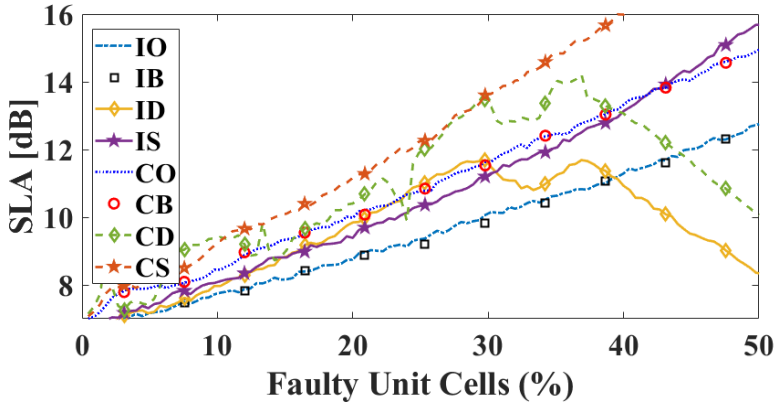

Figure 4.16: Accumulated energy of the side lobes versus percentage of the faulty unit cells for different error types and spatial distribution.

4.5 Summary

In this chapter, we have used a general methodology for the error analysis of programmable MSs, where faults are distinguished by their impact on individual unit cells and their spatial distribution across the MS. Albeit applicable to any functionality, the methodology has been used to study a beam-steering MS at 26 GHz for 5G applications. This case is particularly robust against spatially uncorrelated errors with random values, since these generate mild scattering that does not form detrimental side lobes. For the MS under evaluation, the functionality is preserved with minor degradation even if faults affect 1/4 of the unit cells. On the contrary, clustered errors that set all the unit cells to the same state are very detrimental as they favor the formation of powerful side lobes. Overall, these results illustrate the value

of the error analysis to guide the design of future programmable MSs by, for instance, demonstrating that 25% of the controller chips could be powered off without reducing the beam steering performance significantly.

Chapter 5

Multi-User Communication Empowered with Metasurfaces

The transition from static to intelligent programmable MSs costs design, fabrication, and embedding complexity. RISs need to integrate tuning and control elements on a per-cell basis, electronic circuits to implement intelligence within the device, as well as mechanisms to interface the surface with the world. Such complexity may lead to uneconomical design and fabrication process which is an obstacle toward commercializing the applications within 5G networks. One way to justify the costs is to make full use of the technology and explore ways in which the exploitation is maximized. MSs can actually perform multiple functions concurrently [100], so one design can serve several purposes. Preferentially, in the use case of wireless communications, multi-user scenarios are appreciated. In this case, an MS provides services for multiple users which is a very compelling.

An omnidirectional antenna can communicate with multiple users through a wide beam. In this case, the beam is detrimental as it squanders the energy in a huge space. This strategy is not practical for mmWave spectrum because high propagation losses [101] combined with the challenge of high power transmitters [102], severely restricts the communication range. The proper solution is to engineer the radiation pattern with respect to the users' location. In order to engineer a radiation pattern with independent control over the beams, MSs space or time allocation should be shared between the users. Space or time multiplexing is a linear segmentation of the MSs in space or time domain. However, the distribution of resources between the users diminishes the link quality compared to single user communication. Multi-user scenarios rely on the proper execution of multiplexing by which the space-time allocation is optimized.

In this chapter, we introduce a technique based on the momentum conservation law and

superposition of waves for MS reconfiguration to engineer multiple beams independently. Based on the realistic system parameters, we then evaluate the performance of the proposed framework by analyzing the throughput in indoor, outdoor and broadcast scenarios. We compare our results to the baseline system, and show that by taking advantage of the MS, orders-of-magnitude improvements in the overall system throughput can be experienced.

With this background, we now highlight the organization of the chapter as follows: In Section 5.1, we review the latest works in multi-user communications. Section 5.2 describes proposed technique to reconfigure the MS for multi-user communication. Section 5.3 describes the indoor, outdoor and broadcast scenarios on which we evaluate our system. In Section 5.4 the system model is introduced. Section 5.5 presents the performance evaluation and Section 5.6 summarizes the chapter.

5.1 Background

Time-Division Multiplexing (TDM) handovers the communication link between multiple users in separate time slots [103]. Time is divided into several recurrent blocks of fixed length, one for each user. In terms of MS, TDM refers to time domain reconfiguration which provides a shared communication link that switches between users. In theory, this technique can provide adaptive multi-channel communication by space-time shared aperture [104] with great performance. However, this is not a trivial mechanism, and realizing a TDM MS comes with a major challenge. In 5G, end-to-end latencies as low as 1 ms need to be met with reliability as high as 99.99% [105]. Tracking a moving user requires reconfiguration of the MS to sustain the communication link and the reconfiguration speed affects the latency. This might not be a serious problem in single user scenarios but in the multi-user case, the reconfiguration cycle is multiplied by the number of users. A TDM MS switches the link between the user in the time domain and reconfiguration speed of the MS will have to be extremely fast to rearrange the link with an acceptable delay. The reconfiguration delay is the time takes to reprogram the MS to serve the specific user group (see Fig 5.1).

$$SL = N \times (UGD + R) \tag{5.1}$$

where SL is the length of the subframe, UGD is the user group delay, N is the number of users and R is the reconfiguration delay. As an example, consider that the maximum length of a single subframe for the 5G New Radio (NR) is 1 ms [106]. Further, let us assume that we have $N = 10$ groups of users, wherein each group, a user is served in a given subframe. Hence, it is essential that the MS reconfiguration is completed in a time that is on the scale of a few microseconds, which is a real challenge.

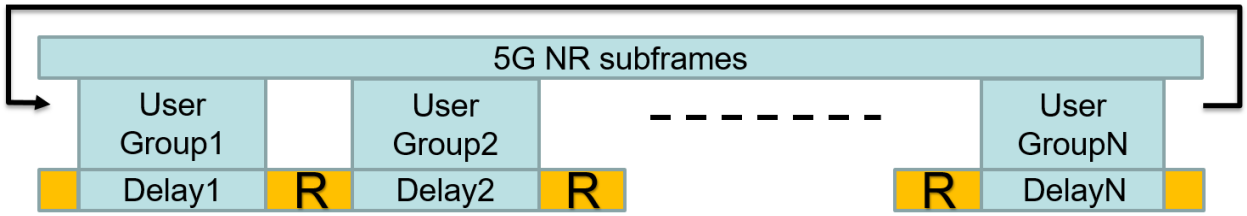

Figure 5.1: Time allocation of each user group (collection of users) in a subframe alongside the reconfiguration duration shown in yellow.

A better strategy to meet 5G criteria is to communicate with all the users concurrently. So, instead of multiplexing in time domain, we suggest to partition the area of the MS and assign a specific segment per user. This segmentation process is equivalent to dividing the original MS into a collection of smaller MS, which inevitably follows with lowering the *Directivity*. Henceforth, enlarging the MS is essential to maintain the Quality of Service (QoS) for multi-user scenarios. While it is possible to estimate the optimal size of the MS depending on the number of users and the desired QoS, the question *"how to divide the MS area amongst users?"* still remains. Figure 5.2 illustrates that the allocation of the MS area amongst two users affects the radiation pattern. While optimization methods can help us determine the best segmentation, they require extensive computing power and time, which is unrealistic. For instance, a single simulation of a MS in CST Microwave Studio [84] takes around one hour. Since, the number of possibilities of MS segmentation is huge, finding the optimized reconfiguration is almost impossible. To exemplify the numbers, consider a grid of 24×24. Next, as suggested in [107], we set $N_s = 4$ states to code (i.e., setting specific phase and amplitude profiles) the MS. Consequently, the overall possibilities will be $4^{24\times24}$. Henceforth, determining an optimal solution becomes extremely unrealistic for real-world deployments.

Moreover, there have been multiple works such as [108, 109], wherein an optimization approach has been provisioned to enable multi-user communication with the RIS. While these works aim at determining the most optimal transmit power, phase shift combination at the RIS/MS, size of RIS/MS, etc., to facilitate multi-user communication, they do not consider the practical aspects of such a programmable MS. Concretely, the MS is considered to be capable at all times to switch its characteristics instantaneously, which as mentioned above is not trivial. Furthermore, computing a global solution is time and power-intensive, hence not viable in real network environments.

Thus, in the following sections, we propose a simple and fast methodology to reconfigure the MS for multi-user communications. Additionally, through an overall system throughput performance analysis, we elaborate on the capability of our method to support multi-user

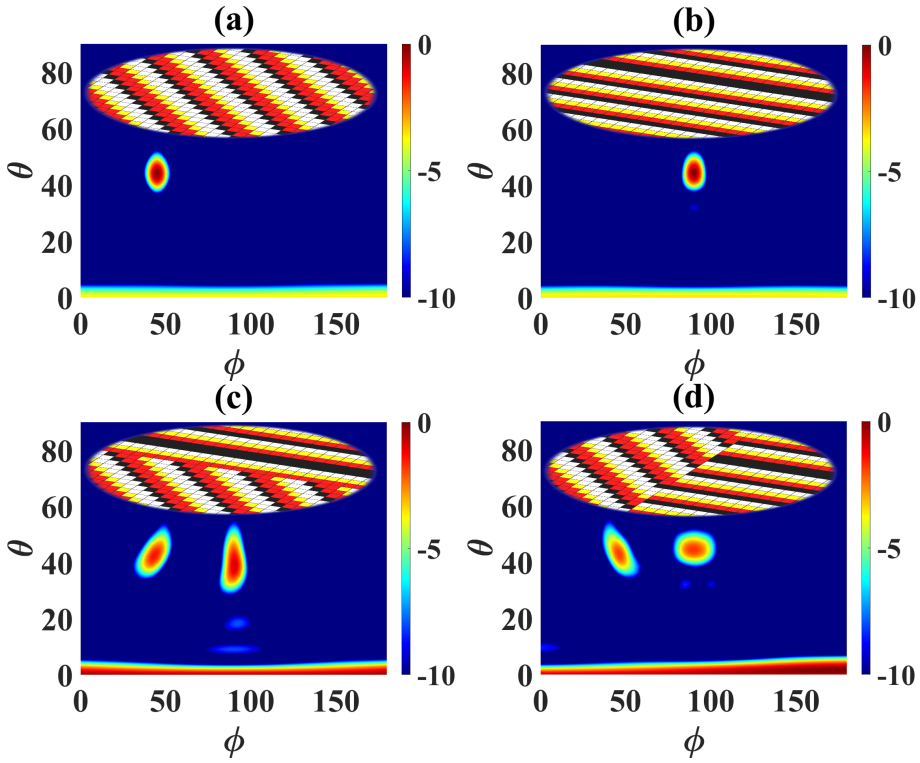

Figure 5.2: Normalized E-field distribution in logarithmic scale (dB) targeting users at (a) $\theta_r = \phi_r = \pi/4$ and (b) $\theta_r = \pi/4, \phi_r = \pi/2$ as single-user MSs compared with two-user MSs dividing the area Row-wise (c) and Column-wise (d) to target both users

communications in indoor, outdoor, and broadcast transmission scenarios.

5.2 Metasurface coding for anomalous reflection in multiple directions

In Chapter 2, we mention that programmable MSs can be reconfigured for different RA. The main lobe of the radiation pattern should track the movement of the user. In other words, instead of the natural (i.e., specular) reflection, MS manipulates the reflection wavefront towards the user position. Using phase gradient described in Equation (2.2), we can encode the MS to reflect the beam toward any arbitrary reflection angle (θ_r, ϕ_r).

Nevertheless, in multi-user case where we have several pairs of reflection angles (i.e., (θ_{r1}, ϕ_{r1}), (θ_{r2}, ϕ_{r2}), ... (θ_{rK}, ϕ_{rK})) former coding is not helpful anymore. However, we solved this issue with fundamental rules. According to the users' position, one can calculate the relative phase profiles individually. The phase is a periodic variable and phase value ranges from 0 to 2π. Thereby, based on the principle of superposition of waves, we can

encapsulate the individual phase profiles by adding them. Assuming normal incident and the amplitude of reflection as unity Equation 2.3 reads

$$E(\theta,\phi)=\sum_{n=1}^{N}\sum_{m=1}^{M}\cos(\theta)e^{jk_0\zeta_{mn}(\theta,\varphi)}(e^{j\Phi_{mn}(\theta_{r1},\phi_{r1})}+e^{j\Phi_{mn}(\theta_{r2},\phi_{r2})}+...+e^{j\Phi_{mn}(\theta_{rK},\phi_{rK})}) \quad (5.2)$$

where $\Phi(\theta_{r1},\phi_{r1})$, $\Phi(\theta_{r2},\phi_{r2})$, and $\Phi(\theta_{rK},\phi_{rK})$ are the phase gradient for the first, second, and Kth-user respectively. The result of this summation is a term with both phase profile Φ_{mn} and amplitude profile Γ_{mn}.

$$\sum_{k=1}^{K}e^{j\Phi_{mn}(\theta_{rk},\phi_{rk})}=\Gamma_{mn}e^{j\Psi_{mn}} \quad (5.3)$$

This means, we can engineer a multi-beam radiation pattern by controlling simultaneous amplitude/phase profile of the unit cells. Nevertheless, any reflection amplitude other than unity means loss. Here, we propose a solution to discard the need for amplitude engineering. By considering the conservation law of energy, in a closed system, all the energy from the impinging wave should be divided between the unit cells. So, in a lossless situation, all the power will be scattered from the MS. Since unity reflection of the subclass profiles are not important anymore, one can change the unity coefficients in subclass profiles to conserve the unity reflection of the overall term as

$$\frac{1}{\Gamma_{mn}}\sum_{k=1}^{K}e^{j\Phi_{mn}(\theta_{rk},\phi_{rk})}=e^{j\Psi_{mn}} \quad (5.4)$$

Then, Equation (5.2) reads

$$E(\theta,\phi)=\sum_{n=1}^{N}\sum_{m=1}^{M}\cos(\theta)e^{jk_0\zeta_{mn}}\frac{1}{\Gamma_{mn}}\sum_{k=1}^{K}e^{j\Phi_{mn}(\theta_{rk},\phi_{rk})} \quad (5.5)$$

Now that we have the final phase gradient without any amplitude profile, the next step is to encode the unit cells. We simulated the MS in CST Microwave Studios. Phase gradient is realized by encoding the relative permittivity ϵ_r to provide the desired phase reflection. Any other unit cell designs [2,38] would operate in the same way. By selecting $D_u=\lambda/3$, we can ensure that the phase gradient is mapped on the MS with acceptable resolution [107]. Figure 5.3 (a,b), shows the radiation pattern and relative phase gradient of a square MS with size of $D_m=8\lambda$. The obtained radiation pattern is improved compared to spatial subdivision technique (Figure 5.2 (c,d)). By setting another phase gradient for the next user, we can extend the methodology for any number of users. Figure 5.3 represents 3 lobes targeting 3 users and respective phase gradient on the MS.

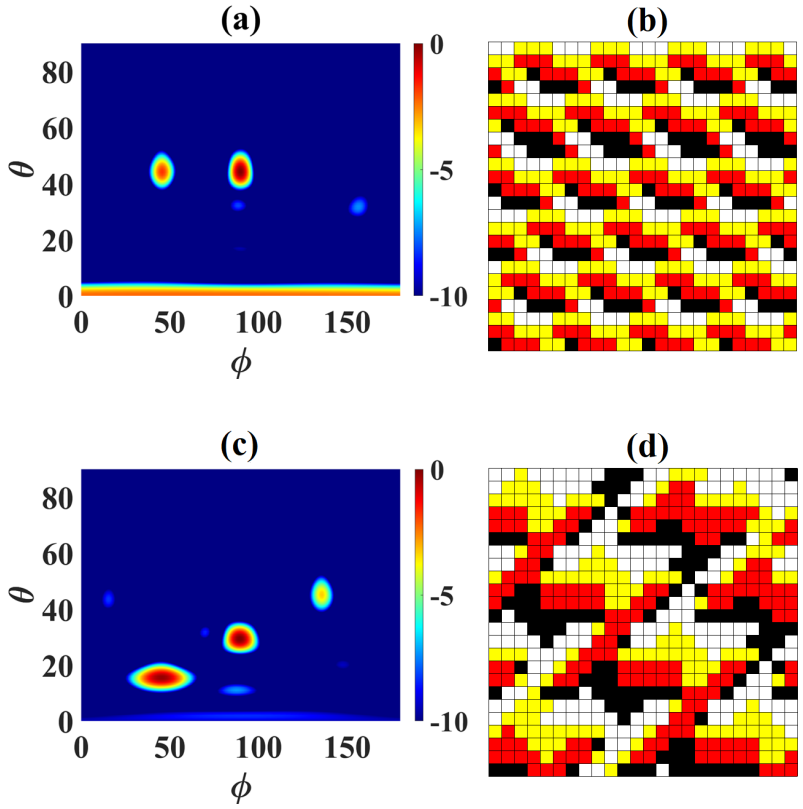

Figure 5.3: Normalized E-field distribution in logarithmic scale (dB) targeting users at $\theta_r = \phi_r = \pi/4$ and $\theta_r = \pi/4, \phi_r = \pi/2$ (a) and respective phase gradient (b). Normalized E-field distribution in logarithmic scale (dB) targeting users at $\theta_r = \pi/12, \phi_r = \pi/4$, $\theta_r = \pi/6, \phi_r = \pi/2$ and $\theta_r = \pi/4, \phi_r = 3\pi/4$ (c) and respective phase gradient (d).

Since the dimension of the MS is fixed at $D_m = 8\lambda$, engineering more beams decreases the *Directivity*. This issue gets critical when we have even more users. The simplest solution is to develop a larger MS. However, due to the design and manufacturing costs, it is preferred to keep the size of the MS as small as possible. To provide complex radiation patterns with more beams for multi-user communications, we need to impose the phase gradient with higher resolution. One way is using smaller unit cells which will increase the complexity of the system. A better policy is to improve the mapping by increasing the number of states (N_s). We checked the influence of N_s in case of 4-users in Figure 5.4 such that (b) shows the phase gradient with 4 different colors representing $N_s = 4$, (d) shows the phase gradient with 8 different colors representing $N_s = 8$ and (a,c) are the respective radiation patterns. Apparently, in the bottom sub-figure (c) the specular reflection at the normal direction ($\theta = 0$) is 5 dB weaker than top sub-figure (a) which will improve the efficiency of the system and decreases the backscattering toward the source.

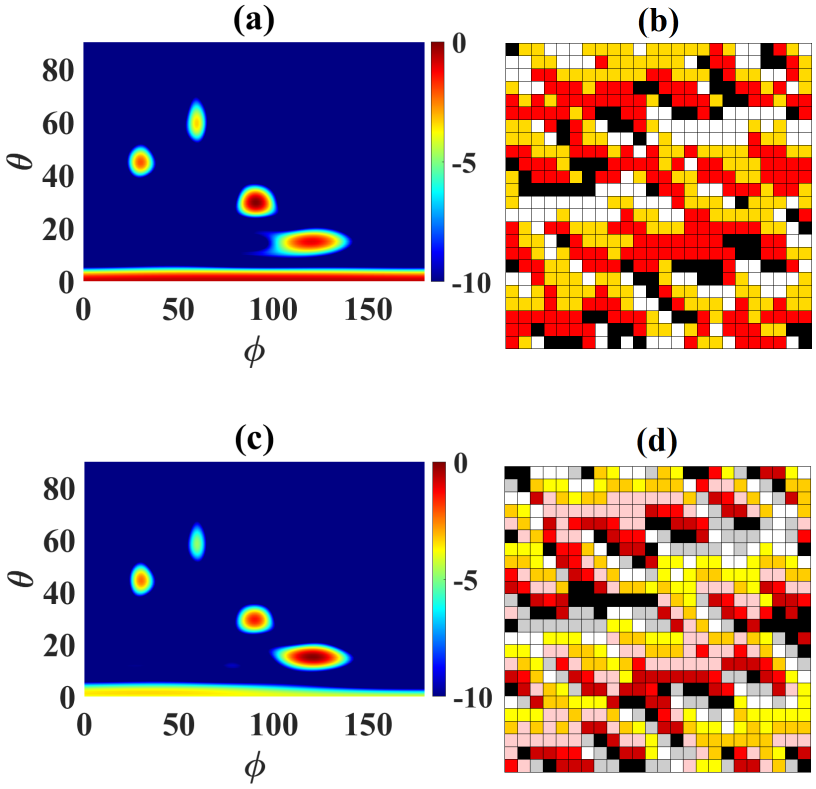

Figure 5.4: Normalized E-field distribution in logarithmic scale (dB) targeting 4-users at random locations with 4 and 8 states (a,c) and respective phase gradient with 4 and 8 states (b,d).

5.3 Scenarios

To illustrate the efficacy of our MS coding, we analyze its performance in the standard indoor and outdoor environments, as defined by Third Generation Partnership Project (3GPP) [110], and compare it with the current wireless network scenarios. Note that, while multiple research efforts, such as [108, 109, 111–114], do not consider realistic MS operational characteristics such as the *Directivity*, in this chapter we perform the very first analysis by utilizing practical MS performance parameters. These parameters have been determined using the methodology described in Section 5.2.

A Indoor Office Environment

The scenario corresponding to indoor office environments is presented in Fig. 5.5. Characteristically, in such scenarios, the Base Station (BS) is a low power transmitter, such as those for WiFi, etc, as compared to the cellular Access Point (AP). Moreover, the trans-

mission path to the receivers can be blocked completely by obstacles such as walls, etc. Additionally, due to the density of obstacles, the propagation environment will be significantly impacted by multipath issues. The aforesaid impairments are further exacerbated for mmWave frequencies [115–118].

Hence, in Fig. 5.5, the User Equipment (UE) has the direct LoS path from an AP blocked by an obstacle. The AP to MS link has a LoS alongside Rician fading [1]. In addition, the MS to UE link has a directed beam. We point out that, it is the MS which provides a bridge (LoS path) to the AP towards the UE, thus circumventing the complete blockage by the obstacle in between.

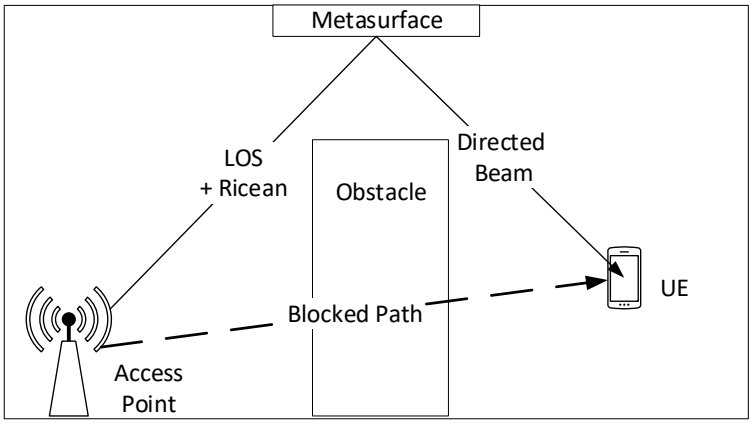

Figure 5.5: Indoor office environment propagation scenario

B Urban Micro Environment

The UMi environment, as shown in Fig. 5.6, consists of multiple BSs, i.e., the Marco Cell Base Station (MCBS) as well as the Small Cell Base Station (SCBS), serving the users. In 5G and beyond scenarios, the SCBSs will be deployed to enhance the throughput, and hence, they will mostly operate upon the mmW frequencies [117, 118]. On the other hand, MCBSs, or the anchor cells, will provide a more reliable connection to the users, thus maintaining coverage as well as supporting various dynamic scenarios [119, 120].

Consequently, while the SCBS will be blocked by the myriad obstacles present in a dense urban environment, such as that shown in Fig. 5.6, MCBSs will still have Non-LoS path

[1]For Line of sight scenarios, Rice model is widely adopted as the small scale fading model. For Non-LoS scenarios, a Rayleigh model is adopted for small scale fading. Note that, other complex and more specific models exist, however we choose the aforesaid rice and Rayleigh fading models for their simplicity.

towards the users. Such a channel is accompanied with a Rayleigh fading model for the small scale fading. Additionally, the SCBS has a LoS path through the MS to the users, similar to the indoor environment in Section B.

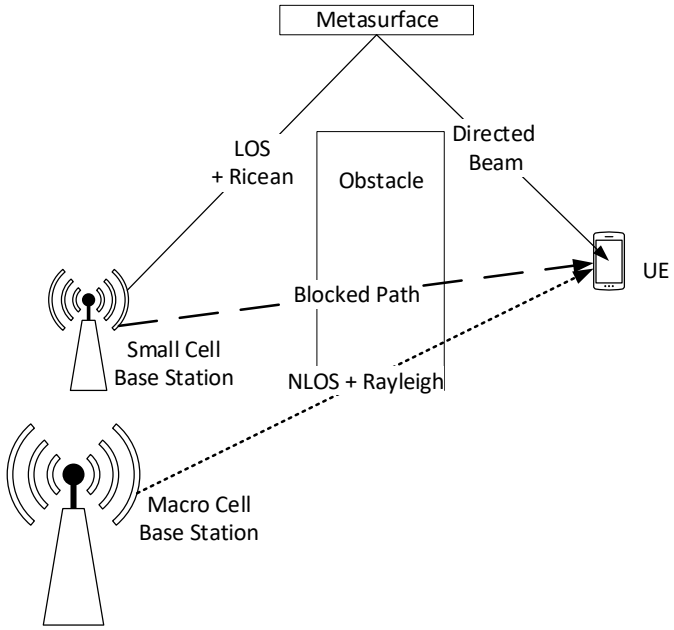

Figure 5.6: UMi environment propagation scenario

C Broadcast

As part of the analysis, in this work, for both the indoor and UMi scenarios, the broadcast mode of communications is evaluated. The broadcast (as well as multicast) mode enables the network to communicate the same information to multiple users at the same time. An important example for such applications os the video streaming service.

5.4 System Model

Given the scenarios, we now discuss the system model for our evaluation. Firstly, we state that for both the indoor office environment and UMi scenarios, the BS and SCBS, respectively, communicate with the UE through a LoS path facilitated by the MS. Hence, the channel model for the aforesaid data path is represented as:

$$y_{sc} = (\mathbf{g}_{\mathbf{MU}}^{\mathbf{T}} \boldsymbol{\Theta} \mathbf{h}_{\mathbf{BM}}) x_{sc} + \eta_{sc} \tag{5.6}$$

where y_{sc} and x_{sc} are the received and transmitted signals, respectively, and η_{sc} denotes the additive white gaussian noise with zero mean and variance (average noise power) σ_{sc}^2 . Furthermore, $\mathbf{h_{BM}}$ and $\mathbf{g_{MU}}$ are the BS to MS and MS to UE channel coefficient vectors. Additionally, $\mathbf{\Theta}$ is the phase applied by the MS on the received signal from the BS [2]. Additionally, the channel model for the MCBS to UE path in the UMi scenario (see Section B) is defined as:

$$y_{mc} = h_{mc}x_{mc} + \eta_{mc} \tag{5.7}$$

where y_{mc} and x_{mc} are the received signal at UE from MCBS and transmitted signal from MCBS to UE, respectively. The channel coefficients for the MCBS to UE channel is represented by h_{mc}, with the additive white Gaussian noise represented as η_{mc} which has zero mean and variance (average noise power) σ_{mc}^2. From Equations (5.6) and (5.7), the overall received Signal to Noise Ratio (SNR) at UE for the indoor scenario is determined as:

$$\Delta_{InH} = \frac{||y_{sc}||^2}{\sigma_{sc}^2} \tag{5.8}$$

whereas the received SNR at the UE for the UMi scenario is expressed as:

$$\Delta_{UMi} = \begin{cases} \frac{||y_{sc}||^2}{\sigma_{sc}^2} & \text{SNR at UE from SCBS,} \\ \frac{||y_{mc}||^2}{\sigma_{mc}^2} & \text{SNR at UE from MCBS} \end{cases} \tag{5.9}$$

Next, the maximum achievable throughput for the users in both the indoor and UMi scenarios can be defined by the Shannon-Hartley theorem as follows:

$$R = B\log_2(1 + SNR) \tag{5.10}$$

where, R is the maximum achievable throughput for a user, B is the allocated bandwidth by a base station (BS/SCBS/MCBS), and SNR is the Signal-to-noise ratio at the receiver from a given base station. Hence, from Equations (5.8), (5.9) and (5.10), the maximum throughput for a user in the Indoor environment, i.e., R_{inh}, is given as:

$$R_{inh} = B_{inh}\log_2(1 + \frac{||y_{sc}||^2}{\sigma_{sc}^2}) \tag{5.11}$$

where B_{inh} is the bandwidth allocated to the user by the BS. On the other hand, the maximum achievable throughput for the UMi scenario, as shown in Fig. 5.6, is:

$$R_{UMi} = B_{sc}\log_2(1 + \frac{||y_{sc}||^2}{\sigma_{sc}^2}) + B_{mc}\log_2(1 + \frac{||y_{mc}||^2}{\sigma_{mc}^2}) \tag{5.12}$$

[2]In this chapter, we are primarily focus on the beamforming/beam-steering application, which is of significant importance for beyond 5G networks

where, R_{UMi} is the achievable throughput, and B_{sc} and B_{mc} are the alloted bandwidths to the user from the SCBS and MCBS, respectively.

However, to compute the received signal powers, i.e., $||y_{sc}||^2$ and $||y_{mc}||^2$ in Equations (5.11) and (5.12), we first subject the stream of data from the BS/SCBS/MCBS to the large scale fading (pathloss and shadow fading) and small scale fading (Rayleigh or Rician fading) phenomena. Subsequently, we utilize the the link budget formula in Equation (5.13) to compute the received signal power as follows,

$$P_r = P_t + G_t + G_r - PL - L_o \tag{5.13}$$

where P_r is the received power, P_t is the transmitted power, G_r is the gain at the receiver antenna, G_t is the gain at the transmit antenna, PL is the scenario dependent path loss and L_o are the other losses incurred at the transmitter and receiver feed, and other mismatches, etc. Note that, in this work we ignore the other losses L_o for the sake of simplicity. In addition, we define the pathloss models, based on the Close-in and 3GPP models [110, 115, 119, 121], as follows:

$$PL_{UMi} = 20\log_{10}(\frac{4\pi f}{c}) + 10n\log_{10}(d_{3D}) + \chi_\sigma \tag{5.14}$$

$$PL_{inh-LOS} = 32.4 + 20\log_{10}(f) + 17.3\log_{10}(d_{3D}) + \chi_\sigma \tag{5.15}$$

$$PL_{inh-NLOS} = max(PL_{inh-LOS}, PL'_{inh-NLOS}) \tag{5.16}$$

$$PL'_{inh-NLOS} = 38.3\log_{10}(d_{3D}) + 17.30 + 24.9\log_{10}(f) \tag{5.17}$$

where, PL_{UMi}, $PL_{inh-LOS}$, $PL_{inh-NLOS}$, and $PL'_{inh-NLOS}$ are the pathloss for the UMi scenario (for both LoS and NLoS setups), indoor office LoS scenario and the NLoS scenarios, respectively. Further, the shadow fading phenomenon is represented using χ_σ which is a gaussian distribution with zero mean and standard deviation σ. In addition, c is the speed of light, f is the central frequency of operation and d_{3D} is the 3D distance between the transmitter and receiver.

Next, for the received signal power computation in Equation 5.13, the transmit power, transmitter gain and receiver gain are required. While these parameters for the BS/SCBS/MCBS and UEs are readily available through existing literature [115, 119], a practical and realistic estimate of transmitter gain for an MS in the presence of single and multiple receivers is largely missing from the current literature. Note that in our study we assume the receiver gain of the MS as 0 dBi.

Since, the transmitter gain is a function of *Directivity* of the transmit antenna, we now discuss the achievable *Directivity* for our MS design in multiple user scenarios through Fig. 5.7. From Fig. 5.7, it can be seen that the *Directivity* shows a decreasing trend as the number of users increases. For evaluation purposes, we utilize the average *Directivity* in our study and analyze the performance of the MS for multi-user communication scenarios. We enlist the average *Directivity* values in Table 5.1.

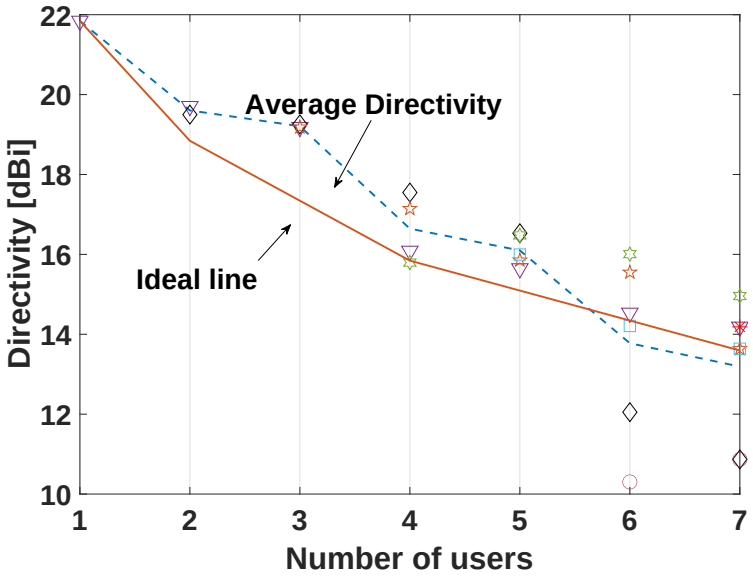

Figure 5.7: *Directivity* vs Number of Users

Table 5.1: Average *Directivity* of MS

Number of users	**Average *Directivity* (dBi)**
1	21.84
2	19.50
3	19.18
4	16.64
5	16.00
6	13.78
7	13.19

Lastly, we introduce Table 5.2, wherein we detail the other system model parameters/settings for the indoor and UMi scenarios. We reiterate that for the LoS paths a Ricean fast fading phenomenon is considered, whilst for the NLoS paths the Rayleigh fast fading is

Table 5.2: System model parameters

Parameter	**Indoor Office**	**UMi**	**Parameter**	**Indoor Office**	**UMi**
BS/SCBS operating frequency	28 GHz	28 GHz	MCBS operating frequency	–	3.55 GHz
BS/SCBS Fast fading model	Ricean	Ricean	MCBS Fast fading model	–	Rayleigh
Transmit Power BS/SCBS	20 dBm	23 dBm	Transmit Power MCBS	–	49 dBm
Transmit Gain BS/SCBS	0 dBi	30 dBi	Transmit Gain MCBS	–	17 dBi
MS Receive Gain	0 dBi		Directivity	cf. Table 5.1	
MS Antenna efficiency	0.9		Noise spectral density	-174 dBm/Hz	
BS/SCBS height	1.5m	10m	MCBS height	–	25m
UE height	1.5m	1.5m	MS height	1.5m	[1.5m, 3m, 4.5m, 6m, 7.5m, 9m]
Number of Monte-Carlo trials	100		Pathloss exponent for BS/SCBS LOS	1.7	2.1
Pathloss exponent for BS/SCBS NLOS	3.8	3.2	Pathloss exponent for MCBS LOS	–	2.0
Pathloss exponent for MCBS NLOS	–	2.9	Shadow Fading factor for BS/SCBS LOS	3.0	4.4
Shadow Fading factor for MCBS LOS	–	2.4	Shadow Fading factor for BS/SCBS NLOS	8.03	8.03

utilized. While these are simplistic fast fading channel models, our primary aim is to establish the distinct advantages that network operators can gain from our MS design in complex

wireless communication environments. In addition, we specify the scenario parameters such as BS/SCBS/MCBS heights, pathloss exponents, shadow fading standard deviation, transmit power and gains according to 3GPP specifications [110], METIS-II project [119] and recent research works such as [115, 117, 118, 121].

5.5 Evaluation

We evaluate the performance of our MS driven network in both indoor office (Fig. 5.5) and UMi scenarios (Fig. 5.6) based on the system models and parameters defined in Section 5.4. We perform the evaluation based on the channel capacity analysis and provide corresponding insights.

A Indoor office scenario

Before delving deeper into the channel capacity analysis, it is imperative to understand the behavior of the MSs in the wireless environment. By behavior we mean that, the SNR profile of the wireless channel corresponding to the reflected path from the MS. This is an essential step, as it highlights the channel properties of the reflected path from the MS. Thus, through Figs. 5.8 and 5.9 we present an analysis of the SNR and pathloss characteristics of the wireless channel (reflected path from MS) in an indoor office environment. In the simulation setup the MS was placed at distances of 0.9m to 8.9m from the BS. In addition, a single user was considered and moved from 1m upto 10m from the BS. Subsequently, the received SNR was computed for each of the location combination of the user and MS, and a profile was plotted. For the sake of brevity in this chapter we only show the SNR profiles when the MS is at a distance of 2.9m and 8.9 m from BS.

From the SNR profile in Figs. 5.8 and 5.9, it is evident that the received SNR is highest when the users are close to the MS. This is because the signal has to traverse two paths to reach the user from the BS. Hence, the overall SNR degradation scales up accordingly as the distance of the user increases from the MS. This gives an initial assessment of the fact that MSs are more effective for close range communications. Following this observation, we now present the channel capacity analysis for the indoor office broadcast environment through Figs. 5.10 and 5.11.

It can be observed from Fig. 5.10 that the overall channel capacity drops as the number of users increases. The reason is two folds: *firstly*, some of the users might be at a large distance from the MS which directly impacts the overall system capacity, and *secondly*, the reduction in the *Directivity* as the number of users increases reduces the MS transmit gain.

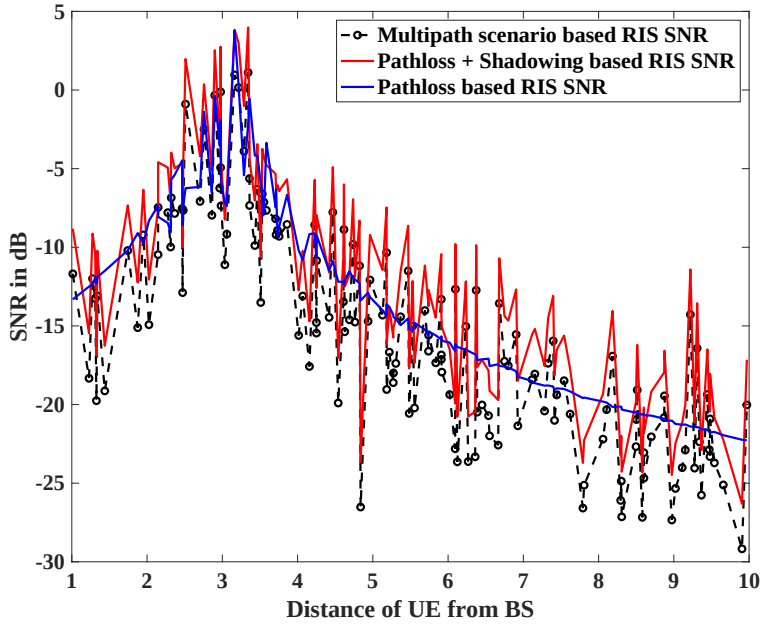

Figure 5.8: SNR vs Distance of UE from the BS (RIS at 2.9m from BS)

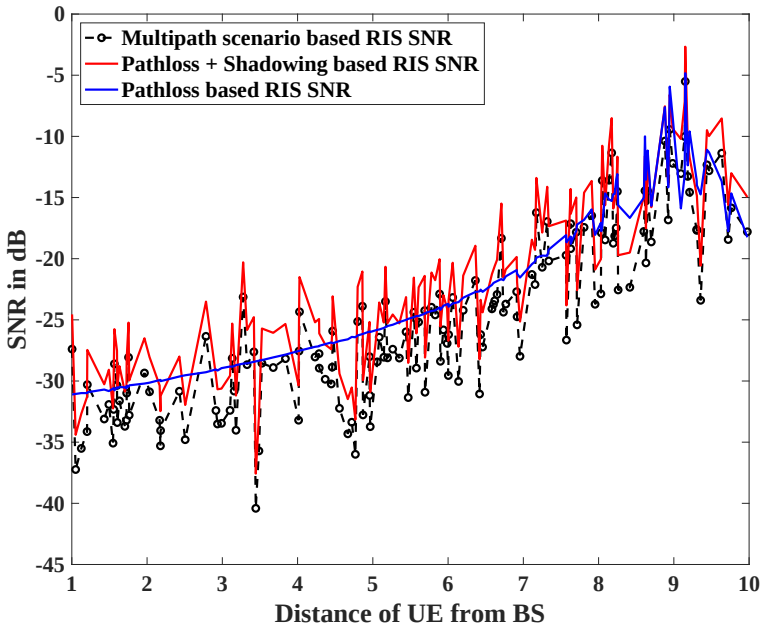

Figure 5.9: SNR vs Distance of UE from the BS (RIS at 8.9m from BS)

Furthermore, through Fig. 5.11, wherein we simulate the indoor office scenario with users being located in certain distance bands (e.g., users being between 1-2m), it is observed that irrespective of the number of users the channel capacity drops significantly with distance.

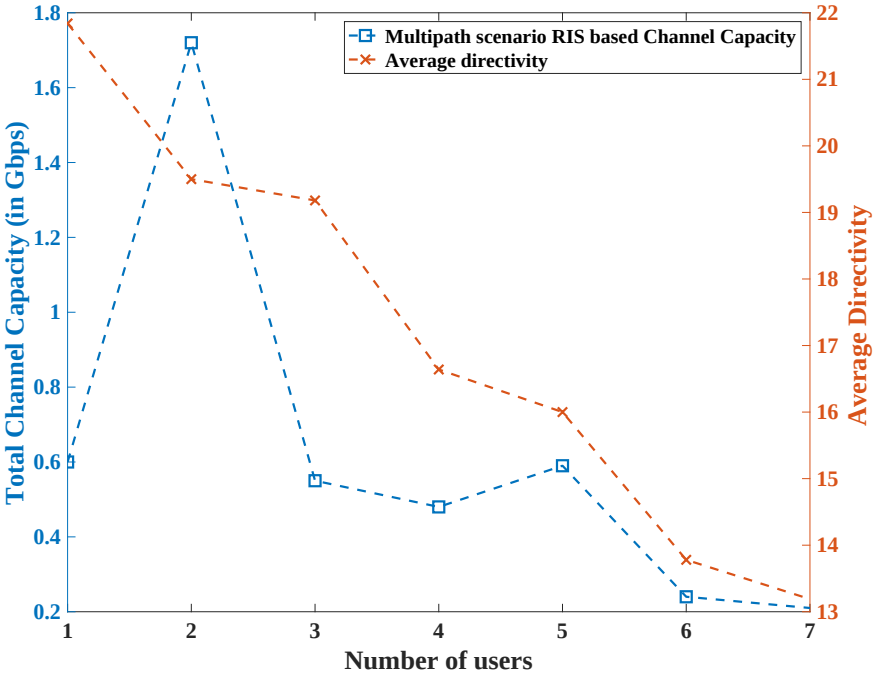

Figure 5.10: Indoor Office broadcast environment channel capacity analysis

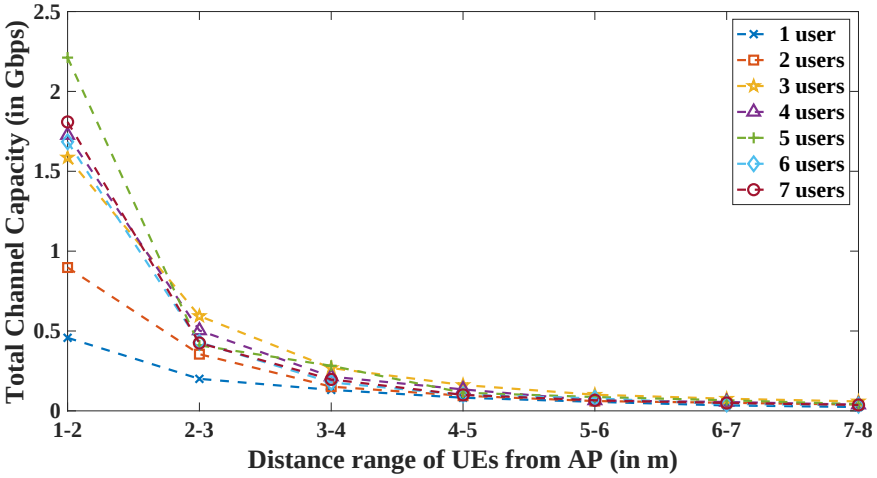

Figure 5.11: Indoor Office broadcast environment channel capacity vs distance to MS

B UMi scenario

We now present our channel capacity analysis for the UMi environment given the broadcast scenario. From Fig. 5.12, it can be seen that as the number of users increases the overall channel capacity also increases. The reason being that the users are able to connect to the SCBS via the MS, which was initially blocked by the obstacle. However, the growth in channel capacity plateaus as the number of users reaches 7. This is so because, the average directivity of the MS drops as the number of users increases. This, as a consequence,

translates into a plateauing effect on the overall channel capacity. Note that, the increase in the total channel capacity in the UMi scenario as compared to the Indoor office scenario, given increasing number of users, is a function of the system parameters defined for both scenarios in Table 5.2.

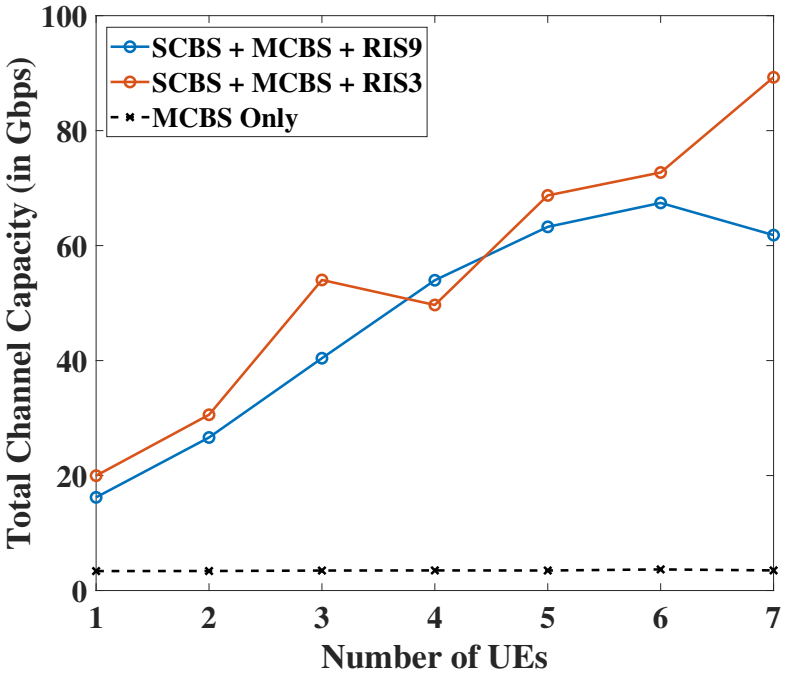

Figure 5.12: UMi environment broadcast channel capacity with RIS at 3m and 9m heights.

5.6 Summary

We introduced analytical theory for MS reconfiguration. This proposal provisions independent control over the radiation pattern lobes by which multi-user communication links can be established. Subsequently the analysis shows that the MS based system provides the best performance when the MS is located close to the users. Further we observed promising performance for indoor office and UMi environments given the broadcast mode of operation. Specifically, in the indoor office scenario, we observe that if the users are within 1-2m of the MS, then atleast 0.5 Gbps of data rate can be experienced by the users (with a peak data rate of $\sim$ 2.2 Gbps). Next, for the UMi scenario we observed that the MS based system provisions nearly 2 orders of magnitude more channel capacity in the presence of 7 users (which is the maximum number of users in our scenarios). Hence, through this work we have

shown the efficacy and effectiveness of the designed MS for $5G$ and beyond scenarios with multi-user applications.

Chapter 6

Radiation Pattern Prediction with Neural Networks

While tunability is an advantageous property of the programmable MSs, an important challenge associated with them is obtaining the characteristics of a reflected wave given the parameters of the incident wave and the states of each composing unit cell. Moreover, as illustrated in Fig. 6.1, a fast yet accurate estimation of the radiation pattern will facilitate multiple applications for 6G networks, such as the design, reliable functioning, and maintenance of MSs. Knowing the EM characteristics of each unit cell facilitates the calculation of the corresponding EM field. In most cases, the unit cell and thus the MS is reflective (the transmission coefficient is zero). So, we just need to possess reflective features (reflection amplitude and phase) of the unit cell to estimate the far-field pattern. Analytical models exist for describing and predicting the reflected EM field in some well-defined cases, such as beam steering [107] and focusing [122] of planar impinging waves. Still, these models introduce simplifications which can result in limitations in realistic setups and, consequently, reduced precision of results compared to the direct solution from Maxwell's equations [123]. Moreover, the iterative numerical full-wave simulations, which are widely adopted today and provide accurate predictions [38], are severely memory and time-consuming. Additionally, the design process largely relies on empirical reasoning or trial-and-error [124], which is inefficient and often ineffective.

On the other hand, ML techniques, and particularly NNs, owing to their ability to learn complex relationships between input and output data, are capable of solving differential equations, thereby circumventing the need for numerical calculations [123,125,126]. This fact provides the intuition towards another direction: since the MS EM response is essentially the solution to Maxwell's differential equations, it could be possible to design an ML construct

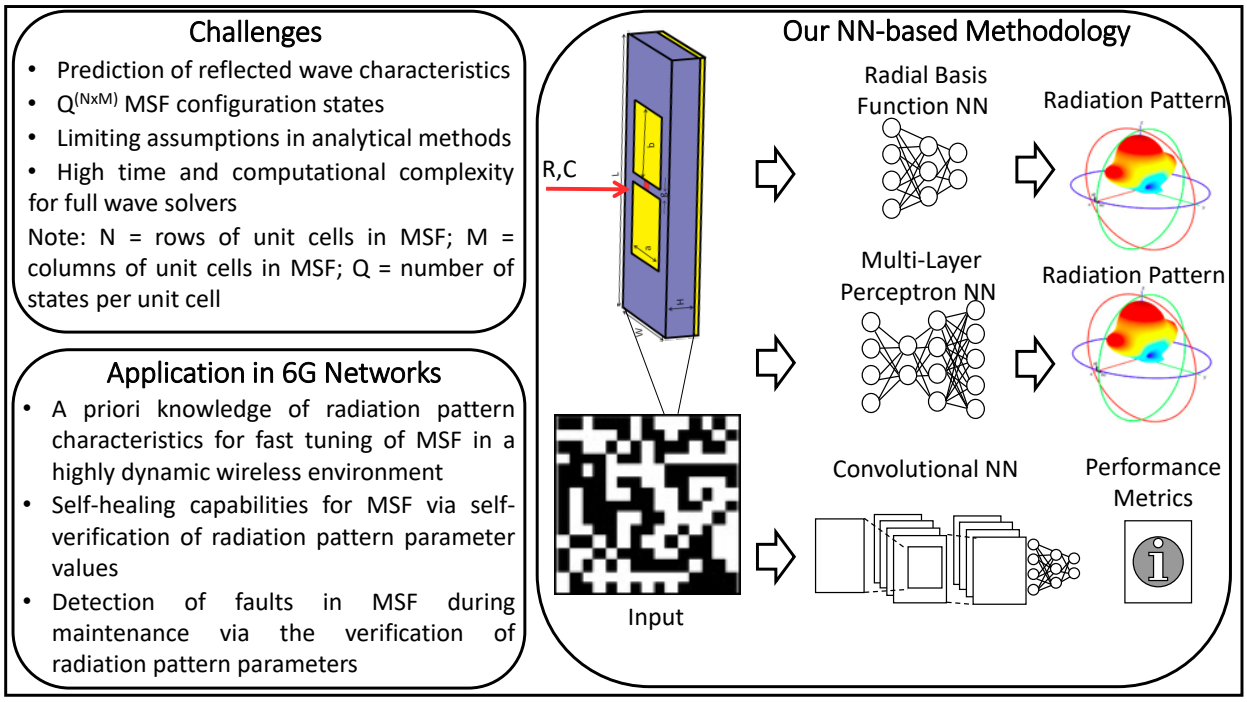

Figure 6.1: Neural Network-based approach for radiation pattern prediction: Challenges, Methodology and Application.

Table 6.1: Estimation of computation time for radiation pattern calculation with different methods

Methods	Computation time
Analytical Methods	$\sim$ 1s
Full-Wave Simulators	$\sim$ 1 hour
Neural Networks	$\sim$ 1 min

that predicts the EM response much faster. In Table 6.1 we have compared calculation time of the EM response for different methods. It can be seen that NNs take around a minute to compute the EM response, whereas full-wave simulators such as CST Microwave Studio take almost one hour to compute the same field with the same resolution. The accuracy of the NN can be as good as the data used to train it. So it gives us the speed of analytical models with the accuracy of simulations. Note that, we utilize the MS design and NNs studied in this work as well as the CST simulator to determine the order of computation time. It is important to state that, the numbers can vary depending on the dimension of MS and configuration of NNs, but the order of magnitude will remain similar. Moreover, this has been corroborated by multiple studies such as [2, 127, 128].

While many works use RIS in optimized but random-looking configurations [129] and sometimes truly random configurations [130], we emphasize a relevant application for wireless communications (i.e., beam steering) to maintain the communication link for a moving target. The proposed NN models the far-field radiation pattern and/or metrics. However, the dimensionality is large, and thus, completely random coding patterns will lead to random scattering patterns. Training the NN for all of them ends up with overfitting and complicates the training process. Moreover, we are interested in directive beams; hence, it is reasonable to discard chaotic radiation patterns. Nevertheless, for the sake of generality, we do not discard all the random inputs. Instead, we use an entropy control to guarantee a representative portion of random-looking and non-random-looking configurations. This approach not only speeds up the training but also reduces the Mean Squared Error (MSE).

Overall, this work provisions a data-driven NN-based approach for determining an accurate estimation of the radiation pattern or several measures of interest that enable the full characterization of the radiation pattern. As shown in Fig. 6.1, we study the performance of our data-driven methodology using different NNs, i.e., RBFNN, MLPNN, and the CNN. We describe the structure and functioning of these NNs in more detail in Section 6.3. We now elaborate on the salient contributions of this chapter, as follows:

- We develop an NN-based radiation pattern predictor, which, through our analysis, is established to be nearly as accurate as a full-wave simulation but with the computational complexity of an analytical method.

- To the best of our knowledge, this is the first method wherein certain important features of the reflected beam radiation pattern for a given MS, i.e. *Directivity, SLL, RA* and *HPBW*, have been predicted and effectively utilized for the complete characterization of the reflected beam radiation pattern. Consequently, this also provisions the capacity of our methodology in 6G networks (Fig. 6.1).

- We provide an analysis based on the accuracy of prediction of the aforesaid parameters, for the locally tunable MS scenario. Through the incremental design methodology, we establish a concrete framework and benchmark towards the selection of a CNN-based predictor for the reflected beam radiation pattern. Specifically, we compare the performance of a CNN-based predictor with an MLPNN based predictor. The comparative study reveals that the CNN predictor provisions an accuracy similar to the MLPNN predictor. It is imperative to state here that a CNN incurs significantly lower computational complexity as compared to an MLPNN.

The remainder of this chapter is organized as follows: In Section 6.1 we present the current

state of the art. In Section 6.2 we describe the incremental design framework, including the multiple scenarios that we have analyzed. In Section 6.3 elaborate upon the methodology that we have utilized for evaluating the multiple scenarios studied. In Section 6.4 we present the evaluation. We conclude the chapter in Section 6.5.

6.1 State of the Art

ML methods over the past decade have gained significant importance in multiple sectors such as aerospace, medicine, and telecommunications [131–133]. Further, since the laws of electromagnetism, fluid and aerodynamics are governed by well-known differential equation sets, the success of ML techniques in such domains is prospective [123,125,126]. Recently, several works in the research community proposed ML-based algorithms to design and validate EM response of MSs [128,134–140]. Additionally, there are other data-driven approaches, such as the Particle Swarm Optimization (PSO) method for designing a wide range of MSs. For example, PSO-based methods are used for designing artificial magnetic conductors, designing time-delay equalizer MS for EM band-gap resonator antenna, and realization of a low profile bandpass frequency selective surface [141]. The aforesaid approaches are consolidated into a schematic diagram and are compared with our proposed method in Fig. 6.2. Furthermore, we have organized the existing approaches into two distinct categories, i.e., *forward design approaches* and *inverse/MS design approaches*. Whilst *forward design approaches* consist of methods wherein the MS coding is used to predict the reflected wave radiation pattern, the *inverse/MS design approaches* utilize the reflected wave radiation pattern as a feedback to optimize the MS coding.

A Forward Design Approaches

In [139], an evolutionary algorithm that generates cell configurations and evaluates the fitness of each configuration by predicting the reflection phase with a trained CNN (a 101 layer deep residual network) for its given specific pattern has been proposed (Fig. 6.2(c)). However, this CNN, which serves as a speedup of the optimization process of the evolutionary algorithm, is trained by previously encoding the output phases into a one-hot vector of length 360. Each element of the vector represents a discrete degree. Consequently, a problem that is purely based on regression is now converted into a classification problem. This results in a loss of resolution and thus, crucial information with regards to the order and distance between degrees. Furthermore, in [139], the proposed CNN approach only provides good results for output radiation patterns with one, two, or three beams. Therefore, for using this approach

as a reflected phase predictor, the user needs to know *a priori* how many lobes the resulting pattern will have. And given the fact that a method to *a priori* deduce the number of lobes has not been proposed in the aforementioned work, it thus limits the ability to generalize this approach to predict any reflected beam pattern.

Notably, other works, such as [142], have used ML tools for solving different EM problems as a replacement of conventional numerical simulations. In [142], an encoder-decoder structure was employed for inferring the internal fields of arbitrary three-dimensional discretized nanostructures.

B Inverse/MS Design Approaches

In [134], the authors propose a smart EM sensing mechanism, wherein the MS coding pattern, as well as the information decoding parameters, are jointly optimized (deduced) to extract the latent scene (human gesture) information. To perform the same, the authors propose to utilize two deep NNs and an optimizer (Fig. 6.2(a)). The deep NNs are termed as measurement ANN (m-ANN) and reconstruction ANN (r-ANN), wherein the m-ANN employs two CNNs. Further the m-ANN, in collaboration with the optimizer, determines the optimal MS coding pattern. The r-ANN on the other hand employs three CNNs, and in coordination with the optimizer identifies the latent scene information from the received EM data. Next, in [135–138], Generative Adversarial Networks (GANs) have been used to solve the inverse problem, i.e., to determine the MS unit cell structure, given the desired frequency response (Fig. 6.2(b)). Additionally, in [135] a CNN is utilized as a simulator to verify the accuracy of the frequency response of transmittance from the generated structures during the training phase of the GANs generator component. Similarly in [136], a GAN-based simulator, faster than the conventional numerical simulation tools, has been proposed. This simulator is one of the components of a system that performs an inverse design to select an MS pattern from a user-defined dataset to match the required input optical spectrum. Additionally, in [137] GANs have been employed to design the MSs that can generate complex tensorial Radio Frequency (RF) responses. Further, and similar to previous methods, it also uses a CNN-based simulator to validate the RF response of the generated MS configurations. Concretely, the CNN simulates and generates the scattering parameters for a given unit cell shape. However, the proposed simulator does not evaluate the complete radiation pattern of a locally or globally tunable MS. Lastly, amongst the GAN-based methods, [138] works with a variant of the conventional GANs, i.e., Wasserstein GAN (W-GAN), to achieve its goal of identifying the most suitable MS design.

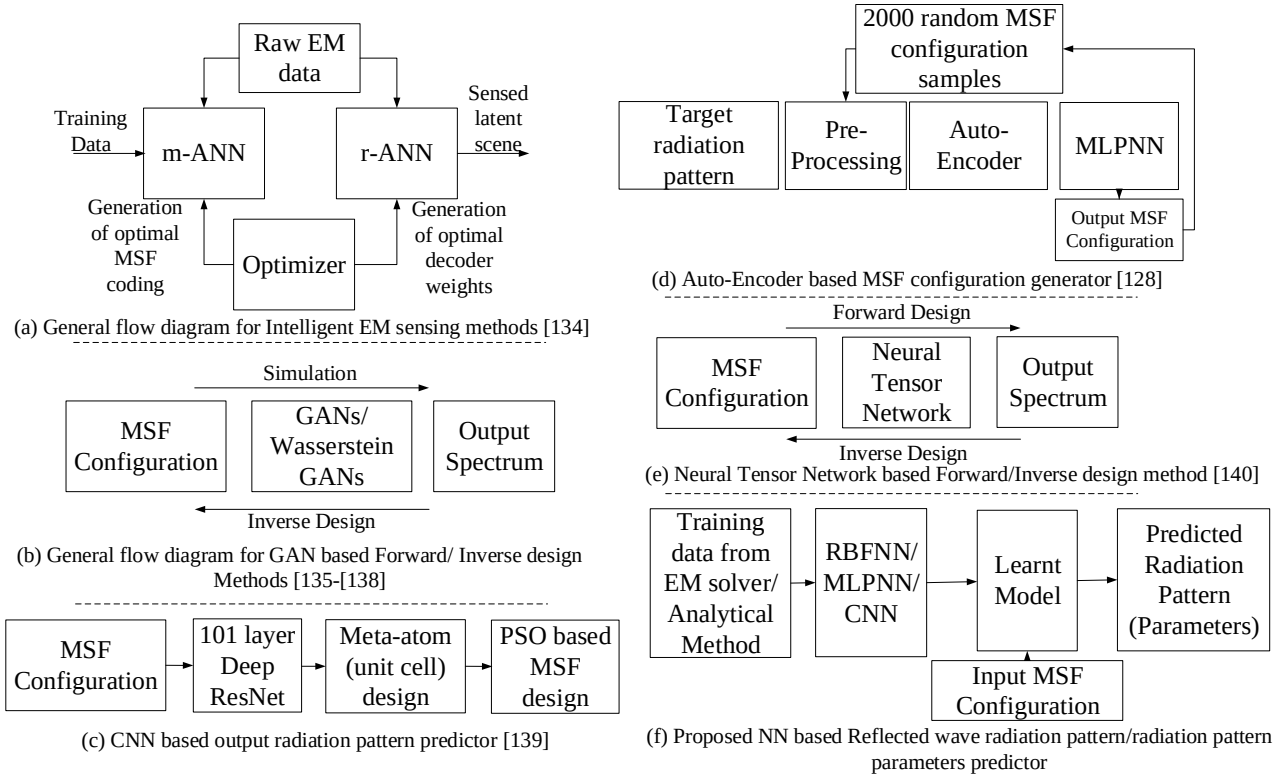

Figure 6.2: Schematic representation of state of the art approaches and the proposed method.

Further, other research efforts such as [128] and [140] exploit other deep learning techniques to perform the task of MS design. Concretely, in [128] an auto-encoder based approach has been adopted (Fig. 6.2(d)). In this method, the auto-encoder enables capturing the most significant aspects of the input data, i.e., the desired reflected beam radiation spectrum. Subsequently, it facilitates the fully connected MLPNN network in determining the requisite MS profile for the demanded radiation pattern. Moreover, in [140], a combination of the traditional NN, such as MLPNN, and Neural Tensor Network (NTN) based approach has been adopted for designing the MS (Fig. 6.2(e)). However, to do the same an initial simulation framework consisting of two NNs, which employs the NTN, have been prepared. These NNs aim to predict the amplitude and phase of the reflected wave from the MS. This is performed by using these two NNs to predict the real and imaginary part of the desired EM response, respectively. Following this accurate prediction, inverse design methodologies are then adopted to formulate MSs conforming to a wide variety of design objectives, thus highlighting the versatility of the proposed approach.

Given the aforesaid studies, to the best of our knowledge, we claim that, for estimation of the reflected wave radiation pattern, our methodology provides a *simpler* solution. This can

be highlighted from the fact that the study in [134] utilizes a set of two different deep ANNs, both comprising multiple CNN layers. Specifically, the m-ANN, which provisions the MS coding for the optimal illumination of the field of interest, applies two deep CNNs. The CNN we use in the third scenario may end up generalizing to an NN with a similar architecture than m-ANN, but in this chapter, we prove that with a simpler CNN architecture, we can obtain relevant features of the radiation pattern instead of the full radiation pattern. Also, in this study, MS coding pattern is optimized for a specific application (shaping planar incident wavefront) while we conducted a general study (i.e., prediction of radiation pattern or performance metrics for any reconfiguration pattern). Next, the models defined in studies [135–138] work with GANs/W-GANs. These are again more complex DNN architectures as compared to the relatively simple CNN framework that we propose. Further, in [135–138] the objective is to study the inverse problem, i.e., to determine the MS configuration from a set of input radiation patterns. Hence, such solutions do not apply to the objective of the problem that we aim to solve in this work. Moreover, the work done in [139] results in a loss of resolution and applies to only some well-known cases. Additionally, in [128] and [140], the proposed methodologies either suffer from scalability issues (MLPNN is not scalable for large MS configurations) or develope multiple complex DNN architectures (such as two DNNs with the first layer being an NTN), respectively. Hence, from Fig. 6.2(f), it can be observed that proposed methodology, which we will detail next, is unique compared to the state-of-the-art approaches (Figs. 6.2(a)-(e)) in terms of its structure and approach towards predicting the output radiation pattern/parameters. Table 6.2 lists the state-of-the-art papers comparing design approach, application, and year of the publication.

Table 6.2: Summarizing the state of the art data-driven approaches

Design approach	Application	Year	Reference
Optimizer	Time-delay equalizer	2017	[141]
Two Deep NN and optimizer	Smart sensing	2020	[134]
GAN and CNN	Frequency response prediction	2018	[135]
GAN	Inverse design	2019	[136]
GAN and CNN	MS design	2019	[137]
GAN	MS design	2021	[138]
CNN	Reflection phase prediction	2019	[139]
Auto-encoder	MS design	2019	[128]
MLPNN and NTN	MS design	2019	[140]
Encoder-decoder	Field prediction	2020	[142]

6.2 Incremental Design Framework

We now describe the framework for our radiation pattern predictor, wherein we consider two broad scenarios, i.e., homogeneous and heterogeneous MS configurations, and incrementally demonstrate that it is possible to predict the features of the reflected wave from a given MS configuration through data-driven learning approaches. Note that, depending on the scenario, the MS is represented by a matrix of unit cell states. Since the unit cells are not extremely small compared to the wavelength and phase reflection is the only parameter that is different for each unit cell, the coupling effect between the unit cells is negligible. The accuracy of this approximation is in excellent agreement with full-wave simulations [2,38,107] and have been used in different analyses [90, 143, 144].

Next, the homogeneous MS configuration scenario is further expanded to two specific scenarios. These scenarios are established based on the underlying unit cell configurations of the MS, and are listed as follows:

- The non-tunable scenario consists of a non-tunable unit cell configuration across the MS. Such a configuration is termed a non-tunable MS.
- The globally tunable scenario consists of a matrix of unit cells across the MS, wherein the unit cells have the same values for the tunable resistance R and capacitance C. Such a configuration is termed a globally tunable MS.

The unit cell design is a modified version of the previous work [41] which can be a tunable perfect absorber for different incidence angles and have tunable anomalous reflection toward different directions at 5 GHz. Fig. 6.3 presents the schematic of the unit cell in which two metallic patches are connected via tunable R and C elements. The PCB thickness is 3.18mm, the relative permittivity is $\epsilon = 2.2$ and loss tangent is $\delta = 0.0009$.

Subsequently, the heterogeneous MS configuration scenario, or the locally tunable MS, refers to the scenario where the unit cells can have different values of R and C associated with them. An illustration of these three scenarios that we have analyzed in this work, is presented in Fig. 6.4. It is worth stating here that in our framework we analyze the efficacy of NN-based approaches by starting from a simple scenario, i.e., the non-tunable (static) MS, to a more generic and complex scenario, i.e., the locally tunable (Programmable) MS. Hence, we now describe these scenarios and the associated methodologies for radiation pattern prediction in detail through Sections 6.2 and 6.3, respectively.

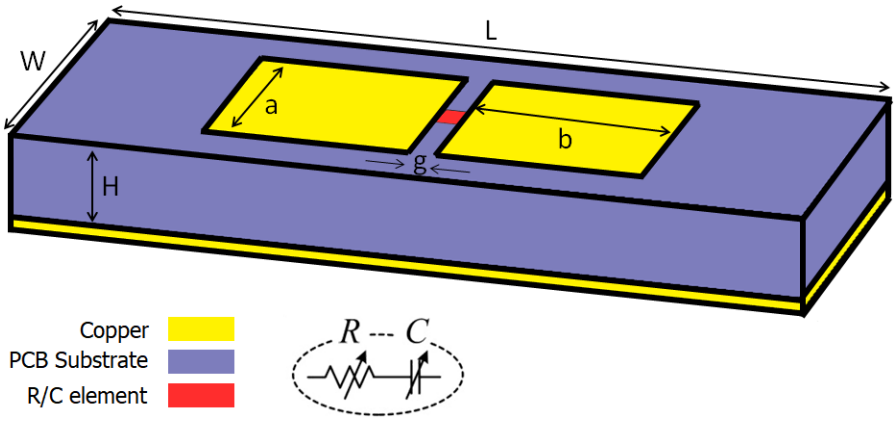

Figure 6.3: Schematic of the unit cell for the proposed MS. The dimensions are $L = 30$mm, $W = 12$mm, $H = 3.18$mm $a = 7.85$mm, $b = 7.50$mm and $g = 1$mm.

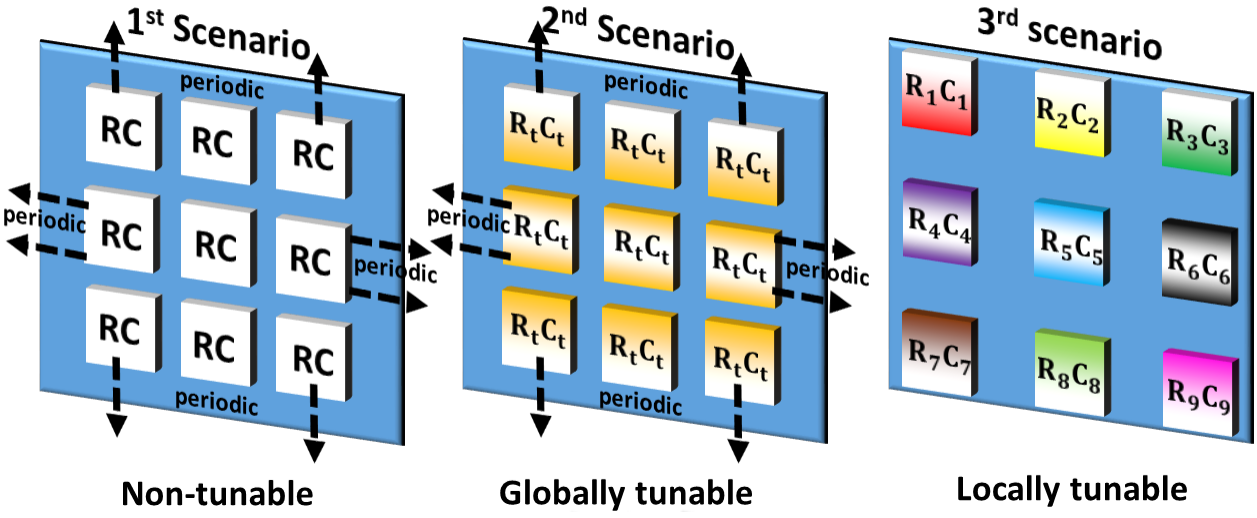

Figure 6.4: Diagram of the three scenarios utilized in the Incremental Design framework. Non-tunable and globally tunable scenarios correspond to the broader homogeneous MS configuration category, while the locally tunable scenario corresponds to the heterogeneous MS configuration category.

A Homogeneous MS Configuration

In this scenario, w elaborate upon the two scenarios, i.e., the non-tunable MS and the globally tunable MS, in the text that follows.

A.1 Non-tunable scenario (non-tunable, single unit cell / full radiation pattern estimation)

Interaction coefficients for the general analysis of MSs can be very complicated [145]. Note that such MSs can be used for focusing [146] and polarization selection [147]. Next, based on the Floquet theory, we can approximate large enough ($>> \lambda_0/2$) periodic structures with an infinite array of the same unit cell configuration (Fig. 6.4, Case 1). This is because the fields propagate only with phase delays together with multiplication by periodic coefficients. This translation is considered automatically with the usage of periodic boundary conditions in the simulations, thus reducing the complexity. This is a very extended practice in this kind of study [148]. Thereby, we just consider one unit cell and apply periodic boundary conditions to model the whole MS. Plus, in the prediction process, it is presumed that the azimuth and elevation angles of the incident EM wave are given.

A.2 Globally tunable scenario (tunable single unit cell / full radiation pattern estimation)

In this scenario, we introduce a data-driven model to predict the complete reflected wave radiation pattern for a globally tunable MS. One of the reasons for studying the globally tunable MS configurations is the role that they will play in applications such as perfect absorber [149], frequency-tunable absorber [150], amplitude modulator [151] and, polarization control [152]. Same as before, in this scenario the MS consists of an infinite array of unit cells, wherein the same tuned unit cell configuration is repeated *ad infinitum* (Fig. 6.4, Case 2).

B Heterogeneous MS Configuration

B.1 Locally tunable scenario (tunable full surface / radiation pattern attribute estimation)

Here, we elaborate upon the locally tunable scenario, which expands our incremental framework to a locally tunable MS (Fig. 6.4, Case 3). Such MSs enable applications such as object tracking [130, 153, 154] and sensing [134, 155]. Hence, they will be of significant importance in 6G networks.

In this scenario, the inputs for our NN-based framework are two-dimensional matrices, with each value representing the 8 possible states of the unit cell at the corresponding position in the MS. Additionally, the corresponding MS is a 12×12 matrix of unit cells. The framework thus attempts to predict, for normal incident angles, the measures of the reflected beam radiation pattern for an MS with a set of given unit cell state configurations. Note that, the number of possible configurations for the MS under study, is 8^{144}. Due to the large dimentionality, we investigate a data-driven model to predict four measures of interest that characterize the reflected wave radiation pattern instead of the radiation pattern itself. These measures of interest are the *Directivity*, *SLL*, *RA* and *HPBW*.

6.3 Methodology

Training an NN with environmental parameters like the location and geometry of the obstacles requires specific information. Simulation of this complex medium is a challenge and modeling it with analytical methods is not accurate. So, in this framework, we assumed the RIS in free space whereas the environment does not affect the RIS response (i.e., objects are not in the reactive near-field of the RIS). Nevertheless, this doesn't mean the scenario under study is unrealistic because the input of the NN is the reconfiguration profile of the MS and the output is the radiation pattern. So, by learning this relationship between the reconfiguration profile and the MS response, we can manipulate the radiation pattern to optimize the communication channel. Moreover, free space RIS was the subject of several recent works such as free space optical systems [156], smart radio environments [157–159], vehicular communication systems [160, 161], and line of sight wireless communications [162]. Regardless of the actual characteristics of the source (e.g., horn antenna), far-field impinging waves upon the MS can be considered to be locally planar [159]. So, we assumed a plane wave with a normal incident that illuminates the MS area uniformly.

A Homogeneous MS Configuration

A.1 Non-tunable scenario

For the simulations in the non-tunable scenario, we sweep the azimuth and elevation angles from 0 to 89 degrees with respect to normal incidence direction alongside a resolution of 1 degree. Given that the transmittance is 0, we do not need to evaluate negative elevation angles. Moreover, due to the assumed unit cell symmetries, we do not need to explore all the azimuth angles.

The NN model that we explore for our data-driven framework is RBFNN. It is a three-layer fully connected NN, wherein the inputs from the input layer are fed to a hidden layer via weighted links. At the hidden layer, a euclidean distance between the input and the link weight vector, also known as neuron's center is computed [163]. The activation function of the neurons is the Gaussian function, and these are also known as the basis functions [163]. Consequently, the output of the neurons in the hidden layer is determined by the output of the Gaussian function operated over the distance between the input and neuron's center. The final output is obtained by combining the weighted outputs of the neurons in the hidden layer [163]. Such a paradigm is *a priori* very interesting for our approach since it models spatial variables. This is in contrast to the MLPNN, in which the basis functions are based on the dot product. Concretely, this enables the RBFNN to learn the non-linear relationship between the incident and reflection angles of the EM wave more effectively than an MLPNN, which is inherently based on a linear transformation.

Note that, for the accuracy of evaluation of the RBFNN, we set the MSE goal to be 10^{-11} and the spread constant to 1. The spread constant here refers to the spread (or variance) of the Gaussian radial basis functions. This hyper-parameter consequently plays a crucial role in determining how the input layer is mapped onto these basis functions [164]. Further, 8100 samples were collected using an EM simulator, which in this work is the CST Microwave Studio, of which 85% were spend for training and validation and the rest, i.e., 15%, for evaluating the model generalization (which is usually referred to as the testing process). For non-deep learning scenarios, the aforementioned set of hyper-parameters lie within the range of values that are chosen usually [139].

A.2 Globally tunable scenario

In the globally tunable scenario, we vary the values of the parameters that characterize the physical structure of the unit cell, i.e., resistance R and capacitance C. However, as described earlier, the entire MS consists of the same unit cell configuration throughout, i.e., all tuned unit cells will have the same value for R and C. For brevity, we studied only normal incident wave direction. However, if required, our model can be extended to any incident wave direction (incident angle). Further, we sweep the values of R from 1Ω to 100Ω with a resolution of 1Ω, and that of C from 0.1 pF to 1 pF with a resolution of 0.01 pF. The framework we use in this scenario for our data-driven approach is the MLPNN.

Moreover, unlike scenario 1, wherein the spatial characteristics of the incidence and reflected angles of the impinging wave were to be learned, in scenario 2 the input features R and C lack any spatial characteristics. Thus, we do not evaluate RBFNN for this case.

Furthermore, and owing to its relatively poor performance in scenario 1, we do not explore CNN for scenario 2.

For the MLPNN, we utilize a single hidden layer of 20 neurons. The training algorithm used was scaled conjugate gradient [165] without any regularization. The non-requirement of any regularization in our model was due to the fact that it has a very small amount of parameters. Similar to the non-tunable scenario, we obtained the samples from an EM simulator and delimited 85% of them for training and the rest for testing purposes. We collected 9191 samples, which is slightly more than the number of samples collected for the non-tunable scenario.

B Heterogeneous MS Configuration (Locally tunable MS)

As mentioned in Section B.1, for locally tunable MS (Fig. 6.5), we have to deal with a large input dimentionality (8^{144}). To train an NN and test it we need numerous input data (10^6). Since unit cells are tuned differently, it is not possible to adopt periodic boundary condition. This increases the computation time. Given our computational limitations, collecting enough samples through an EM simulator, would take an extremely long time. So, in addition of hundreds of simulated samples we collected thousands of samples through an analytical method. With this technique, we trained an NN as fast as analytical solutions and as accurate as EM solvers (c.f. Section 6.4). Therefore, in this chapter, and for this scenario, we demonstrate that:

- Our ML approach predicts the measures of the reflected beam pattern accurately.
- Provided that there is enough computational power, we can extrapolate the same model and methodology to the scenario where we have more samples from an EM solver.

Training and Testing dataset generation – Next, for ML, normally random selection is used to generate samples for training. However, random inputs of the gradient for unit cells will always end up in a random scattering pattern. These patterns, in addition to being non-learnable, will not be of significance for design purposes. Thus, the samples collected for training are not entirely random combinations within the whole space, wherein the total number of combinations, as mentioned earlier, is $Q^{(N\times M)} = 8^{144}$.

Additionally, in our approach, a sample generation space is defined to control the entropy of the input data [166]. Specifically, low entropy regimes will only be useful to train specific options, i.e., those that require ordered codings (focusing, beam steering), but they will not suffice scenarios that need near-to-random codings (Radar Cross Section (RCS) reduction).

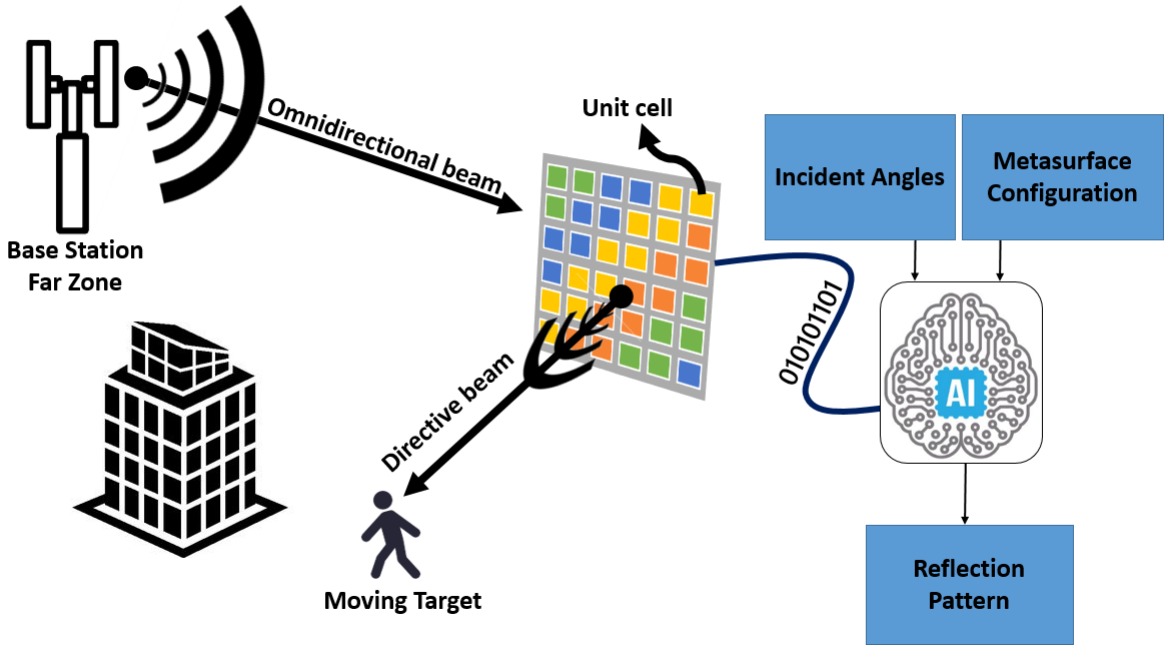

Figure 6.5: Graphical exhibition of the system model: Base station at the far zone radiates with an omnidirectional pattern. Planar impinging wave on the MS reflected toward the target with a precise configuration of the MS imposed by the well-trained NN.

Hence, a wide entropy range, such as the one as we have described above, will be essential to train the NN and enables it to generalize effectively. Using a simple algorithm to generate random samples for MS configuration, there is a huge chance to get high entropy data. In most cases, the products of the algorithm are unrelated configurations. Due to the huge number of possibilities, we cannot iterate the data generation frequent enough to make sure the low entropy data is produced as well. Here, we introduced a method to overcome this issue. In this procedure, a configuration is acquired with Eq. 2.2 for a random pair of reflection angles. Thereafter, an entropy factor is introduced into the matrix of configuration with an adjustable size that allows us to control the entropy of the final configuration ranging from 0 to 100%. With this method, generated data includes configurations with uncorrelated data with high entropy as well as meaningful configurations with low entropy. So, we obtained a vast range of entropy with a reasonable number of iterations (e.g., 10^6) which is precisely what we need to prevent overfitting.

Subsequently, a criterion on the radiation pattern (e.g., Directivity) can be applied to discriminate interpretative configurations. This criterion translates the qualification of the NN on a specific configuration. Therefore, we have a system that automatically checks if the new configurations used for predicting its measures can be used (with a reasonable granted accuracy) in the NN for prediction.

Adopting the aforementioned procedure, the number of samples that were collected for training and testing the model of the locally tunable scenario was 10^5. Amongst these samples, and similar to the first two scenarios, 85% of them were used for training and validation whereas the remaining 15% were stored in a completely separate set for the testing phase of the model. Further, from the training and validation set, 80% of the samples were used for training, while the remaining 20% were used for validation. The values of the pixels in the input images were normalized by performing a max-min escalation, without modifying their variance. This is not the case for our input variables, as the variance of each pixel is part of the relevant information the model uses for prediction.

However, it is important to state that standardizing the features is important when we compare measurements that have different units, as variables that are measured at different scales will not contribute equally and could end up creating a bias. And since this is the case for the target variables, the target samples for both training and testing sets were standardized by subtracting the mean of each of the measures and dividing them by their respective variances.

Prediction System Operation – Following this, once our model is trained for a given upcoming configuration, it performs an analytical check of the given configuration and determines if it is totally random or not. If after the analytical check it is determined that the MS configuration is not totally random, the trained model is used to predict the measures of interest. Instead, if it is determined otherwise during the analytical check, meaning that the configuration outputs a random radiation pattern, it is discarded as the model cannot provide suitable results for this configuration. Concretely, since NN training is time-consuming, inputs that are not suitable for the application under study are removed. Moreover, and as we have already stated, we employ the entropy control methodology for ensuring diversity in the inputs for NN training. However, during the prediction stage, configurations that are not suitable for the specified application are eliminated via the analytical check. Fig. 6.6 illustrates the aforesaid steps performed in our system for predicting the measures of interest from an upcoming MS configuration, once the model is trained.

NN Models – With this background, we now delve deeper into the setup of the two NN models that we use for our evaluations within the locally tunable scenario. Note that, for this scenario, unlike the non-tunable scenario of the homogeneous MS configuration (Section A.1) where the spatial characteristics of the incidence and reflected angles were to be learned, we do not use the RBFNN since we are not considering any spatial characteristics in our input space.

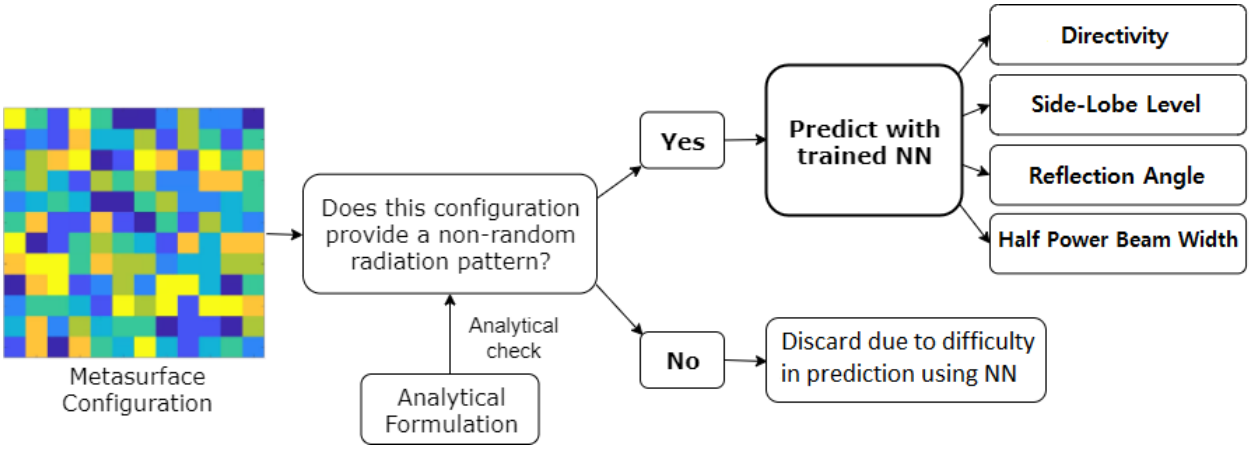

Figure 6.6: Diagram of the steps performed inside the system once the model is trained for the Locally tunable scenario.

B.1 Multi-Layer Perceptron Neural Network

As part of our methodology, illustrated in Fig. 6.6, we adopt NNs for predicting the measures of interest of the reflected beam radiation pattern. Note that, we consider measures of interest here as against the full radiation pattern, given the prohibitively large nature of the search space in highly scattering environments for predicting the complete reflected wave radiation pattern. Next, in this section, we consider MLPNN as our candidate NN. For the MLPNN case, the input images of 12×12 pixels which represent the unit cell configurations are flattened into vectors of 144 variables before being introduced into the NN.

Fig. 6.7 shows the structure of the MLPNN approach for the locally tunable scenario. The number of hidden layers and the neurons per layer was set to 2 and 100, respectively. A conclusion, with regards to the aforesaid parameter values, was reached after extensive user-driven exploration since sweeping across all the possible combinations was not computationally feasible. The rest of the parameters for the MLPNN are listed in Table 6.3.

Table 6.3: Multi-Layer Perceptron Neural Network parameters

Parameter name	**Value**
Regularization type	L2
λ	0.8
Training algorithm	scaled conjugate gradient
Number of hidden layers	2
Neurons of 1st hidden layer	100
Neurons of 2nd hidden layer	100

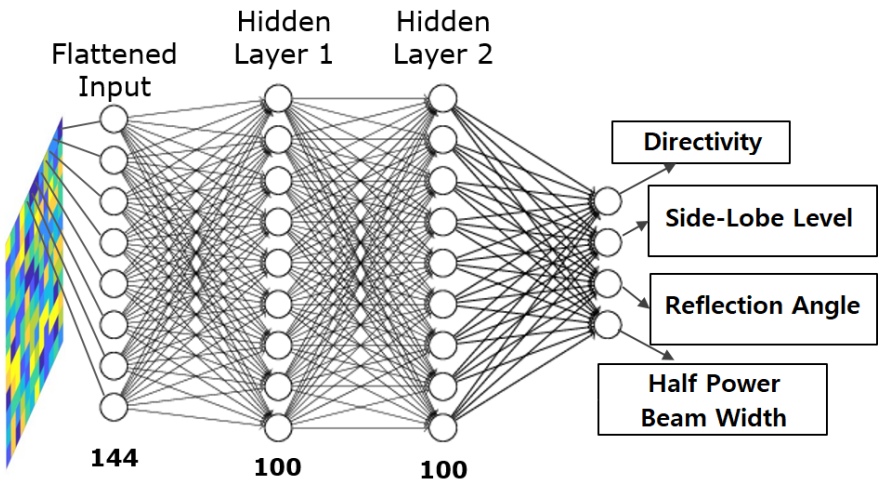

Figure 6.7: Structure of the Multi-Layer Perceptron Neural Network in the Locally tunable scenario.

As we can observe from Table 6.3, the training algorithm selected is the scaled conjugate gradient which accelerates the convergence rate for first-order algorithms, like the steepest descent, while avoiding the high computational cost of second-order methods, such as Newton's method. Since the default learning rate parameter worked reasonably well for the NN training, i.e., it provided a reasonable convergence time and performance, we did not deem it necessary to tune it further. Whilst this could be a point of optimization, we leave it for a future work as our objective in this chapter is to demonstrate the efficacy of the method.

Next, regularization is a way to limit the complexity of a model and hence reduce the chances of overfitting by penalizing the most complex solutions in the cost function. Thus we employ an L2 regularization in our methodology. Specifically, in the model, this is enforced via the λ hyper-parameter.

B.2 Convolutional Neural Network

Another NN that we explore for our methodology is the CNN. For the CNN case, the input images of 12×12 pixels and additionally a channel, which represents the unit cell configurations, are directly introduced to the NN.

Fig. 6.8 illustrates the structure of the CNN-based approach for the locally tunable scenario. It is composed of three convolutional layers that consist of 64, 32, and 32 filters, respectively. Further, a max-pooling process is performed after each of them. For all the convolutional layers, the filter size is 3×3 pixels and the stride is 1. As we do not use zero paddings, the dimensionality of the intermediate images which represent the activations is

reduced at each layer. They are followed by a fully-connected layer with 100 neurons and an output layer with a linear activation function. Similar to the MLPNN case, the architectural parameters of the CNN are a result of extensive user-driven exploration, since sweeping around all the possible combinations was not computationally feasible. We enlist the most significant CNN architecture-related parameters in Table 6.4.

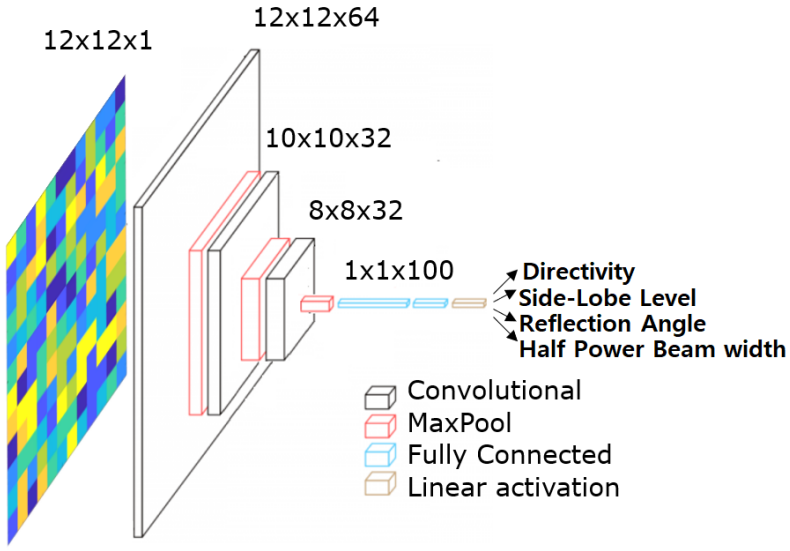

Figure 6.8: Structure of the Convolutional Neural Network in the Locally tunable scenario.

Table 6.4: Convolutional Neural Network architecture parameters

Parameter name	**Value**
Regularization type	Dropout
Dropout factor 3rd conv. layer	0.2
Dropout factor FC layer	0.25
Training algorithm	Stochastic Gradient Descent
Learning rate	0.001
Momentum	0.9
Decay	1e-4
Num. of conv. layers	3
Num. of FC layers	1

As we can observe, the training algorithm selected is the stochastic gradient descent (Table 6.4). As it is a first-order optimizer, the steps of the optimization process are linearly done

concerning the direction of the maximum gradient. Thus, the length of the steps needs to be defined by the learning rate hyper-parameter. The learning rate, decay, momentum, and the number of both convolutional and fully connected layers, specified in Table 6.4, are set following a user-driven exploration. It is important to state here that, we do not use zero paddings as it would introduce noise to the data, by essentially forcing a boundary that would be non-existent on a continuous MS plane.

Additionally, the third convolutional layer and the fully connected layer are regularized through a dropout process. This process consists of randomly ignoring a given number of layer outputs during the training process. Therefore, the layer with the dropout process is treated as a layer with a lower number of nodes and connectivity to the previous layer. In effect, each update to a layer during training is performed with a different "view" of the configured layer. Dropout factor controls the number of nodes and is ignored randomly. For the third convolutional layer and the fully connected layer, the dropout factors are 0.2 and 0.25, respectively. These values were selected following the same procedure explained for selecting the λ regularization parameter in the MLPNN.

6.4 Evaluation

Given the framework discussed in Sections 6.2 and 6.3, we now present the evaluation for each of the scenarios discussed within this framework and highlight the relevant outcomes and insights. The results obtained from our NN-based prediction system have been compared to the ground truth results obtained via the CST simulator.

A Homogeneous MS Configuration

A.1 Non-tunable scenario

For the non-tunable, single unit cell/ full radiation pattern case, the trained RBFNN was able to predict the radiation pattern for any given angle of incidence with an R^2 test of 0.9994. Therefore, this assists us in validating our hypothesis that ML models can accurately predict the reflected wave radiation pattern from a single unit cell for every angle of the incident wave. Fig. 6.9 illustrates a visual comparison between the predicted radiation pattern by the trained RBFNN and the true diagram obtained through EM simulation, for the azimuth and elevation angles that were not present in the training set. So, our prediction system can accurately learn and generalize for untrained/unseen angles within the training dataset.

Further, when a CNN was applied for this case, the observed MSE was 10^{-7}, which is significantly worse as compared to the accuracy obtained via the RBFNN approach (the

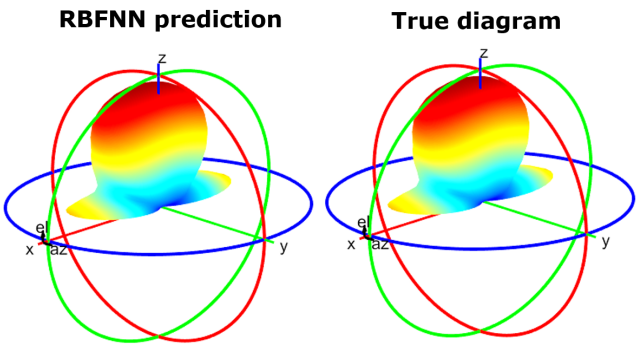

Figure 6.9: Comparison between the predicted radiation pattern by the RBFNN of the non-tunable scenario (left) and the true diagram (right) for azimuth an elevation values of 89.5 and 88.7 degrees with respect to the normal direction, respectively.

MSE goal to measure the RBFNN accuracy was set to 10^{-11}). Hence, for the sake of brevity, for scenario 1 we only highlight the results from the evaluations carried out using the RBFNN approach.

A.2 Globally tunable scenario

For the tunable, single unit cell / full radiation pattern case, the trained MLPNN was able to predict the radiation pattern for any given R and C value with an R^2 test of 0.9849. Therefore, our hypothesis that ML models can accurately predict the radiation pattern of the reflected wave in a single unit cell for each R and C combination, has also been validated. Fig. 6.10 shows the visual comparison between the predicted radiation pattern by the trained MLPNN and the true diagram obtained through EM simulation, for R and C values that were not present in the training set. This reinforces the fact that our predictor can learn and generalize to scenarios with untrained/unseen values of R and C within the training dataset.

Further, here we do not present a discussion of results for this scenario with the RBFNN and CNN setups. Specifically, given that RBFNN is not suitable for the globally tunable scenario, and the CNN performs poorly for the non-tunable scenario, we do not detail a discussion on the performance of these setups here.

B Heterogeneous MS Configuration (Locally tunable scenario)

The radiation pattern *attribute* prediction problem for the locally tunable scenario, is essentially a regression problem. Hence, the cost/error function to minimize during the training process is the MSE. However, this error function does not provide a very good interpretability of the performance. Alternatively, we define a tolerance (or a set of tolerances) specific

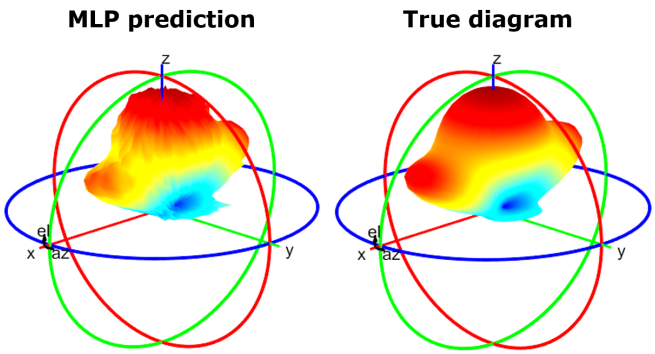

Figure 6.10: Comparison between the predicted radiation pattern by the MLPNN of the Globally tunable scenario (left) and the true diagram (right) for R and C values of 2.5Ω and 0.25 pF, respectively.

for each measure of interest. Subsequently, we evaluate the percentage of the predictions that fall within this tolerance limit. This is termed as the accuracy measure in this chapter. Thus, in the following sections (B.1-B.4) we discuss the performance of the MLPNN and CNN over the different measures of interest that we aim to predict using our methodology (Fig. 4). The results associated with the ensuing discussions are reported in Table 6.5.

B.1 Directivity

For *Directivity*, we observed that the MLPNN provided near-perfect prediction, subject to certain tolerance limits. Concretely, from Table 6.5, it can be seen that 95% of the test samples have been accurately predicted when the tolerance is set to 0.25 dB. Moreover, when the tolerance is relaxed further, i.e., to 0.5 dB, we observe an improved accuracy of 99.99%. However, when the tolerance limit is reduced to 0.1 dB, we notice that the accuracy of the MLPNN degrades drastically to 56.3%.

On the other hand, when the CNN is used as the predictor, the accuracy of prediction with a 0.25 dB tolerance limit is set on 90.6% (Table 6.5). Further, when the tolerance is increased to 0.5 dB, the accuracy of prediction is improved to 99.8%. Additionally, when the tolerance limit is reduced to 0.1 dB, similar to the MLPNN case, the accuracy of prediction for the CNN is deteriorated significantly to 48.8%. These aforementioned accuracy measures are lower than those offered by the MLPNN. This is because, an MLPNN based method, due to the fully connected architecture, can learn almost any feature space accurately. On the other hand, a CNN tries to extract the most significant features through its convolution-based processing and hence, is a lossy method.

However, a point of contention with the MLPNN is that the fully connected architecture

Table 6.5: Accuracy Measure: MLPNN vs CNN

Parameter	**MLPNN**		**CNN**	
	Tolerance	Accuracy	Tolerance	Accuracy
Directivity	0.5 dB	99.9%	0.5dB	99.8%
	0.25 dB	95%	0.25dB	90.6%
	0.1 dB	56.3%	0.1dB	48.8%
Side-Lobe Level	0.5 dB	99.9%	0.5dB	99.4%
	0.25 dB	98.3%	0.25dB	94.3%
	0.1 dB	86.1%	0.1dB	80.1%
Reflection Angle	5°	99.8%	5°	98.9%
	2°	72.7%	2°	60.7%
	1°	40.6%	1°	31.9%
Half Power Beam Width	1°	99.5%	1°	98.8%
	0.5°	97.3%	0.5°	92.6%
	0.25°	79.2%	0.25°	61.8%

is not scalable for bigger MS configurations. This will progressively become detrimental to the system performance, as the cost of computation will increase exponentially. In contrast, a CNN utilizes significantly less computational and memory resources and will scale better, whilst providing an accuracy measure that is close to that offered by the MLPNN.

B.2 Side-Lobe Level

For the *SLL*, we obtain similar observations from Table 6.5, as we did for the *Directivity* parameter. Specifically, for the MLPNN, when we vary the tolerance from 0.5 dB to 0.25 dB and finally to 0.1 dB, the corresponding accuracy measures are registered at 99.9%, 98.3%, and 86.1%, respectively. On the other hand, for the same tolerance value ensemble, the CNN method produces accuracy measures of 99.4%, 94.3%, and 80.1%, respectively.

And so, as we can see that the MLPNN performs slightly better than the CNN. However, as mentioned earlier, this comes at a significant computational cost, thus hampering its scalability. Besides, it is understood that the correlation between the neighboring unit cells is far less as compared to those that are found in images in general [139]. Consequently, this corroborates the findings from Table 6.5, with regards to the CNN performing slightly worse as compared to the MLPNN. Concretely, an MLPNN can learn the interactions between

the distinctly related neighboring unit cells much more effectively due to the fully connected architecture. However, a CNN treats the MS like an image, thus considering the neighboring unit cells to be correlated. However, in reality, this is seldom the case.

It is imperative to state here that, the aforesaid non-relational nature of nearby unit cells is also responsible for the visibly subdued performance of the CNN, as compared to the MLPNN, for other measures of interest.

B.3 Reflection Angle

The results for the angle of maximum radiation in Table 6.5 are obtained bBeay averaging the accuracy of prediction of the elevation and azimuth angles, to provide a single view over this feature. Subsequently, we observe that the MLPNN performs slightly better than the CNN, the reasons for which have been expressed in Section B.2.

To elaborate, for this measure we consider tolerance values of 5^{o}, 2^{o}, and 1^{o}. Next, from Table 6.5 we observe that the MLPNN has an accuracy of 99.8%, 72.7%, and 40.6% for the corresponding tolerance values, respectively. Further, the CNN approach has an accuracy of 98.9%, 60.7%, and 31.9%, given the same tolerance value ensemble, respectively. As can be seen, the accuracy drops as we reduce the tolerance limit, which is in line with our observations from the other measures of interest. Additionally, it can be deduced that irrespective of the NN utilized for the prediction step, the accuracy for the lower tolerance values is significantly less as compared to the other measures of interest.

B.4 Half Power Beam Width

For this measure, we consider the tolerance values of 1^{o}, 0.5^{o}, and 0.25^{o}. From Table 6.5 we observe that the MLPNN has the corresponding accuracy of 99.5%, 97.3%, and 79.2%, respectively. Further, the CNN has accuracy measures of 98.8%, 92.6%, and 61.8%, respectively. The trend for the accuracy values is similar to that observed for the other measures of interest (Sections B.1-B.3).

Hence, from the discussions so far, we can deduce that the proposed methodology can accurately predict the reflected beam radiation pattern or the measures that can fully characterize the same. To further reinforce this idea, we present Figs. 6.11 and 6.12. Concretely, Fig. 6.11 shows in detail the evolution of the accuracy of the predictions for the *Directivity* and *SLL* as the tolerance in dB grows, for both MLPNN and CNN cases. We observe that the trend for the accuracy is exactly what we have deduced through our discussions in sections B.1-B.4. Further, we see that as the tolerance approaches 0.5 dB, the accuracy of the CNN predictor approaches that of the MLPNN.

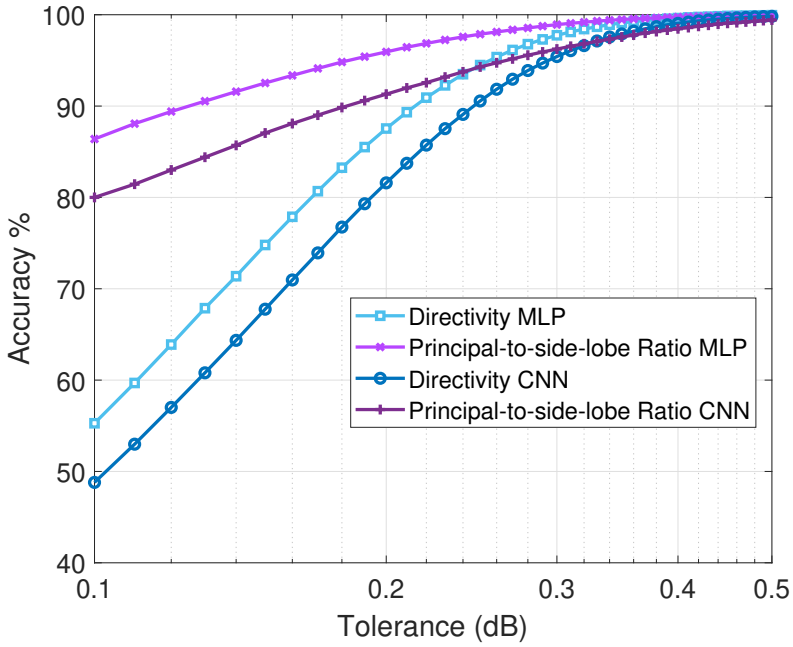

Figure 6.11: Accuracy vs tolerance in dB for both MLPNN and CNN. The curves shown correspond to *Directivity* and SLL.

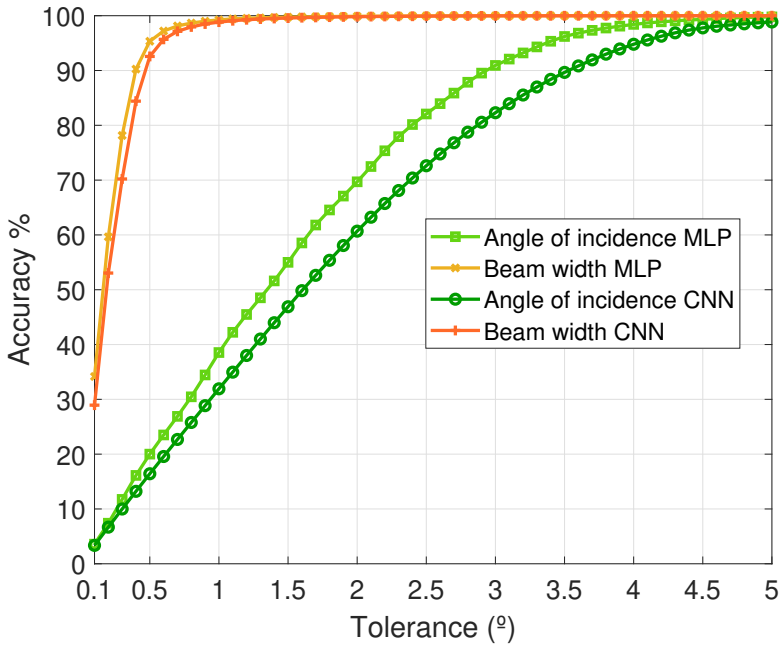

Figure 6.12: Accuracy vs tolerance in degrees for both MLPNN and CNN. The curves shown correspond to the RA and $HPBW$.

Lastly, Fig. 6.12 illustrates the evolution of the accuracy of the predictions for the *Angle of incidence* and *HPBW* as the tolerance in degrees grows, for both MLPNN and CNN cases. Again, here we observe that the accuracy percentage improves as the tolerance is increased. However, we also notice that the *HPBW* prediction approaches near 100% accuracy at very low tolerance values, whilst the *RA* measure necessitates higher tolerance limits for the predictors to achieve better accuracy.

6.5 Summary

We presented a data-driven methodology, wherein we developed an NN-based approach for characterizing the reflected beam radiation pattern from an MS. One of the most important advantages of such an approach is that, while its accuracy is close to the full-wave simulation, the time complexity to achieve the same is significantly smaller. Additionally, it can also serve as a methodology that enables self-healing characteristics and facilitates maintenance aspects of MSs in the 6G wireless network environment.

As part of this methodology, we have provisioned an incremental design framework. Through this framework, we analyzed three specific scenarios, wherein we estimated radiation pattern of non-tunable MSs and globally tunable MSs. Further, through our analysis, we have demonstrated the efficacy of the NN-based approaches. Concretely, it was observed that the NN-based approaches could predict the radiation pattern with very high accuracy in a significantly reduced time frame as compared to the full-wave simulator counterparts.

Moreover, through the locally tunable scenario, we demonstrated that our CNN-based prediction framework performs as well as the fully connected MLPNN framework. However, it does so with a significantly reduced computational complexity as compared to the fully connected MLPNN framework. This will especially be critical when the framework is scaled up to even larger MS.

Further, through the last scenario, we have provisioned the first study, wherein, instead of estimating the entire radiation pattern, we have predicted the most important parameters that govern any radiation pattern, i.e., *Directivity*, SLL, RA and $HPBW$. This process will not only ensure the required reliability in estimation but it will also allow for a faster convergence time for such estimations.

Since the objective of this chapter was to understand the feasibility of the discussed approaches, only a simulation-based analysis was performed. Hence, as part of future work, a more realistic framework based on true data (measurement) should be carried out.

Chapter 7

Conclusions

In this thesis, we developed a methodology to model EM characteristics of the MS. After analyzing the performance metrics versus scaling and manufacturing factors, design-oriented guidelines are introduced. Conventional beam steering metrics are evaluated as functions of the unit cell size, number of unit cell states, and metasurface size for different incidence and reflection angles. It is shown that metasurfaces $5\lambda \times 5\lambda$ or larger with unit cells of $\lambda/3$ and 2-bits coding ensure good performance overall. Further, it is demonstrated that performance degrades significantly for angles larger than $\theta > 60^o$ and that, to combat this, extra effort is needed in the development of the unit cell. These performance trends, combined with power and cost models, paves the way for optimal metasurface dimensioning.

We examined the reliability problem in programmable MS by proposing an error model and a general methodology for error analysis. To derive the error model, the causes and potential impact of faults are identified and discussed qualitatively. Results show that performance degradation depends on the type of error and its spatial distribution and that, in beam steering, error rates over 20% can still be considered acceptable.

We analyzed the performance of multi-user RIS for indoor and outdoor scenarios, given broadcast mode of operation. The aforesaid scenarios encompass a majority of the challenging scenarios that wireless networks encounter. We show that our proposed technique for multi-beam engineering provisions sufficient gains in the observed channel capacity when the users are close to the MS in the indoor office environment scenario. Further, we report a 1-2 orders of magnitude increase in the system throughput given the outdoor environment. The results prove that RIS with the ability to communicate with multiple users can empower wireless networks with great capacity.

Finally, we proposed an NN-based approach that enables a fast and accurate characterization of the MS response. We analyze multiple scenarios and demonstrate the capabilities and

utility of the proposed methodology. Concretely, we show that this method can learn and predict the parameters governing the reflected wave radiation pattern with an accuracy of a full-wave simulation (98.8%–99.8%) and the time and computational complexity of an analytical model. The aforementioned result and methodology will be of specific importance for the design, fault tolerance, and maintenance of the thousands of RISs that will be deployed in the 6G network environment.

Appendix: Workload Characterization and Traffic Analysis

Introduction

The HSF paradigm embeds a network of customized integrated circuit (IC) controllers within the device with the aim of adding intelligence, connectivity, and autonomy. Here, we briefly characterize the workload of programmable MS which is then used to analyze the beam steering HSFs. The workload characterization leads to many useful insights into traffic behavior, including the spatio-temporal load incurred and the HSF limitations in terms of fine-grained tracking of moving targets. Similar to previous analysis, we need a model to study the HSF workload characterization.

HSF Model

Fig. 7.1 illustrates the HSF under study, which is composed by a bidimensional array of $M \times N$ unit cells attached to a gateway device that interfaces the HSF tile with other tiles or with the world. The HSF design [1], incorporates a Digital-to-Analog with 8 bits to set the voltage levels for configuring the complex impedance values thus offering a wide range of phase shift [167]. The aim of the HSF is to react to variations in the position of the source or the destination to maximize the amount of signal that reaches the receiving end.

Without loss of generality, let us consider a HSF that is fixed onto a wall and is used to track the position of users or objects moving along a vector $\vec{v}$. This could model, for instance, a scenario where the objective is to avoid service disruption in wireless 5G networks with highly-directive antennas [16]. The position of the moving objects can be expressed in spherical coordinates using the HSF as point of reference, thus allowing to obtain the desired reflection angle over time. The trajectories under study are illustrated in Fig. 7.1b and described next.

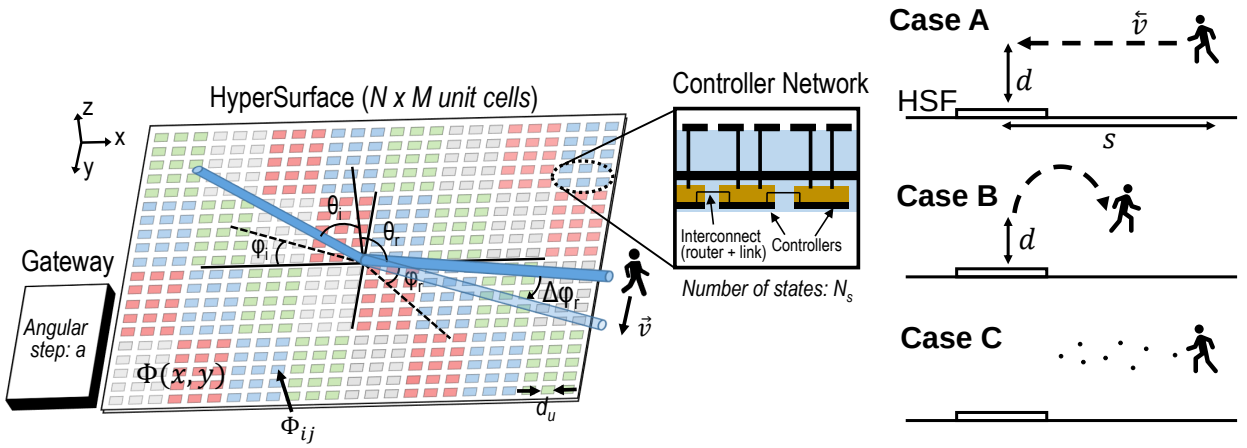

(a) System model (b) Mobility cases (top view)

Figure 7.1: System model. Target moves with speed $\vec{v}$ changing the required reflection angle. A HSF with $N \times M$ unit cells of size d_u implements a phase profile $\Phi(x, y)$ to obtain the desired reflected angle. The phase of each unit cell Φ_{ij} is approximated to the closest phase among the N_s available states. The gateway reconfigures Φ_{ij} when angles vary more than the angular step a, which is a design parameter.

Case A: the target moves in a straight line parallel to the surface. We assume that the target is at the same height as the surface, i.e. $\phi_i = \phi_r = 0°$. Motion starts from a point at distance S from the surface and finishes when the object is directly in front of it. The perpendicular distance between the surface and the line of motion is denoted by d as shown in the figure. To emulate the walking movement of mobile user, we consider a default speed of $v = 1.4m/s$, which is the average walking speed of humans. Therefore, the azimuth angle of the reflection signal, θ, at time t is then expressed as

$$\theta = \arctan(\frac{S - vt}{d}) \tag{7.1}$$

Case B: the target describes a projectile motion parallel to the surface starting from a point close to the surface and moving away from it, as represented in Fig. 7.2. This could represent a typical case of radar tracking. Unlike the horizontal movement described above, the projectile motion changes both the azimuth and elevation angles of the reflected signal. The initial speed is assumed to be $v_i = 30m/s$. Considering a gravitational acceleration constant $g = 9.8m/s^2$, the azimuth and elevation angles of the reflected signal at time t are expressed as follows.

$$\theta = \arctan(\frac{\frac{v_i}{\sqrt{2}}t}{d}) \tag{7.2}$$

$$\phi = \arctan\left(\frac{v_i}{\sqrt{2}t} - 0.5gt^2\right) \tag{7.3}$$

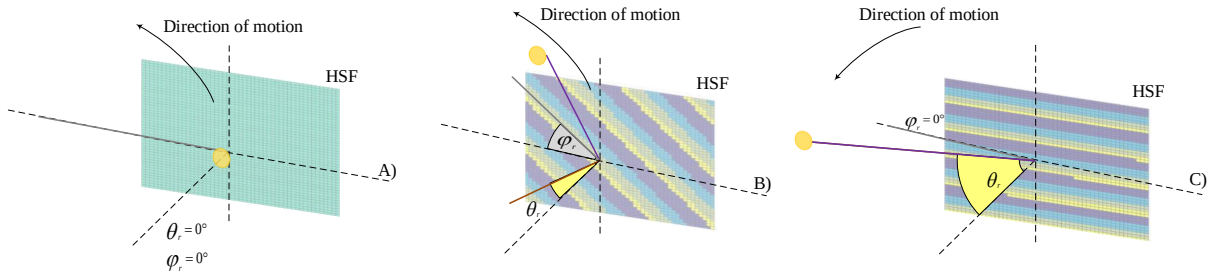

Figure 7.2: Illustration of tracking in Case B, which models a projectile movement parallel to the HSF.

Case C: the target takes arbitrary leaps which results into abrupt changes in location as apposed to the gradual change in the aforementioned cases. This case represents a person moving in an area with multiple mobile obstacles resulting in intermittent connection with the surface. Using the same settings of Case A, we model the arbitrary movement by randomly changing the azimuth angle of the reflected signal.

For the purposes of traffic analysis, we consider that the HSF is equipped with two gateways. The input gateway is in charge of gathering the changes in incidence and reflection angles and reprogramming the HSF in order to adapt to those changes. Whenever any of the angles changes by more than a given pre-defined amount, which we define as *angular step* α, the gateway computes the new state for each unit cell. To save power, the gateway communicates only to the unit cells that need to change the state.

The gateway (i) has external sensing or communication capabilities that allow to infer the angle of incidence $\{\theta_i, \phi_i\}$, (ii) communicates with other external devices to obtain the target direction $\{\theta_r, \phi_r\}$, and (iii) is thus able to compute the phase profile Φ_{ij} towards obtaining the state of each unit cell. An additional Gateway is provided which collects acknowledgments (ACKs) for successfully delivered setup packets.

We consider an HSF design where each controller drives a single unit cell. The controllers are interconnected among them and to the gateway via an internal network, with two purposes: (a) for the gateway to send the reconfiguration requests to the controllers, and (b) for the controllers to send acknowledgment packets to the gateway.

In order to model how fast does the HSF serve the signaling between the gateway and the controllers, it is necessary to model the chip interconnections. The design of the HSF assumes a wired controller network resembling a Network-on-Chip [13]. The design of the topology of this network has been subject to multiple implementation restrictions and requirements to minimize cost and power, as pointed out in [167]. Due to these restrictions, a Manhattan-like topology is considered. Fig. 7.3 shows a 4×4 sized network, extendable to any number of

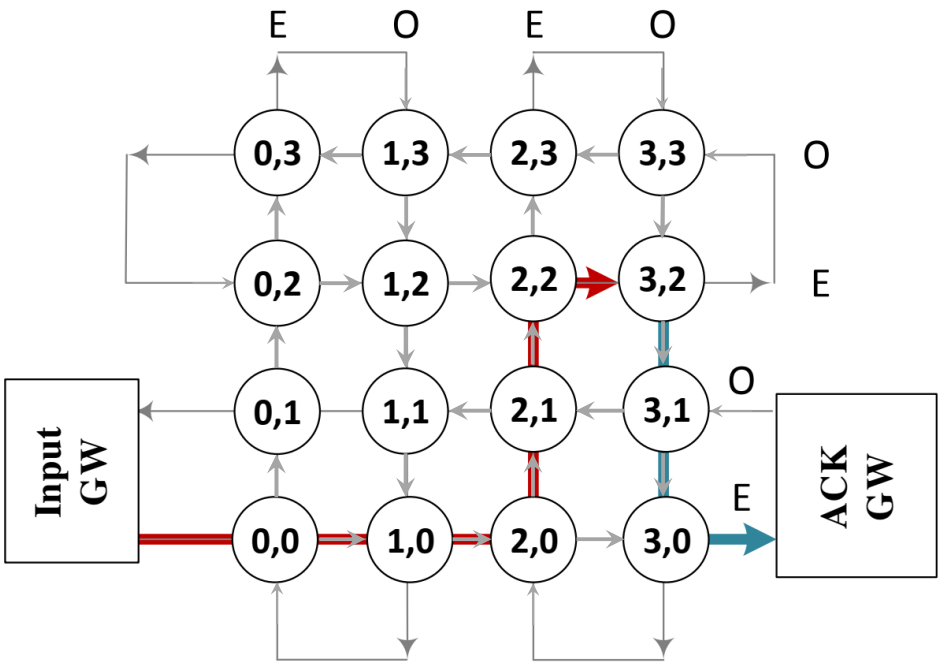

Figure 7.3: Embedded controller network topology and an example routing path to the destination node at coordinates (3,2). Rows and columns of even and odd coordinates are denoted by E and O, respectively.

controllers. One of the main characteristics of this topology is its unidirectional channels, which significantly limits routing options within the network [81, 168]. Therefore, a simple variation of the XY-YX routing mechanism, referred to as the agnostic XY-YX, has been selected to disseminate directives within the controller network with enhancements recently proposed to ensure deadlock freedom in the presence of faults [168].

Agnostic XY-YX is a topology-aware variation of the XY-YX that alternates between forwarding the packet horizontally and vertically until the destination is reached. As shown in Fig. 7.3, rows of even coordinates can forward packets towards the east whereas rows of odd coordinates forward packets towards the west. Similarly, columns of even coordinates forward packets towards the north and those of odd coordinates forward packets towards the south. The locations of the input gateway and the ACK gateway, which are at the bottom left corner and the bottom right corner of the network, respectively, suggest that configuration and data packets generally move from the east to the west of the network.

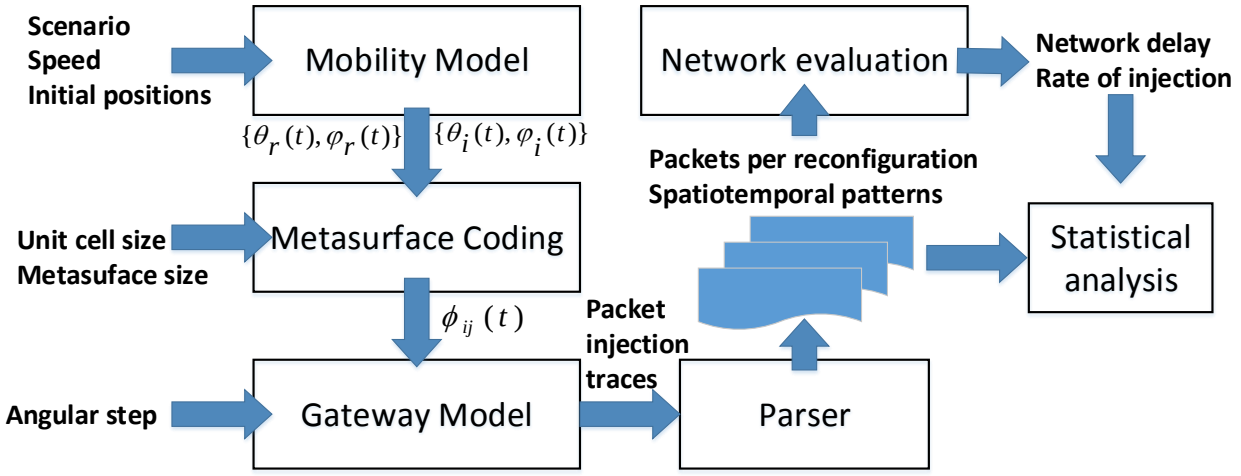

Figure 7.4: Summary of the evaluation methodology.

Methodology

We first evaluate the incidence and reflection angles given the positions of the HSF, the illumination source, and the moving target. Then, we use Eq. (2.1) to obtain the phase gradients and then Eq. (2.2) to calculate the phase Φ_{ij} of each unit cell. Finally, we apply the nearest neighbor mapping to Φ_{ij}.

The main output is a packet injection trace for each simulated scenario. Besides studying the impact of the user mobility on the internal communication, we also examine the impact of two HSF design parameters: the number of states per unit cell N_s and the angular step α. The traces are finally fed to an AnyLogic-based custom-made simulator [81], which evaluates the time consumed by the controllers network to deliver reconfiguration packets to the corresponding controllers. The input gateway is assumed to be connected at the bottom left corner, i.e. node (0, 0), and the ACK gateway to be connected at the bottom right corner, i.e. node $(N-1, 0)$. Further, each data packet triggers the generation of an ACK packet upon receipt at the destination node. The delay of the network (to deliver packets relative to one reconfiguration of the HSF) is the time elapsed between the first data packet entering the network and the last ACK packet is received by the ACK gateway. The obtained reconfiguration delays, along with the information of the spatial distribution of packets, are finally utilized to characterize the patterns of the traffic within the network in terms of packet arrival times at the nodes. Statistical analysis is then performed on these patterns to define the appropriate models for the generated traffic.

As shown in Fig. 7.4, the parser results are used to analyze the spatio-temporal charac-

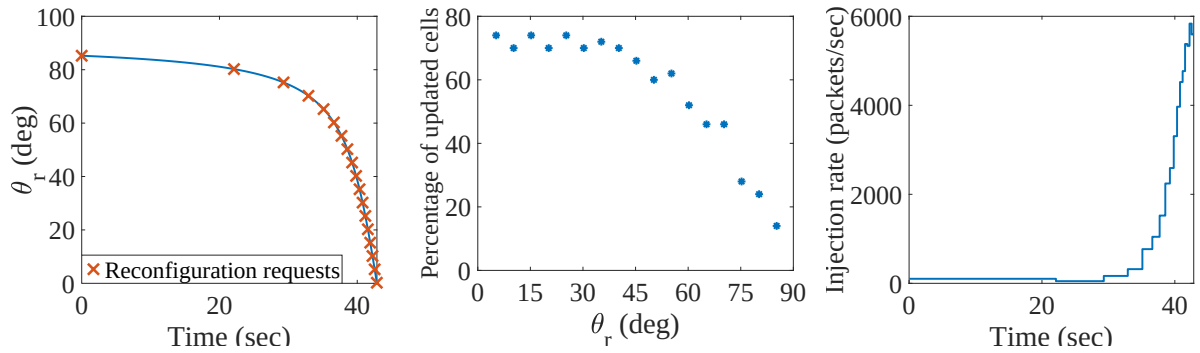

(a) Reconfiguration request (b) Reconfiguration ratio (c) Reconfiguration per second

Figure 7.5: For an object moving according to Case A: (a) Reconfiguration requests during the tracking of the object. (b) Percentage of reconfigured cells versus the azimuth angle of the reflected signal. (c) The number of reconfiguration requests per second.

teristics of the network traffic. Then, we examine the effect of varying the parameters of the surface on the traffic generated by the different motion scenarios and the network delay. We further extend the analysis by calculating the tolerance of the HSF, this is, the type and speed of movements that the HSF is capable of serving correctly. Finally, the traffic generated through a representative scenario is analyzed.

Results

In all the cases, the HSF has $N \times M = 50 \times 50$ unit cells, with $N_s = 4$ possible states and an angular step of $\alpha = 5°$. The relationship between the change in the reflection angle (the incidence angle is assumed to be fixed) and the reconfiguration requests injected into the system is depicted in Fig. 7.5a where Case A motion pattern is considered. The figure shows that reconfiguration requests (marked by crosses) become more frequent as the tracked object approaches the surface. For instance, more than 80% of the requests are injected during the last 33% of the motion time span. The size of the updated subset highly relies on the preceding and the currently targeted angles, as shown in Fig. 7.5b. For instance, a change of 5° from $\theta_r = 85°$ to $\theta_r = 80°$ requires the reconfiguration of about 20% of the cells of the surface. Whereas the same amount of change in the angle between $\theta_r = 35°$ and $\theta_r = 30°$ requires the reconfiguration of about 70% of the cells.

As expected, the injection rate increases as the change in the reflection angle becomes more frequent as observed in Fig. 7.5c. We investigate the spatial distribution of traffic generated by the different mobility cases. This is visualized through heat maps representing the HSF, where hotter spots indicate cells receiving larger number of packets throughout the

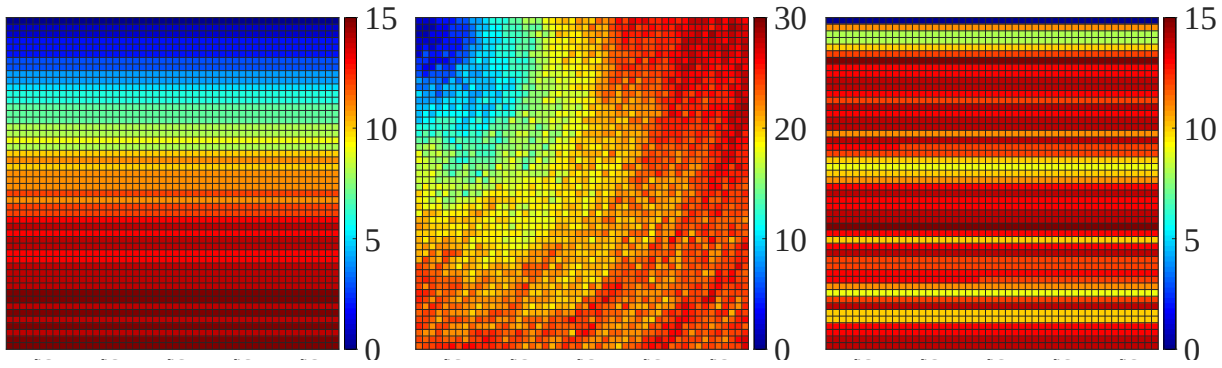

(a) Case A (b) Case B (c) Case C

Figure 7.6: Spatial distribution of traffic for the three considered movement scenarios.

considered motion. The effect of the different motion patterns is shown in Fig. 7.6, where the gradual change in θ_r induced from tracking an object following Case A results in the spatial distribution in Fig. 7.6a. On the other hand, the traffic is more evenly distributed throughout the network when the motion of Case C is considered as observed in Fig. 7.6c. In the two aforementioned cases, the elevation angle was fixed, which is different than the projectile motion case where both the azimuth and elevation angles of the reflected signal change. The effect of this can be observed in the pattern of the heat map in Fig. 7.6b.

Here we determine the frequency with which each node must be reconfigured in a particular range of motion and the states obtained at each reconfiguration. Feeding this information into our custom-made AnyLogic-based network simulator produces detailed paths for all the packets injected into the network. At each node, we obtain the number of received packets and the time of receipt. The information about the state of each node at every reconfiguration is utilized to study the spatial correlation between nodes in terms of the obtained state. The number of received packets however, is used to characterize the load at each node in the network. The state of each node is compared with the state of all other nodes in the network at each reconfiguration. We visualize this spatial correlation through heat maps where each color in the map represents a cluster of nodes which have a high probability ($p > 0.7$) of obtaining the same state during the entire range of motion.

Fig. 7.7 shows the heat maps corresponding to the considered mobility models, namely, horizontal movement (case A), projectile movement (case B) and random movement (case C). Fig. 7.7a indicates that, in Case A, a large portion of the nodes have a high probability of having the same state and thus the small number of color variations in the color scale. Furthermore, the states are distributed on the rows of the network such that cells on the same row have a high probability of acquiring the same state. This is different than what is

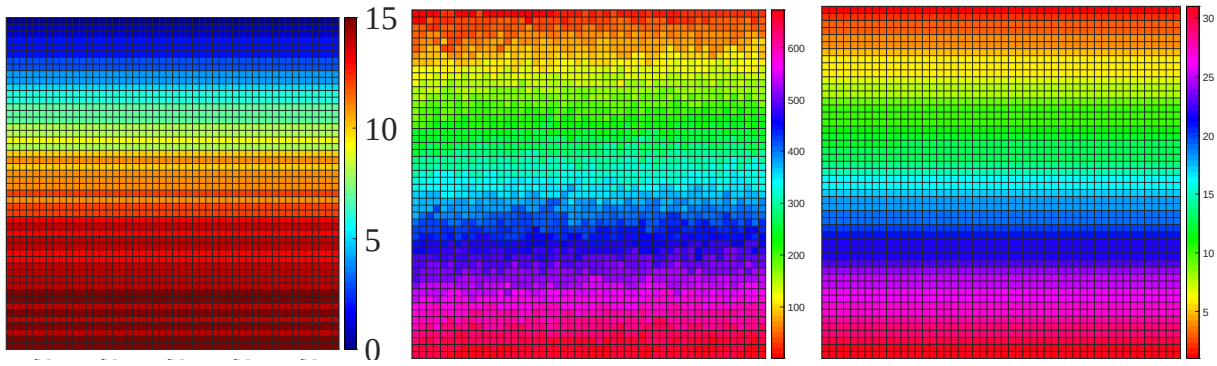

(a) Case A (b) Case B (c) Case C

Figure 7.7: Spatial correlation in cell states for the three considered mobility scenarios.

observed in Fig. 7.7b and Fig. 7.7c where a smaller portion of the nodes frequently obtain the same state, which is indicated by the higher number of colors in the heat map (i.e. each color represents a cluster of nodes that probably have a similar state).

Bibliography

[1] Visorsurf. [Online]. Available: http://www.visorsurf.eu/

[2] H. Taghvaee, A. Cabellos-Aparicio, J. Georgiou, and S. Abadal, "Error analysis of programmable metasurfaces for beam steering," *IEEE Journal on Emerging and Selected Topics in Circuits and Systems*, vol. 10, no. 1, pp. 62–74, 2020.

[3] I. F. Akyildiz, S. Nie, S.-C. Lin, and M. Chandrasekaran, "5G roadmap: 10 key enabling technologies," *Computer Networks*, vol. 106, pp. 17–48, 2016.

[4] E. Björnson, E. G. Larsson, and T. L. Marzetta, "Massive mimo: Ten myths and one critical question," *IEEE Communications Magazine*, vol. 54, no. 2, pp. 114–123, 2016.

[5] T. S. Rappaport, S. Sun, R. Mayzus, H. Zhao, Y. Azar, K. Wang, G. N. Wong, J. K. Schulz, M. Samimi, and F. Gutierrez, "Millimeter wave mobile communications for 5G cellular: It will work!" *IEEE access*, vol. 1, pp. 335–349, 2013.

[6] H. Farhady, H. Lee, and A. Nakao, "Software-defined networking: A survey," *Computer Networks*, vol. 81, pp. 79–95, 2015.

[7] E. Björnson, L. Sanguinetti, H. Wymeersch, J. Hoydis, and T. L. Marzetta, "Massive mimo is a reality—what is next?: Five promising research directions for antenna arrays," *Digital Signal Processing*, vol. 94, pp. 3–20, 2019.

[8] S. J. Nawaz, S. K. Sharma, S. Wyne, M. N. Patwary, and M. Asaduzzaman, "Quantum Machine Learning for 6G Communication Networks: State-of-the-Art and Vision for the Future," *IEEE Access*, vol. 7, pp. 46 317–46 350, 2019.

[9] C. Liaskos, A. Tsioliaridou, A. Pitsillides, S. Ioannidis, and I. Akyildiz, "Using any Surface to Realize a New Paradigm for Wireless Communications," *Communications of the ACM*, vol. 61, no. 11, pp. 30–33, 2018.

[10] S. Nie, J. M. Jornet, and I. F. Akyildiz, "Intelligent environments based on ultra-massive mimo platforms for wireless communication in millimeter wave and terahertz bands," in *Proceedings of the ICASSP '19*. IEEE, 2019, pp. 7849–7853.

[11] V. Petrov, D. Moltchanov, J. M. Jornet, and Y. Koucheryavy, "Exploiting Multipath Terahertz Communications for Physical Layer Security in Beyond 5G Networks," in *Proceedings of the INFOCOM Workshops '19*. IEEE, 2019, pp. 865–872.

[12] A. Mestres, A. Rodriguez-Natal, J. Carner, P. Barlet-Ros, E. Alarcón, M. Solé, V. Muntés-Mulero, D. Meyer, S. Barkai, M. J. Hibbett *et al.*, "Knowledge-defined networking," *ACM SIGCOMM Computer Communication Review*, vol. 47, no. 3, pp. 2–10, 2017.

[13] S. Abadal, C. Liaskos, A. Tsioliaridou, S. Ioannidis, A. Pitsillides, J. Solé-Pareta, E. Alarcón, and A. Cabellos-Aparicio, "Computing and Communications for the Software-Defined Metamaterial Paradigm: A Context Analysis," *IEEE Access*, vol. 5, pp. 6225–6235, 2017.

[14] C. Liaskos, A. Tsioliaridou, A. Pitsillides, I. F. Akyildiz, N. Kantartzis, A. Lalas, X. Dimitropoulos, S. Ioannidis, M. Kafesaki, and C. Soukoulis, "Design and development of software defined metamaterials for nanonetworks," *IEEE Circuits and Systems Magazine*, vol. 15, no. 4, pp. 12–25, 2015.

[15] A. Pitilakis, A. C. Tasolamprou, C. Liaskos, F. Liu, O. Tsilipakos, X. Wang, M. S. Mirmoosa, K. Kossifos, J. Georgiou, A. Pitsilides, N. Kantartzis, S. Ioannidis, E. N. Economou, M. Kafesaki, S. A. Tretyakov, and C. M. Soukoulis, "Software-defined metasurface paradigm: Concept, challenges, prospects," in *Proceedings of the META-MATERIALS '18*. IEEE, Aug. 2018.

[16] C. Liaskos, S. Nie, A. Tsioliaridou, A. Pitsillides, S. Ioannidis, and I. Akyildiz, "A New Wireless Communication Paradigm through Software-Controlled Metasurfaces," *IEEE Communications Magazine*, vol. 56, no. 9, pp. 162–169, 2018.

[17] M. Di Renzo, M. Debbah, D.-T. Phan-Huy, A. Zappone, M.-S. Alouini, C. Yuen, V. Sciancalepore, G. C. Alexandropoulos, J. Hoydis, H. Gacanin *et al.*, "Smart radio environments empowered by reconfigurable ai meta-surfaces: an idea whose time has come," *EURASIP Journal on Wireless Communications and Networking*, no. 129, 2019.

[18] M. Di Renzo and J. Song, "Reflection probability in wireless networks with metasurface-coated environmental objects: an approach based on random spatial processes," *EURASIP Journal on Wireless Communications and Networking*, no. 99, 2019.

[19] X. Tan, Z. Sun, D. Koutsonikolas, and J. M. Jornet, "Enabling indoor mobile millimeter-wave networks based on smart reflect-arrays," in *Proceedings of the INFOCOM '18*. IEEE, 2018, pp. 270–278.

[20] C. Huang, A. Zappone, G. C. Alexandropoulos, M. Debbah, and C. Yuen, "Reconfigurable intelligent surfaces for energy efficiency in wireless communication," *IEEE Transactions on Wireless Communications*, vol. 18, no. 8, pp. 4157–4170, 2019.

[21] W. Tang, X. Li, J. Y. Dai, S. Jin, Y. Zeng, Q. Cheng, and T. J. Cui, "Wireless communications with programmable metasurface: Transceiver design and experimental results," *China Communications*, vol. 16, no. 5, pp. 46–61, 2019.

[22] J. Y. Dai, W. K. Tang, J. Zhao, X. Li, Q. Cheng, J. C. Ke, M. Z. Chen, S. Jin, and T. J. Cui, "Wireless communications through a simplified architecture based on time-domain digital coding metasurface," *Advanced Materials Technologies*, p. 1900044, 2019.

[23] V. Arun and H. Balakrishnan, "Rfocus: Practical beamforming for small devices," *arXiv preprint arXiv:1905.05130*, 2019.

[24] B. A. Munk, *Frequency Selective Surfaces: Theory and Design*. New York: John Wiley & Sons, 2000.

[25] S. B. Glybovski, S. A. Tretyakov, P. A. Belov, Y. S. Kivshar, and C. R. Simovski, "Metasurfaces: From microwaves to visible," *Physics Reports*, vol. 634, pp. 1–72, 2016.

[26] C. L. Holloway, E. F. Kuester, J. A. Gordon, J. O'Hara, J. Booth, and D. R. Smith, "An overview of the theory and applications of metasurfaces: The two-dimensional equivalents of metamaterials," *IEEE Antennas and Propagation Magazine*, vol. 54, no. 2, pp. 10–35, April 2012.

[27] T. Koschny, C. Soukoulis, and M. Wegener, "Metamaterials in microwaves, optics, mechanics, thermodynamics, and transport," *J. Opt.*, vol. 19, no. 8, 2017.

[28] H. Yang, X. Cao, F. Yang, J. Gao, S. Xu, and M. Li, "A programmable metasurface with dynamic polarization , scattering and focusing control," *Scientific Reports*, no. October, pp. 1–11, 2016.

[29] A. Tasolamprou, L. Zhang, M. Kafesaki, T. Koschny, and C. Soukoulis, "Experimentally excellent beaming in a two-layer dielectric structure," *Opt. Express*, vol. 22, no. 19, pp. 23 147–23 152, 2014.

[30] L. Li, T.-J. Cui, W. Ji, S. Liu, J. Ding, X. Wan, Y. Bo Li, M. Jiang, C. W. Qiu, and S. Zhang, "Electromagnetic reprogrammable coding-metasurface holograms," *Nature Communications*, vol. 8, no. 1, pp. 1–7, 2017.

[31] S. Tcvetkova, D.-H. Kwon, A. Díaz-Rubio, and S. Tretyakov, "Near-perfect conversion of a propagating plane wave into a surface wave using metasurfaces," *Phys. Rev. B*, vol. 97, no. 11, 2018.

[32] O. Tsilipakos, A. C. Tasolamprou, T. Koschny, M. Kafesaki, E. N. Economou, and C. M. Soukoulis, "Pairing toroidal and magnetic dipole resonances in elliptic dielectric rod metasurfaces for reconfigurable wavefront manipulation in reflection," *Adv. Opt. Mater.*, vol. 6, no. 22, p. 1800633, 2018.

[33] X. Wang, A. Díaz-Rubio, V. Asadchy, G. Ptitcyn, A. Generalov, J. Ala-Laurinaho, and S. Tretyakov, "Extreme asymmetry in metasurfaces via evanescent fields engineering: Angular-asymmetric absorption," *Phys Rev Lett*, vol. 121, no. 25, 2018.

[34] S. W. Qu, W. W. Wu, B. J. Chen, H. Yi, X. Bai, K. B. Ng, and C. H. Chan, "Controlling Dispersion Characteristics of Terahertz Metasurface," *Scientific Reports*, vol. 5, p. 9367, 2015.

[35] Y. Zhang, L. Liang, J. Yang, Y. Feng, B. Zhu, T. Zhao, J. Jiang, B. Jin, and W. Liu, "Broadband diffuse terahertz wave scattering by flexible metasurface with randomized phase distribution," *Scientific Reports*, vol. 6, p. 26875, 2016.

[36] S. Liu, T. J. Cui, Q. Xu, D. Bao, L. Du, X. Wan, W. X. Tang, C. Ouyang, X. Y. Zhou, H. Yuan, H. F. Ma, W. X. Jiang, J. Han, W. Zhang, and Q. Cheng, "Anisotropic coding metamaterials and their powerful manipulation of differently polarized terahertz waves," *Light: Science and Applications*, vol. 5, no. 5, pp. e16 076–11, 2016.

[37] G. Perrakis, O. Tsilipakos, G. Kenanakis, M. Kafesaki, C. M. Soukoulis, and E. N. Economou, "Perfect optical absorption with nanostructured metal films: design and experimental demonstration," *Opt. Express*, vol. 27, no. 5, pp. 6842–6850, Mar. 2019.

[38] S. E. Hosseininejad, K. Rouhi, M. Neshat, A. Cabellos-Aparicio, S. Abadal, and E. Alarcón, "Digital Metasurface Based on Graphene: An Application to Beam Steer-

ing in Terahertz Plasmonic Antennas," *IEEE Transactions on Nanotechnology*, vol. 18, no. 1, pp. 734–746, 2019.

[39] N. Yu, P. Genevet, M. a. Kats, F. Aieta, J.-P. Tetienne, F. Capasso, and Z. Gaburro, "Light Propagation with Phase Discontinuities: Generalized Laws of Reflection and Refraction," *Science*, vol. 334, no. October, pp. 333–337, 2011.

[40] C. Pfeiffer and A. Grbic, "Metamaterial Huygens' surfaces: Tailoring wave fronts with reflectionless sheets," *Phys. Rev. Lett.*, vol. 110, p. 197401, May 2013.

[41] F. Liu, O. Tsilipakos, A. Pitilakis, A. C. Tasolamprou, M. S. Mirmoosa, N. V. Kantartzis, D.-H. Kwon, J. Georgiou, K. Kossifos, M. A. Antoniades, M. Kafesaki, C. M. Soukoulis, and S. A. Tretyakov, "Intelligent metasurfaces with continuously tunable local surface impedance for multiple reconfigurable functions," *Phys. Rev. Appl.*, vol. 11, no. 04, p. 044024, 2019.

[42] G. Oliveri, D. Werner, and A. Massa, "Reconfigurable electromagnetics through metamaterials - A Review," *Proceedings of the IEEE*, vol. 103, no. 7, pp. 1034 – 1056, 2015.

[43] S. Makarov, A. Zalogina, M. Tajik, D. Zuev, M. Rybin, A. Kuchmizhak, S. Juodkazis, and Y. Kivshar, "Light-induced tuning and reconfiguration of nanophotonic structures," *Laser Photon. Rev.*, vol. 11, no. 5, 2017.

[44] F. Liu, A. Pitilakis, M. S. Mirmoosa, O. Tsilipakos, X. Wang, A. C. Tasolamprou, S. Abadal, A. Cabellos-Aparicio, E. Alarcón, C. Liaskos, N. V. Kantartzis, M. Kafesaki, E. N. Economou, C. M. Soukoulis, and S. Tretyakov, "Programmable Metasurfaces: State of the art and Prospects," in *Proceedings of the ISCAS '18*, 2018.

[45] T. Cui, B. Bai, and H.-B. Sun, "Tunable metasurfaces based on active materials," *Adv. Funct. Mater.*, vol. 29, no. 10, 2019.

[46] S. Abadal, T.-J. Cui, T. Low, and J. Georgiou, "Programmable metamaterials for software-defined electromagnetic control: Circuits, systems, and architectures," *IEEE Journal on Emerging and Selected Topics in Circuits and Systems*, vol. 10, no. 1, pp. 6–19, 2020.

[47] S. J. Li, X. Y. Cao, L. M. Xu, L. J. Zhou, H. H. Yang, J. F. Han, Z. Zhang, D. Zhang, X. Liu, C. Zhang, Y. J. Zheng, and Y. Zhao, "Ultra-broadband Reflective Metamaterial with RCS Reduction based on Polarization Convertor, Information Entropy Theory

and Genetic Optimization Algorithm," *Scientific Reports*, vol. 5, no. October, pp. 1–12, 2016.

[48] S. Sui, H. Ma, J. Wang, Y. Pang, M. Feng, Z. Xu, and S. Qu, "Absorptive coding metasurface for further radar cross section reduction," *Journal of Physics D: Applied Physics*, vol. 51, no. 6, 2018.

[49] D. S. Dong, J. Yang, Q. Cheng, J. Zhao, L. H. Gao, S. J. Ma, S. Liu, H. B. Chen, Q. He, W. W. Liu, Z. Fang, L. Zhou, and T. J. Cui, "Terahertz Broadband Low-Reflection Metasurface by Controlling Phase Distributions," *Advanced Optical Materials*, vol. 3, no. 10, pp. 1405–1410, 2015.

[50] L. H. Gao, Q. Cheng, J. Yang, S. J. Ma, J. Zhao, S. Liu, H. B. Chen, Q. He, W. X. Jiang, H. F. Ma, Q. Y. Wen, L. J. Liang, B. B. Jin, W. W. Liu, L. Zhou, J. Q. Yao, P. H. Wu, and T. J. Cui, "Broadband diffusion of terahertz waves by multi-bit coding metasurfaces," *Light: Science and Applications*, vol. 4, no. January, 2015.

[51] Y. Zhao, X. Cao, J. Gao, Y. Sun, H. Yang, X. Liu, Y. Zhou, T. Han, and W. Chen, "Broadband diffusion metasurface based on a single anisotropic element and optimized by the Simulated Annealing algorithm," *Scientific Reports*, vol. 6, no. January, pp. 1–9, 2016.

[52] L. Jidi, X. Cao, Y. Tang, S. Wang, Y. Zhao, and X. Zhu, "A new coding metasurface for wideband RCS reduction," *Radioengineering*, vol. 27, no. 2, pp. 394–401, 2018.

[53] K. Wang, J. Zhao, Q. Cheng, D. S. Dong, and T. J. Cui, "Broadband and broad-angle low-scattering metasurface based on hybrid optimization algorithm," *Scientific Reports*, vol. 4, pp. 10–15, 2014.

[54] Q. Zhang, C. Liu, X. Wan, L. Zhang, S. Liu, Y. Yang, and T. J. Cui, "Machine-Learning Designs of Anisotropic Digital Coding Metasurfaces," *Advanced Theory and Simulations*, vol. 1800132, p. 1800132, 2018.

[55] T. J. Cui, M. Q. Qi, X. Wan, J. Zhao, Q. Cheng, K. T. Lee, J. Y. Lee, S. Seo, L. J. Guo, Z. Zhang, Z. You, and D. Chu, "Coding metamaterials, digital metamaterials and programmable metamaterials," *Light: Science and Applications*, vol. 3, no. 10, pp. 1–9, 2014.

[56] X. Wan, M. Q. Qi, T. Y. Chen, and T. J. Cui, "Field-programmable beam reconfiguring based on digitally-controlled coding metasurface," *Scientific Reports*, vol. 6, p. 20663, 2016.

[57] Y. B. Li, L. L. Li, B. B. Xu, W. Wu, R. Y. Wu, X. Wan, Q. Cheng, and T. J. Cui, "Transmission-Type 2-Bit Programmable Metasurface for Single-Sensor and Single-Frequency Microwave Imaging," *Scientific Reports*, vol. 6, no. October 2015, pp. 1–8, 2016.

[58] M. Moccia, S. Liu, R. Y. Wu, G. Castaldi, A. Andreone, T. J. Cui, and V. Galdi, "Coding Metasurfaces for Diffuse Scattering: Scaling Laws, Bounds, and Suboptimal Design," *Advanced Optical Materials*, vol. 5, no. 19, pp. 1–11, 2017.

[59] H. Yi, S. W. Qu, B. J. Chen, X. Bai, K. B. Ng, and C. H. Chan, "Flat Terahertz Reflective Focusing Metasurface with Scanning Ability," *Scientific Reports*, vol. 7, no. 1, pp. 2–9, 2017.

[60] L. Zhang, S. Liu, L. Li, and T. J. Cui, "Spin-Controlled Multiple Pencil Beams and Vortex Beams with Different Polarizations Generated by Pancharatnam-Berry Coding Metasurfaces," *ACS Applied Materials and Interfaces*, vol. 9, no. 41, pp. 36 447–36 455, 2017.

[61] Q. Ma, C. B. Shi, G. D. Bai, T. Y. Chen, A. Noor, and T. J. Cui, "Beam-Editing Coding Metasurfaces Based on Polarization Bit and Orbital-Angular-Momentum-Mode Bit," *Advanced Optical Materials*, vol. 5, no. 23, pp. 1–7, 2017.

[62] S. Liu, H. C. Zhang, L. Zhang, Q. L. Yang, Q. Xu, J. Gu, Y. Yang, X. Y. Zhou, J. Han, Q. Cheng, W. Zhang, and T. J. Cui, "Full-State Controls of Terahertz Waves Using Tensor Coding Metasurfaces," *ACS Applied Materials and Interfaces*, vol. 9, no. 25, pp. 21 503–21 514, 2017.

[63] X. G. Zhang, W. X. Jiang, and T. J. Cui, "Frequency-dependent transmission-type digital coding metasurface controlled by light intensity," *Applied Physics Letters*, vol. 113, no. 9, pp. 1–6, 2018.

[64] Y. Zhou, G. Zhang, H. Chen, P. Zhou, X. Wang, L. Zhang, and L. Zhang, "Design of Phase Gradient Coding Metasurfaces for Broadband Wave Modulating," *Scientific Reports*, vol. 8, p. 8672, 2018.

[65] L. Zhang, X. Q. Chen, S. Liu, Q. Zhang, J. Zhao, J. Y. Dai, G. D. Bai, X. Wan, Q. Cheng, G. Castaldi, V. Galdi, and T. J. Cui, "Space-time-coding digital metasurfaces," *Nature Communications*, vol. 9, no. 1, p. 4334, 2018.

[66] G. Ding, K. Chen, X. Luo, J. Zhao, T. Jiang, and Y. Feng, "Dual-helicity decoupled coding metasurface for independent spin-to-orbital angular momentum conversion," *Phys. Rev. Applied*, vol. 11, p. 044043, Apr 2019.

[67] Q. Zheng, Y. Li, Y. Pang, J. Wang, H. Chen, S. Qu, M. Feng, and J. Zhang, "Wideband coding metasurfaces based on low q resonators," *Optics Communications*, vol. 430, pp. 189–194, 2019.

[68] S. Iqbal, H. A. Madni, S. Liu, L. Zhang, and T. J. Cui, "Full controls of OAM vortex beam and realization of retro and negative reflections at oblique incidence using dual-band 2-bit coding metasurface," *Materials Research Express*, vol. 6, no. 12, p. 125804, dec 2019.

[69] M. Wang, H. F. Ma, L. W. Wu, S. Sun, W. X. Tang, and T. J. Cui, "Hybrid digital coding metasurface for independent control of propagating surface and spatial waves," *Advanced Optical Materials*, vol. 7, no. 13, p. 1900478, 2019.

[70] R. Phon and S. Lim, "Dynamically self-reconfigurable multifunctional all-passive metasurface," *ACS Applied Materials & Interfaces*, vol. 12, no. 37, pp. 42 393–42 402, 2020.

[71] Y.-L. Sun, X.-G. Zhang, Q. Yu, W.-X. Jiang, and T.-J. Cui, "Infrared-controlled programmable metasurface," *Science Bulletin*, vol. 65, no. 11, pp. 883–888, 2020.

[72] H. Chen, W.-B. Lu, Z.-G. Liu, and M.-Y. Geng, "Microwave programmable graphene metasurface," *ACS Photonics*, vol. 7, no. 6, pp. 1425–1435, 2020.

[73] J. Shabanpour, "Programmable anisotropic digital metasurface for independent manipulation of dual-polarized thz waves based on a voltage-controlled phase transition of vo2 microwires," *J. Mater. Chem. C*, vol. 8, pp. 7189–7199, 2020.

[74] T. Qian, "Reconfigurable metasurface antenna based on the liquid metal for flexible scattering fields manipulation," *Micromachines*, vol. 12, no. 3, 2021.

[75] W. Li, T. Qiu, J. Wang, L. Zheng, Y. Jing, Y. Jia, H. Wang, Y. Han, and S. Qu, "Programmable coding metasurface reflector for reconfigurable multibeam antenna application," *IEEE Transactions on Antennas and Propagation*, vol. 69, no. 1, pp. 296–301, 2021.

[76] R. Mehrotra, R. Ansari, A. Pitilakis, S. Nie, C. Liaskos, N. Kantartzis, and A. Pitsillides, "3D channel modeling and characterization for hypersurface empowered indoor

environment at 60 GHz millimeter-wave band," in *Proceedings of the SPECTS '19*, 2019.

[77] A. C. Tasolamprou, A. Pitilakis, S. Abadal, O. Tsilipakos, X. Timoneda, H. Taghvaee, M. Sajjad Mirmoosa, F. Liu, C. Liaskos, A. Tsioliaridou, S. Ioannidis, N. V. Kantartzis, D. Manessis, J. Georgiou, A. Cabellos-Aparicio, E. Alarcón, A. Pitsillides, I. F. Akyildiz, S. A. Tretyakov, E. N. Economou, M. Kafesaki, and C. M. Soukoulis, "Exploration of intercell wireless millimeter-wave communication in the landscape of intelligent metasurfaces," *IEEE Access*, vol. 7, pp. 122 931–122 948, 2019.

[78] C. Liaskos, G. Pyrialakos, A. Pitilakis, S. Abadal, A. Tsioliaridou, A. Tasolamprou, O. Tsilipakos, N. Kantartzis, S. Ioannidis, E. Alarcon, A. Cabellos, M. Kafesaki, A. Pitsillides, K. Kossifos, J. Georgiou, and I. Akyildiz, "Absense: Sensing electromagnetic waves on metasurfaces via ambient compilation of full absorption," in *Proceedings of the NANOCOM '19*, 2019.

[79] C. Liaskos, A. Tsioliaridou, S. Nie, A. Pitsillides, S. Ioannidis, and I. F. Akyildiz, "On the network-layer modeling and configuration of programmable wireless environments," *IEEE/ACM Transactions on Networking*, vol. 27, no. 4, pp. 1696–1713, 2019.

[80] T. Saeed, C. Skitsas, D. Kouzapas, M. Lestas, V. Soteriou, A. Philippou, S. Abadal, C. Liaskos, L. Petrou, J. Georgiou, and A. Pitsillides, "Fault Adaptive Routing in Metasurface Network Controllers," in *Proceedings of the NoCArc '18*, 2018.

[81] D. Kouzapas, C. Skitsas, T. Saeed, V. Soteriou, M. Lestas, A. Philippou, S. Abadal, C. Liaskos, L. Petrou, J. Georgiou *et al.*, "Towards fault adaptive routing in metasurface controller networks," *Journal of Systems Architecture*, vol. 106, p. 101703, 2020.

[82] A. C. Tasolamprou, A. Pitilakis, S. Abadal, O. Tsilipakos, X. Timoneda, H. Taghvaee, M. S. Mirmoosa, F. Liu, C. Liaskos, A. Tsioliaridou *et al.*, "Exploration of intercell wireless millimeter-wave communication in the landscape of intelligent metasurfaces," *IEEE access*, vol. 7, pp. 122 931–122 948, 2019.

[83] L. Zhang, X. Q. Chen, S. Liu, Q. Zhang, J. Zhao, J. Y. Dai, G. D. Bai, X. Wan, Q. Cheng, G. Castaldi, V. Galdi, and T. J. Cui, "Space-time-coding digital metasurfaces," *Nature Communications*, vol. 9, no. 1, pp. 1–11, 2018.

[84] "CST Microwave Studio http://www.cst.com." [Online]. Available: http://www.cst.com

[85] T.-J. Cui, S. Liu, and L.-L. Li, "Information entropy of coding metasurface," *Light: Science & Applications*, vol. 5, no. 11, p. e16172, 2016.

[86] R. Y. Wu, C. B. Shi, S. Liu, W. Wu, and T. J. Cui, "Addition Theorem for Digital Coding Metamaterials," *Advanced Optical Materials*, vol. 6, no. 5, pp. 1–10, 2018.

[87] Z. Wei, Y. Cao, X. Su, Z. Gong, Y. Long, and H. Li, "Highly efficient beam steering with a transparent metasurface," *Opt. Express*, vol. 21, no. 9, pp. 10 739–10 745, May 2013.

[88] A. Forouzmand and H. Mosallaei, "Tunable two dimensional optical beam steering with reconfigurable indium tin oxide plasmonic reflectarray metasurface," *Journal of Optics (United Kingdom)*, vol. 18, no. 12, pp. 0–8, 2016.

[89] A. H. Naqvi and S. Lim, "A beam-steering antenna with a fluidically programmable metasurface," *IEEE Transactions on Antennas and Propagation*, pp. 1–1, 2019.

[90] T. Saeed, S. Abadal, C. Liaskos, A. Pitsillides, H. Taghvaee, A. Cabellos-Aparicio, M. Lestas, and E. Alarcón, "Workload Characterization of Programmable Metasurfaces," in *Proceeding of the NANOCOM '19*, 2019.

[91] I. F. Akyildiz, C. Han, and S. Nie, "Combating the Distance Problem in the Millimeter Wave and Terahertz Frequency Bands," *IEEE Communications Magazine*, vol. 56, no. June, pp. 102–108, 2018.

[92] M.-A. Badiu and J. P. Coon, "Communication through a large reflecting surface with phase errors," 2019.

[93] L. Rondinelli, "Effects of random errors on the performance of antenna arrays of many elements," in *1958 IRE International Convention Record*, vol. 7. IEEE, 1966, pp. 174–189.

[94] C. Zahm, "Effects of errors in the direction of incidence on the performance of an adaptive array," *Proceedings of the IEEE*, vol. 60, no. 8, pp. 1008–1009, 1972.

[95] H. Wang, "Performance of phased-array antennas with mechanical errors," *IEEE Transactions on Aerospace and Electronic Systems*, vol. 28, no. 2, pp. 535–545, 1992.

[96] L. Poli, P. Rocca, N. Anselmi, and A. Massa, "Dealing with uncertainties on phase weighting of linear antenna arrays by means of interval-based tolerance analysis," *IEEE Transactions on Antennas and Propagation*, vol. 63, no. 7, pp. 3229–3234, 2015.

[97] F. Liu, O. Tsilipakos, A. Pitilakis, A. C. Tasolamprou, M. S. Mirmoosa, N. V. Kantartzis, D.-H. Kwon, J. Georgiou, K. Kossifos, M. A. Antoniades, M. Kafesaki, C. M. Soukoulis, and S. A. Tretyakov, "Intelligent metasurfaces with continuously tunable local surface impedance for multiple reconfigurable functions," *Phys. Rev. Applied*, vol. 11, p. 044024, Apr 2019.

[98] International Telecommunication Union (ITU), "Report of the cpm to wrc-19," in *World Radiocommunication Conference*, no. March, 2019. [Online]. Available: https://www.itu.int/md/R15-CPM19.02-R-0001/en

[99] J. Srinivasan, S. V. Adve, P. Bose, and J. A. Rivers, "The impact of technology scaling on lifetime reliability," in *International Conference on Dependable Systems and Networks, 2004*, 2004, pp. 177–186.

[100] A. Pitilakis, O. Tsilipakos, F. Liu, K. M. Kossifos, A. C. Tasolamprou, D. Kwon, M. S. Mirmoosa, D. Manessis, N. V. Kantartzis, C. Liaskos, M. A. Antoniades, J. Georgiou, C. M. Soukoulis, M. Kafesaki, and S. A. Tretyakov, "A multi-functional reconfigurable metasurface: Electromagnetic design accounting for fabrication aspects," *IEEE Transactions on Antennas and Propagation*, pp. 1–1, 2020.

[101] M. Marcus and B. Pattan, "Millimeter wave propagation: spectrum management implications," *IEEE Microwave Magazine*, vol. 6, no. 2, pp. 54–62, June 2005.

[102] M. Hunukumbure, J. Luo, M. Castaneda, R. DErrico, P. Zetterberg, A. A. Zaidi, J. Vihriala, and D. Giustiniano, "Mm-wave specific challenges in designing 5G transceiver architectures and air-interfaces," 2018.

[103] E. Froehlich and A. Kent, *The Froehlich/Kent encyclopedia of telecommunications: Volume 2*, 1st ed. CRC Press, 1991.

[104] H. B. Sedeh, M. M. Salary, and H. Mosallaei, "Adaptive multichannel terahertz communication by space-time shared aperture metasurfaces," *IEEE Access*, pp. 1–1, 2020.

[105] K. I. Pedersen, F. Frederiksen, G. Berardinelli, and P. E. Mogensen, "The Coverage-Latency-Capacity Dilemma for TDD Wide Area Operation and Related 5G Solutions," in *2016 IEEE 83rd Vehicular Technology Conference (VTC Spring)*, 2016, pp. 1–5.

[106] S.-Y. Lien, S.-L. Shieh, Y. Huang, B. Su, Y.-L. Hsu, and H.-Y. Wei, "5G New Radio: Waveform, Frame Structure, Multiple Access, and Initial Access," *IEEE Communications Magazine*, vol. 55, no. 6, pp. 64–71, 2017.

[107] H. Taghvaee, S. Abadal, A. Pitilakis, O. Tsilipakos, A. C. Tasolamprou, C. Liaskos, M. Kafesaki, N. V. Kantartzis, A. Cabellos-Aparicio, and E. Alarcón, "Scalability analysis of programmable metasurfaces for beam steering," *IEEE Access*, vol. 8, pp. 105 320–105 334, 2020.

[108] C. Huang, A. Zappone, M. Debbah, and C. Yuen, "Achievable rate maximization by passive intelligent mirrors," in *2018 IEEE International Conference on Acoustics, Speech and Signal Processing (ICASSP)*, no. 1, 2018, pp. 3714–3718.

[109] X. Hu, C. Zhong, Y. Zhu, X. Chen, and Z. Zhang, "Programmable metasurface-based multicast systems: Design and analysis," *IEEE Journal on Selected Areas in Communications*, vol. 38, no. 8, pp. 1763–1776, 2020.

[110] 3GPP, "TR 138 901 - V15.0.0 - 5G; Study on channel model for frequencies from 0.5 to 100 GHz (3GPP TR 38.901 version 15.0.0 Release 15)," 2018.

[111] E. Basar, M. Di Renzo, J. De Rosny, M. Debbah, M. Alouini, and R. Zhang, "Wireless communications through reconfigurable intelligent surfaces," *IEEE Access*, vol. 7, pp. 116 753–116 773, 2019.

[112] E. Basar, I. Yildirim, and I. Akyildiz, "Indoor and outdoor physical channel modeling and efficient positioning for reconfigurable intelligent surfaces in mmwave bands," *ArXiv*, vol. abs/2006.02240, 2020.

[113] O. Ozdogan, E. Bjornson, and E. G. Larsson, "Intelligent Reflecting Surfaces: Physics, Propagation, and Pathloss Modeling," *IEEE Wirel. Commun. Lett.*, vol. 9, no. 5, pp. 581–585, 2020.

[114] E. Bjornson, O. Ozdogan, and E. G. Larsson, "Intelligent Reflecting Surface Versus Decode-and-Forward: How Large Surfaces are Needed to Beat Relaying?" *IEEE Wirel. Commun. Lett.*, vol. 9, no. 2, pp. 244–248, 2020.

[115] A. Jain, E. Lopez-Aguilera, and I. Demirkol, "User Association and Resource Allocation in 5G (AURA-5G): A Joint Optimization Framework," 2020.

[116] A. Jain, E. Lopez-Aguilera, and I. Demirkol, "Are mobility management solutions ready for 5G and beyond?" *Computer Communications*, vol. 161, pp. 50–75, Sept. 2020.

[117] S. Sun, T. S. Rappaport, T. A. Thomas, A. Ghosh, H. C. Nguyen, I. Z. Kovács, I. Rodriguez, O. Koymen, and A. Partyka, "Investigation of prediction accuracy, sensitivity, and parameter stability of large-scale propagation path loss models for 5g wireless communications," *IEEE Transactions on Vehicular Technology*, vol. 65, no. 5, pp. 2843–2860, 2016.

[118] M. Polese, M. Giordani, M. Mezzavilla, S. Rangan, and M. Zorzi, "Improved handover through dual connectivity in 5g mmwave mobile networks," *IEEE Journal on Selected Areas in Communications*, vol. 35, no. 9, pp. 2069–2084, 2017.

[119] Michał Maternia and S. E. E. Ayoubi, "5G PPP use cases and performance evaluation models," *5G-PPP Initiat.*, 2016.

[120] T. Specification, "System Architecture for the 5G System (3GPP TS 23.501 version 15.2.0 Release 15)," 2018.

[121] S. Sun, T. S. Rappaport, M. Shafi, P. Tang, J. Zhang, and P. J. Smith, "Propagation models and performance evaluation for 5g millimeter-wave bands," *IEEE Transactions on Vehicular Technology*, vol. 67, no. 9, pp. 8422–8439, 2018.

[122] S. E. Hosseininejad, K. Rouhi, M. Neshat, R. Faraji-Dana, A. Cabellos-Aparicio, S. Abadal, and E. Alarcón, "Reprogrammable Graphene-based Metasurface Mirror with Adaptive Focal Point for THz Imaging," *Scientific Reports*, vol. 9, p. 2868, 2019.

[123] I. E. Lagaris, A. Likas, and D. I. Fotiadis, "Artificial neural networks for solving ordinary and partial differential equations," *IEEE transactions on neural networks*, vol. 9, no. 5, pp. 987–1000, 1998.

[124] M. Khorasaninejad, Z. Shi, A. Y. Zhu, W. T. Chen, V. Sanjeev, A. Zaidi, and F. Capasso, "Achromatic metalens over 60 nm bandwidth in the visible and metalens with reverse chromatic dispersion," *Nano Letters*, vol. 17, no. 3, pp. 1819–1824, 2017.

[125] K. Valasoulis, D. Fotiadis, I. Lagaris, and A. Likas, "Solving differential equations with neural networks: implementation on a DSP platform," in *2002 14th International Conference on Digital Signal Processing Proceedings. DSP 2002 (Cat. No.02TH8628)*, vol. 2, 2002, pp. 1265–1268 vol.2.

[126] I. G. Tsoulos, D. Gavrilis, and E. Glavas, "Solving differential equations with constructed neural networks," *Neurocomputing*, vol. 72, no. 10-12, pp. 2385–2391, 2009.

[127] S. Inampudi and H. Mosallaei, "Neural network based design of metagratings," *Applied Physics Letters*, vol. 112, no. 24, 2018.

[128] T. Qiu *et al.*, "Deep Learning: A Rapid and Efficient Route to Automatic Metasurface Design," *Advanced Science*, vol. 6, no. 12, 2019.

[129] P. del Hougne, M. Fink, and G. Lerosey, "Optimally diverse communication channels in disordered environments with tuned randomness," *Nature Electronics*, vol. 2, no. 1, pp. 36–41, 2019.

[130] P. del Hougne, M. F. Imani, M. Fink, D. R. Smith, and G. Lerosey, "Precise localization of multiple noncooperative objects in a disordered cavity by wave front shaping," *Phys. Rev. Lett.*, vol. 121, p. 063901, Aug 2018.

[131] A. Santos, E. Figueiredo, M. Silva, C. Sales, and J. Costa, "Machine learning algorithms for damage detection: Kernel-based approaches," *Journal of Sound and Vibration*, vol. 363, pp. 584–599, 2016.

[132] M. W. Libbrecht and W. S. Noble, "Machine learning applications in genetics and genomics," *Nature Reviews Genetics*, vol. 16, no. 6, pp. 321–332, Jun. 2015.

[133] S. Mullainathan and J. Spiess, "Machine learning: An applied econometric approach," *Journal of Economic Perspectives*, vol. 31, no. 2, pp. 87–106, 2017.

[134] H.-Y. Li, H.-T. Zhao, M.-L. Wei, H.-X. Ruan, Y. Shuang, T. J. Cui, P. del Hougne, and L. Li, "Intelligent electromagnetic sensing with learnable data acquisition and processing," *Patterns*, vol. 1, no. 1, p. 100006, 2020.

[135] S. Liu, T. J. Cui, A. Noor, Z. Tao, H. C. Zhang, G. D. Bai, Y. Yang, and X. Y. Zhou, "Negative reflection and negative surface wave conversion from obliquely incident electromagnetic waves," *Light: Science and Applications*, vol. 7, no. 5, pp. 18 008–18 011, 2018.

[136] J. Jiang, D. Sell, S. Hoyer, J. Hickey, J. Yang, and J. A. Fan, "Free-form diffractive metagrating design based on generative adversarial networks," *ACS Nano*, vol. 13, no. 8, pp. 8872–8878, 2019.

[137] J. A. Hodge, K. V. Mishra, and A. I. Zaghloul, "Joint Multi-layer GAN-based Design of Tensorial RF Metasurfaces," in *2019 IEEE 29th International Workshop on Machine Learning for Signal Processing (MLSP)*, 2019, pp. 1–6.

[138] S. An, B. Zheng, H. Tang, M. Y. Shalaginov, L. Zhou, H. Li, M. Kang, K. A. Richardson, T. Gu, J. Hu, C. Fowler, and H. Zhang, "Multifunctional metasurface design with a generative adversarial network," *Advanced Optical Materials*, vol. 9, no. 5, p. 2001433, 2021.

[139] Q. Zhang, C. Liu, X. Wan, L. Zhang, S. Liu, Y. Yang, and T. J. Cui, "Machine-Learning Designs of Anisotropic Digital Coding Metasurfaces," *Advanced Theory and Simulations*, vol. 2, no. 2, p. 1800132, Feb. 2019.

[140] S. An, C. Fowler, B. Zheng, M. Y. Shalaginov, H. Tang, H. Li, L. Zhou, J. Ding, A. M. Agarwal, C. Rivero-Baleine, K. A. Richardson, T. Gu, J. Hu, and H. Zhang, "A novel modeling approach for all-dielectric metasurfaces using deep neural networks," *arXiv preprint arXiv:1906.03387*, 2019.

[141] A. Lalbakhsh, M. U. Afzal, and K. P. Esselle, "Multiobjective particle swarm optimization to design a time-delay equalizer metasurface for an electromagnetic band-gap resonator antenna," *IEEE Antennas and Wireless Propagation Letters*, vol. 16, pp. 912–915, 2017.

[142] P. R. Wiecha and O. L. Muskens, "Deep Learning Meets Nanophotonics: A Generalized Accurate Predictor for Near Fields and Far Fields of Arbitrary 3D Nanostructures," *Nano Letters*, vol. 20, no. 1, pp. 329–338, 2020.

[143] H. Taghvaee, S. Abadal, J. Georgiou, A. Cabellos-Aparicio, and E. Alarcón, "Fault tolerance in programmable metasurfaces: The beam steering case," in *2019 IEEE International Symposium on Circuits and Systems (ISCAS)*, 2019, pp. 1–5.

[144] N. Ashraf, M. Lestas, T. Saeed, H. Taghvaee, S. Abadal, A. Pitsillides, and C. Liaskos, "Extremum seeking control for beam steering using hypersurfaces," in *2020 IEEE International Conference on Communications Workshops (ICC Workshops)*, 2020, pp. 1–6.

[145] M. Yazdi and M. Albooyeh, "Analysis of metasurfaces at oblique incidence," *IEEE Transactions on Antennas and Propagation*, vol. 65, no. 5, pp. 2397–2404, 2017.

[146] H. Chu, J. Qi, S. Xiao, and J. Qiu, "A thin wideband high-spatial-resolution focusing metasurface for near-field passive millimeter-wave imaging," *Applied Physics Letters*, vol. 112, no. 17, p. 174101, 2018.

[147] S. M. Q. A. HShah, N. Shoaib, F. Ahmed, A. Alomainy, A. Quddious, S. Nikolaou, M. A. Imran, and Q. H. Abbasi, "A multiband circular polarization selective metasurface for microwave applications," *Scientific reports*, vol. 11, no. 1774, 2021.

[148] M. Bakır, M. Karaaslan, F. Dincer, and C. Sabah, "Metamaterial characterization by applying different boundary conditions on triangular split ring resonator type metamaterials," *International Journal of Numerical Modelling: Electronic Networks, Devices and Fields*, vol. 30, no. 5, p. e2188, 2017, e2188 JNM-16-0019.R1.

[149] M. Lei, N. Feng, Q. Wang, Y. Hao, S. Huang, and K. Bi, "Magnetically tunable metamaterial perfect absorber," *Journal of Applied Physics*, vol. 119, no. 24, p. 244504, 2016.

[150] H. K. Kim, D. Lee, and S. Lim, "Frequency-tunable metamaterial absorber using a varactor-loaded fishnet-like resonator," *Appl. Opt.*, vol. 55, no. 15, pp. 4113–4118, May 2016.

[151] B. Zhu, Y. Feng, J. Zhao, C. Huang, and T. Jiang, "Switchable metamaterial reflector/absorber for different polarized electromagnetic waves," *Applied Physics Letters*, vol. 97, no. 5, p. 051906, 2010.

[152] Z. Tao, X. Wan, B. C. Pan, and T. J. Cui, "Reconfigurable conversions of reflection, transmission, and polarization states using active metasurface," *Applied Physics Letters*, vol. 110, no. 12, p. 121901, 2017.

[153] H. Wymeersch, J. He, B. Denis, A. Clemente, and M. Juntti, "Radio localization and mapping with reconfigurable intelligent surfaces: Challenges, opportunities, and research directions," *IEEE Vehicular Technology Magazine*, vol. 15, no. 4, pp. 52–61, 2020.

[154] P. del Hougne, "Robust position sensing with wave fingerprints in dynamic complex propagation environments," *Phys. Rev. Research*, vol. 2, p. 043224, Nov 2020.

[155] P. del Hougne, M. F. Imani, A. V. Diebold, R. Horstmeyer, and D. R. Smith, "Learned Integrated Sensing Pipeline: Reconfigurable Metasurface Transceivers as Trainable Physical Layer in an Artificial Neural Network," *Advanced Science*, vol. 7, no. 3, p. 1901913, 2020.

[156] M. Najafi and R. Schober, "Intelligent reflecting surfaces for free space optical communications," in *2019 IEEE Global Communications Conference (GLOBECOM)*, 2019, pp. 1–7.

[157] S. Kisseleff, W. A. Martins, H. Al-Hraishawi, S. Chatzinotas, and B. Ottersten, "Reconfigurable intelligent surfaces for smart cities: Research challenges and opportunities," *IEEE Open Journal of the Communications Society*, vol. 1, pp. 1781–1797, 2020.

[158] M. Di Renzo, K. Ntontin, J. Song, F. H. Danufane, X. Qian, F. Lazarakis, J. De Rosny, D. T. Phan-Huy, O. Simeone, R. Zhang, M. Debbah, G. Lerosey, M. Fink, S. Tretyakov, and S. Shamai, "Reconfigurable intelligent surfaces vs. relaying: Differences, similarities, and performance comparison," *IEEE Open Journal of the Communications Society*, vol. 1, pp. 798–807, 2020.

[159] M. Di Renzo, A. Zappone, M. Debbah, M. S. Alouini, C. Yuen, J. de Rosny, and S. Tretyakov, "Smart radio environments empowered by reconfigurable intelligent surfaces: How it works, state of research, and the road ahead," *IEEE Journal on Selected Areas in Communications*, vol. 38, no. 11, pp. 2450–2525, 2020.

[160] B. M. Masini, C. M. Silva, and A. Balador, "The use of meta-surfaces in vehicular networks," *Journal of Sensor and Actuator Networks*, vol. 9, no. 1, 2020.

[161] L. Yang, F. Meng, J. Zhang, M. O. Hasna, and M. D. Renzo, "On the performance of ris-assisted dual-hop uav communication systems," *IEEE Transactions on Vehicular Technology*, vol. 69, no. 9, pp. 10 385–10 390, 2020.

[162] E. Basar, M. Di Renzo, J. De Rosny, M. Debbah, M. Alouini, and R. Zhang, "Wireless communications through reconfigurable intelligent surfaces," *IEEE Access*, vol. 7, pp. 116 753–116 773, 2019.

[163] J. Liu, *Radial Basis Function (RBF) neural network control for mechanical systems: design, analysis and Matlab simulation*. Springer Science & Business Media, 2013.

[164] K. Kasiviswanathan and A. Agarwal, "Radial basis function artificial neural network: spread selection," *International Journal of Advanced Computer Science*, vol. 2, no. 11, pp. 394–398, 2012.

[165] M. F. Møller, "A scaled conjugate gradient algorithm for fast supervised learning," *Elsevier Neural networks*, vol. 6, no. 4, pp. 525–533, 1993.

[166] T. Cui, S. Liu, and L. Li, "Information entropy of coding metasurface," *Light Sci Appl*, vol. 5, no. e16172, 2016.

[167] K. M. Kossifos, L. Petrou, G. Varnava *et al.*, "Toward the realization of a programmable metasurface absorber enabled by custom integrated circuit technology," *IEEE Access*, vol. 8, pp. 92 986–92 998, 2020.

[168] T. Saeed, V. Soteriou, C. Liaskos *et al.*, "Toward fault-tolerant deadlock-free routing in hypersurface-embedded controller networks," *IEEE Networking Letters*, vol. 2, no. 3, pp. 140–144, 2020.